IN MEMORIAM OF COLLEAGUE AND FRIEND SOFIA DONU

25.01.1948 – 14.09.2022

Sofia Donu, our colleague and friend, began her scientific career in the summer of 1971, in the Institute of Applied Physics as a laboratory assistant at the Laboratory of Physical Methods of Solid State Investigation, which today bears the name of its founder, academician Tadeusz Malinowski, and she belongs to the second generation of Moldavan crystallographers. Her supervisor was the young Doctor of physical and mathematical sciences, crystallographer Ion Diacon who applied the electron diffraction method to study the structure of crystals and textured polycrystals. Naturally, this direction became the topic of Sofia Donu's scientific research. It should be noted that this method differs significantly by techniques and equipment from the methods of single crystal X-ray diffraction analysis and X-ray diffraction analysis of polycrystals used by most Laboratory staff. Nevertheless, specificity of crystallization of some compounds based on amino-acids did not allow obtaining monocrystals appropriate for X-ray method and only electron diffraction method was suitable for study the structures of such compounds. Sofia started to overcome selflessly and persistently all the difficulties and obstacles that stood in the way of her research work. She had to learn how to prepare samples and maintain and

troubleshoot the foreline and oil diffusion pumps to ensure the correct operation of the electronograph, to understand the resulting diffraction patterns, and apply them to deciphering the crystal structures. Perseverance and hard work have brought first successful results and Sofia became an engineer in 1978, and scientific researcher of the Laboratory in 1983. In 1985 Sofia Donu has defended her Ph.D. thesis entitled “Crystal and electronic structures of some mixed compounds of copper(II) with alpha-amino-acids” by specialty crystallography and crystal physics. Her scientific research was devoted to the study of the structure of copper(II) complexes with natural alpha-amino acids, such as glycine, serine, threonine, alpha-aminobutyric acid and homoserine, which have shown antitumor activity and were classified as potential drugs. For these reasons the thesis and some of her publications, for examples in “Chemistry tumor therapy in the USSR” were marked as "Restricted Use Only" and unavailable for wide audience. The quantum-mechanical studies of the electronic structure of these compounds were aimed at understanding the mechanism of their action and interaction with receptors. It is worth noting that Sofia's successful research was carried out in line with a wide range of experimental and theoretical studies carried out in the Laboratory of Physical Methods of Solid State investigation of the Institute of Applied Physics for the search of new anticancer drugs and understanding the mechanism of their action within the framework of the State program. The scientific activity of Sofia Donu in our Laboratory lasted till 1997, when she joined the organizational and administrative Department of the Academy of Sciences of Moldova.

Sofia Donu (second from left in the first line) among the colleagues from the Laboratory of Physical Methods of Solid State Investigation at the entrance to the Institute of Applied Physics.

However, after she has left our Lab., Sofia's friendship and warm relations with the collaborators of the Laboratory have never been interrupted. She always participated in all informal activities and events of the Laboratory: celebration of the New Year, March 8, Easter, members of laboratory birthdays in the same way as it was before. Sofia sang well, she participated in the academic choir, and often performed wonderful Moldovan songs for us in the lab., and we listened to her with pleasure and tried to sing along. Many of us remember well her unforgettable birthdays, on January 25, which we usually celebrated at her apartment upon her kind invitations. Having been a skilled hostess and cook, she has set a table with delicious dishes and homemade drinks. The very special dish that we always looked forward for was the traditional famous and incomparable, delicious cheese-stuffed Moldavan layer pie "Placinta" which she cooked skillfully. She always joked that the pie was so delicious because she pressed the dough to her chest. We were returning home very happy and in a good mood, and then we waited again for Sofia's next birthday.

Having been in a close proximity for a long time, we knew and shared many personal things seeking advice, sympathy and support. Sofia also shared with us all her joyful events and sorrows, and we always tried to support her in the most difficult situations she met in her life. She knew how to remain a cheerful, optimistic and sympathetic person who loved life, she knew how to laugh contagiously and have fun from the bottom of her heart. This is how we will remember her in our hearts.

Colleagues and friends, all those who had the pleasure to be in contact and cooperate with Sofia Donu will certainly remember her gratefully and pass to the next generation the fond memories about her as a wonderful person and scientist.

Odihnească-se în pace.

Victor Ch. Kravtsov

Laboratory of Physical Methods of Solid State Investigation “Tadeusz Malinowski”,
Institute of Applied Physics.

IN MEMORIAM, SOFIA DONU: BY HER DAUGHTER

With a difference of 15 years from my sister Diana, I was born into the Donu family when both parents already had their PhDs defended and were in the prime of their careers as physicists.

My mother Sofia, besides being a soloist in the choir of the Academy of Sciences and a talented scientist, was first and foremost a caring mother and an adventurer in life.

Her personality can be described by the following story, which always brings a smile to my face whenever I remember it.

In her ninth month of pregnancy with me, she got a craving for cherries and without much hesitation climbed the cherry tree in my grandparents' garden. My father seeing this image got visibly emotional and asked her to come down, to which my mother reacted quietly and continued the feast.

What a wonderful lesson about living in the present moment, here and now when you feel for it.

I had a happy childhood where I had the opportunity to develop my talents and discover the world at my own pace. Out of the little she had, she moved me to school #56 (Spiru Haret High School today) to have access to programs and teachers qualified in education. I was lucky that she listened to my wishes and enrolled me at the music school No. 5 (now "Eugen Doga" Music School) in the piano section. This is how my artistic activity started.

In addition to the music school, I attended the folk dance circle, an activity close to my heart, which continued until I left for the Czech Republic to continue my master degree studies. I remember our first trip abroad with the dance group "Miorița", led by master Valentina Cocea. It was an international festival in Georgia, and the travel expenses for a family of scholars were beyond our means. However, my mother went to the trade union committee of the Academy of Sciences and managed to get the money so that I could attend the event. From the little we had as a family, she always knew how to look for solutions to make us happy. An indescribable strength of character in such a gentle and tender person. I am forever grateful to her for trying to keep going despite difficulties and barriers.

In her everyday life, she was an accomplished housewife who loved receiving guests and was always the life of the party. She charmed everyone with the pies and dishes she lovingly made. Most of the ingredients were homemade, as she believed with all her being that the tastiest can only be cooked at home and with homemade products.

Even after tasting fine and exquisitely cooked dishes from the kitchens of different countries, I always longed for the tasty treats my mother used to serve us at home.

I remember that every year, everyone in the physics lab where my mother worked looked forward to January 25, my mother's birthday. My mother always invited her colleagues to our house, and they still mention that everyone loved the winter holidays, but they were most looking forward to Sofiica's birthday, because the food she prepared was simply extraordinary! Made with a lot of love. My mother was a normal human being but she exuded love, whatever she did.

Looking back, I can say with certainty that my mother was an exceptional woman and not just because she was my mother. It is fascinating how such a tiny person can encompass so many

qualities and talents - a successful scientist, a beautiful woman at heart and body, a gifted singer and not least an extraordinary housewife.

No doubt, I inherited the best traits from both sides, but my mother stood out from everyone else due to the "ease" with which she walked through life. She saw the beautiful even when it looked ugly, she smiled even when she was sad.

My gratitude has no boundaries, and the accomplishments I add to the record year after year make her live on through me. I've made up my mind. Both my mother and my older sister, Diana, will live on through me and will continue to fulfil their dreams through me. This thought determines me to remain eager and not to beat myself left or right from my personal path full of dreams and ambitions.

The period when I lost Diana to an incurable illness was a difficult one, as that same year I won a scholarship to study in the Czech Republic and was unsure if it would make sense to leave my parents alone.

But my mother insisted that I go because it was a good opportunity for my future. I greatly appreciated her letting me go, just when she probably needed her closest ones by her side the most. Needless to say, this traumatic episode in our lives had a very negative impact on my mother's well-being. Still, she tried to move forward, even though it was probably the most complicated thing she had ever done.

I have lost two women in my family and yet I want to believe that they are beside me and guiding me from somewhere above. I have a responsibility that I carry out with fondness and that is to keep their memory alive going forward.

Whenever I have the opportunity, I commemorate their life before they left, and through the mountains I conquer - their life after they left. They live on through me, and that is the most beautiful thing that helps me move forward with confidence. I will always be grateful to these two women for the lessons they taught me, which enriched my life and calibrated my future.

I carry our name with honor and promise to be a promoter of our family values going forward.

With much gratitude,

Vica

RESTITUTIONS IN MEMORIAM SOFIA DONU

Life not infrequently brings people to our doorstep with whom it might initially seem you have little in common, but not in the episode with Sofia Donu. And not just because we were from the same land and sap from which we grew. This was not the case when we met with Sofia Donu. The event happened through Eleonora Ciumacov, also a doctoral student (aspiring) noble soul who was always open to communication and due to happy encounters we met Valeriu Canter, Ilie Fiștic and other individuals far away from home in Moscow at the Academy of Sciences of the USSR, in the dormitories where we lived. I invoke only these names from our group back then because to my regret all four have gone to the world without longing, and their absence with nothing can be filled, only the memories that remained with us in this dimension. Memories that take you back to the heated discussions of previous times spanning from research to cultural topics, exchange of information and much longing for the places and loved ones waiting for us to return home. It was a time when each of us was trying to develop more than we were allowed, because the possibilities in the metropolis were far beyond those in Chisinau, including access to Romanian books.

Doctor Sofia Donu surprised me with her firmness and delicacy. However, from all of us, she was the most caught between the results of her research and her mother's desire to return home as soon as possible where her daughter Diana was waiting for her. Later on we had already met again in Chișinău with defended PhDs. In the meantime Sofia had defended another PhD – she had given birth to her second child - daughter Victoria. A gift that helped her cope with the vicissitudes and losses that befell her home - the loss of her eldest daughter Diana at 37. Although short in stature, she proved to be a strong family woman and a strong advocate for research and national culture. She participated in the organization and conduct of thematic events as scientific secretary of the "Moldavian Journal of the Physical Sciences", including presenting papers on the results obtained in the projects. Also, her remarkable role as a singer in the Academy Choral Chapel established in the early 1980s in the Academy of Science remains outstanding. Throughout her career she tried to be close to the people with whom she worked, with those who at one time or another asked for her help without expecting reciprocity.

But perhaps most of all she was most herself during the WINTER HOLIDAYS, even if the other celebrations were not overlooked. I have highlighted the winter holidays because in them, above all, the chosen carols of high moral standards were interwoven with the culture of dishes prepared according to the customs. And not without those remarkable exceptions related to the pies Sofia was baking that will bear her name and I hope will be offered from now on in her name. The name Sofia is linked to many searches she tried to apply to make sense of a life with too many decimations.

Obviously the departure of loved ones leaves us with a void and grief in which words ring hollow. My good friend was a fighter and tried to keep the misfortunes she faced at bay, but this time it failed her. I remain hopeful that, her face will continue to be present in the memory of all who knew her and those who failed to tell her so. With the exhortation to rejoice in the successes of those around us, to encourage them when they are in danger while they are alive and not when they are already gone. It is a certainty of their memory that we need to remain human and humane.

Ana Rascaru

SATYENDRA NATH BOSE: QUANTUM STATISTICS TO BOSE-EINSTEIN CONDENSATION

Golam Ali Sekh[1*], Benoy Talukdar[2]

[1]*Department of Physics, Kazi Nazrul University, Asansol 713340, WB, India*
[2]*Department of Physics, Visva-Bharati University, Santiniketan 731235, WB, India*
**E-mail: skgolamali@gmail.com*

(Received, 20 September, 2023)

https://doi.org/10.53081/mjps.2023.22-1.01

Abstract

Satyendra Nath (S.N.) Bose is one of the great Indian scientists. His remarkable work on the black body radiation or derivation of Planck's law led to quantum statistics, in particular, the statistics of photon. Albert Einstein applied Bose's idea to a gas made of atoms and predicted a new state of matter now called Bose-Einstein condensate. It took 70 years to observe the predicted condensation phenomenon in the laboratory. With a brief introduction to the formative period of Professor Bose, this research survey begins with the founding works on quantum statistics and, subsequently, provides a brief account of the series of events terminating in the experimental realization of Bose-Einstein condensation. We also provide two simple examples to visualize the role of synthetic spin-orbit coupling in a quasi-one-dimensional condensate with attractive atom-atom interaction.

Keywords: S. N. Bose; black-body spectrum; quantum statistics; cooling and trapping; experimental realization of Bose-Einstein condensation; spin-orbit coupling.

PACS numbers: 01.30.−y; 01.30.Rr; 01.50.−i ; 01.65.+g; 03.75.Nt; 05.30.−d; 67.85.−d

Rezumat

Satyendra Nath (S.N.) Bose este unul dintre marii savanți indieni. Lucrările sale remarcabile dedicate radiației corpului absolut negru sau derivării legii lui Plank au condus la statistica cuantică, în particular, la statistica fotonilor. Albert Einstein a aplicat idea lui Bose la un gaz format din atomi și a prezis o nouă formă a materiei, numită actualmente condensarea Bose-Einstein. A fost nevoie de 70 de ani pentru a observa în laborator fenomenul de condensare prezis. Cu o scurtă introducere în perioada formativă a profesorului Bose, acest studiu de cercetare începe cu lucrările fondatoare privind statistica cuantică și, ulterior, oferă o scurtă descriere a seriei de evenimente care se încheie cu realizarea experimentală a condensării Bose-Einstein. De asemenea, oferim două exemple simple pentru a vizualiza rolul cuplării sintetice spin-orbită într-un condensat cvasi-unidimensional cu interacțiune atractivă atom-atom.

Cuvinte cheie: S. N. Bose; spectrul corpului absolut negru; statistica cuantică; răcirea și captarea, realizarea experimentală a condensării Bose-Einstein; cuplarea spin-orbită.

1. Introduction

At the end of nineteenth century, properties of physical systems would be studied by using (i) classical mechanics, (ii) Maxwell's theory of electromagnetism and (iii) thermodynamics. The developments in (i) - (iii) made people believe that ultimate description of nature had been completed. However, at the turn of the twentieth century such a belief was challenged on two major fronts. First, Albert Einstein developed the special theory of relativity in 1905 and general theory of relativity in 1915. Both these revolutionary theories had profound impact on classical mechanics. In the special theory, the Newtonian formulation of mechanics was shown to be an approximation that applies only at low velocities. The Newtonian concept of an absolute frame of reference as well as the assumption of the separation of space and time was shown to be invalid at high velocities. The general theory of relativity superseded Newton's law of gravitation by providing a geometrical theory for the origin of gravitational force [1].

The other profound developments that led to revolutionary impacts on classical mechanics were quantum physics and quantum field theory formulated by Bohr, Sommerfeld, de Broglie, Heisenberg, Born, Schrödinger and Dirac. This conceptual revolution in physics took place during the first three decades of the twentieth century. The main objective was to explain several microscopic phenomena such as black-body radiation, photoelectric effect, atomic stability and atomic spectroscopy. Classical concepts were inadequate to provide their correct description; we needed a new theory - the so-called quantum theory. The origin of this theory is perhaps embedded in a talk given by Max Planck on December 14, 1900 to the German Physical society on the continuous spectrum of the frequencies of light emitted by an ideal heated body or the so-called black body [2]. Here Planck's immediate concern was to provide a radiation formula that can account for experimentally confirmed prediction of the black-body spectrum. He considered the black body as an ensemble of charged oscillators and derived a formula that reduces to Wien and Rayleigh-Jeans radiation laws in appropriate limits. As is well known, the Rayleigh-Jeans radiation formula when integrated over all frequencies leads to ultraviolet catastrophe. Planck's law gives a way out from this crisis. Since the radiation law as given by Max Planck is based on an educated guess, it was felt that Planck's formula should be derived from the first principle of statistical mechanics. In this context an unknown Indian-Satyendranath Bose, a young physicist from Dacca University (now in Bangladesh) provided a derivation of the Planck's law without reference to classical electrodynamics. The judgement of history on Bose's paper is that it not only laid the foundation stone of quantum statistics but also justified the photon concept of light that Einstein had championed since 1905. Einstein developed Bose's concept further, extended it to monatomic ideal gases, and predicted what is known as the Bose-Einstein condensation. As named by Paul Dirac, particles obeying Bose statistics has come to known as bosons. According to Abraham Pais 'The paper by Bose is the fourth and last of the revolutionary papers of the old quantum theory, the other three being by Planck, Einstein and Bohr [3]. Significantly enough, Bose's name is one of the six which under graduate physics students come across in the course of statistical mechanics - the others being Maxwell, Boltzmann, Einstein, Fermi and Dirac [4].

Satyendra Nath Bose was not an institution builder like Meghnad Saha, Homi Janngi Bhaba, Prasanta Mahalanobis or Shanti Swarup Bhatnagar. Throughout his life he was a professor with profound interest in different branches of science, statistics and mathematics, literature and music. He was very generous, gentle and, particularly, not caring about the glamorous aspects of science. It is, therefore, an interesting curiosity to look back into the formative period of Professor Bose and envisage a pedagogic study to visualize how Bose

statistics led to our current understanding of the so-called Bose-Einstein condensate which has effectively changed our current understanding of matter [5].

2. Remembering the early life of Bose

Satyendranath Bose was born in Calcutta (now called Kolkata) on the first January, 1894 in a high caste Hindu family with two generations of English education behind him. Both his grandfather, Ambika Charan, and father, Surendra Nath, were Government employees in British India. Satyendranath had an inborn talent and would have flourished under any circumstances. But it was a lucky coincidence that he found a congenial atmosphere.

Schooling of little Satyen began at the age of five. His family was then living at north Calcutta. First, he was admitted to 'Normal School' close to their residence and then shifted to the famous Hindu School which had a glorious tradition behind it. Although Satyendranath had varied interest, he was particularly strong in mathematics. The mathematics teacher of the school, Upendranath Bakshi, was a legend. He was quick to recognize the signs of genius in the boy. Once, in a test examination, he gave Satyen 110 marks out of 100; his argument was that, in the answer script, Satyen did not skip any of the alternatives. Mr. Bakshi even believed that one day Satyen would become a great mathematician like Laplace or Cauchy [6].

In the entrance examination of 1909 Satyen stood fifth in order of merit. In addition to mathematics, he did very well in Sanskrit, History and Geography. But he opted for the science course and joined the intermediate science class at the Presidency College. In the intermediate examination of 1911, Styendranath stood first and his illustrious colleagues Meghnad Saha (coming from Dacca College) and Nikhil Ranjan Sen secured the second and third positions respectively. All of them joined the B. Sc. class in the Presidency College and opted for mixed Mathematics. In the B. Sc. Examination of 1913 Satyendranath Bose stood first, Meghnad Saha second, and Nikhil Ranjan third, all in the first class. The same result was repeated in the M. Sc. mixed mathematics examination of 1915 except that Nikhil Ranjan did not appear in the examination in that year. The bright Satyendranath was now ready for a career.

3. Beginning the carrier

After completing the formal education in schools and colleges it was quite natural for Satyen to look for the prospect open before him. In those days jobs were difficult to get. But situation began to change as Sir Asutosh Mookherjee, the mathematician Vice Chancellor of Calcutta University introduced post graduate teaching program at the University. He immediately needed a band of teachers to run the program. In 1916 both Satyendranath and Meghnad were appointed as lecturers in the Applied Mathematics Department. But neither of them felt comfortable with the then Ghosh Professor of the Department, Dr. Ganesh Prasad. With kind permission of Sir Asutosh, both of them were transferred to the Physics Department although their formal training in Physics was up to B.Sc. level only. Bose and Saha were entirely self-taught in Physics. They studied modern Physics on their own and, remarkably enough, they translated Einstein's papers on the theory of relativity from German to English [7]. During 1920s the situation in the Physics Department of the Science College at Calcutta was becoming rather uncomfortable due to inadequacy of technical resources. Meanwhile, Bose was looking for a better opportunity. At that time a new university was established at Dacca and the authorities there were looking for competent teachers. Bose was offered readership. When Sir Asutosh came

to know this, he expressed his willingness to increase Bose's salary. But Bose had already given his words to accept the appointment at Dacca. In 1921 he joined Dacca University. Mr. P. J. Hartog, the vice chancellor of the University gave Bose the task of building a new Department – including setting up of laboratories and teaching advance courses in Physics for B. Sc. Honours and M. Sc. students. Meanwhile, the library was also being equipped with books and journals. Bose taught thermodynamics and Maxwell's theory of Electromagnetism. Just as his first group of students graduated in 1923, Bose received a letter from the University authority notifying that his appointment will not be extended beyond a year. The reason behind such a decision was a conflict between government of India and the provincial government of Bengal regarding fund allocation for the University. This led Bose to a awkward position to keep his appointment. It was under this troubled situation that he wrote his famous paper on the derivation of Planck's law. The story regarding publication of the paper is well documented in the scientific literature. He sent the article for publication to Philosophical Magazine in the beginning of 1924. After six months the editors informed him that the referees had given negative reports. He sent the rejected paper to Albert Einstein. Einstein was impressed; he himself translates it from English to German and submitted for publication in Zeitschrift für Physik with an added note, "In my opinion Bose's derivation of the Planck's formula signifies an important advance. The method used also yields the quantum theory of ideal gas, as I will work out in detail elsewhere." It is perhaps the second sentence which contains the germ of Bose-Einstein condensation observed in the laboratory [8 – 10] after seventy years since the publication of Bose's paper [11]. In this context it will not be an exaggeration to say that it required the genius of Einstein to realise the far-reaching consequence of the work by Bose. During a friendly visit to Dacca in March 1924, Saha brought to Bose's attention about the new attempts by Wolfgang Pauli, and by Albert Einstein and Paul Ehrenfest to derive Planck's law. Saha's visit, perhaps, provided further impetus to Bose for thinking about the interaction of radiation with matter. In fact, this led Bose writing a second paper that he again sent to Einstein. We shall now present Bose's derivation of Plank's law. Needless to say, we shall begin by considering historically significant discoveries that played a key role to explain the spectrum of black body radiation as visualized by Max Planck.

4. Black-body radiation, Planck's law and Bose statistics

(a) The observed Black-body spectrum

It is a common experience that all material bodies when heated emit radiation. The spectrum of black-body radiation represents one of the early experimental results, the theoretical explanation of which ultimately led to quantum ideas. Experimentally, the black-body radiation spectrum was first studied by Tyndall [12]. There are two important terms that are commonly used to characterize the nature of the radiating substance. These are the so-called emissive and absorptive powers. A black body is made up of a substance whose absorptive power is unity. The term black body was coined by Kirchhoff [13].

Figure 1 gives the schematic diagram of the original Tyndall experiment. It consists of the black-body light source, a collimating slit and lens, a prism and focusing lens, and light sensor mounted on a rotating arm. A rotary motion sensor measures the angle. The incandescent light source that emits light through a small cavity is a perfect emitter. When light from the black body is cast through a prism, the observed spectrum is continuous. Different wavelengths of light will project to different angles.

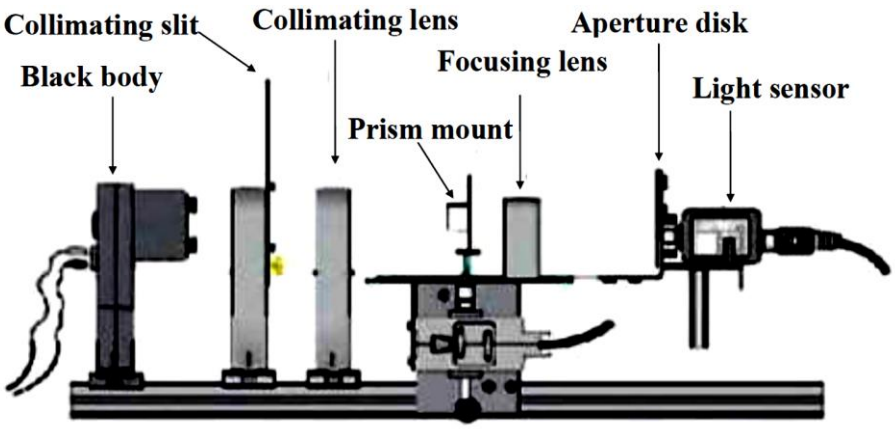

Fig. 1. Diagram for the setup of Tyndall experiment.

In this experiment, parallel light rays travel through the collimating lens, which allows the light rays to remain parallel. Passing through the prism, the light rays refract and project in front of the aperture slit over the light sensor. The light sensor detects and records the light intensity as voltage. So, by measuring the voltage as a function of angle, one can find the intensity of radiation in the spectrum as a function of wavelength.

Figure 2 displays a typical black-body spectrum giving the intensity as a function of wave length. The curves in this figure clearly show that the black-body spectrum is temperature dependent. The intensity of radiation at any given temperature tends to zero at both shorter and longer wavelengths and has a maximum in between. The maximum tends towards shorter wavelength as temperature increases.

(b) Attempts for theoretical explanation

Calculating the black-body curve was a major challenge in theoretical physics during the late nineteenth century because of the following.

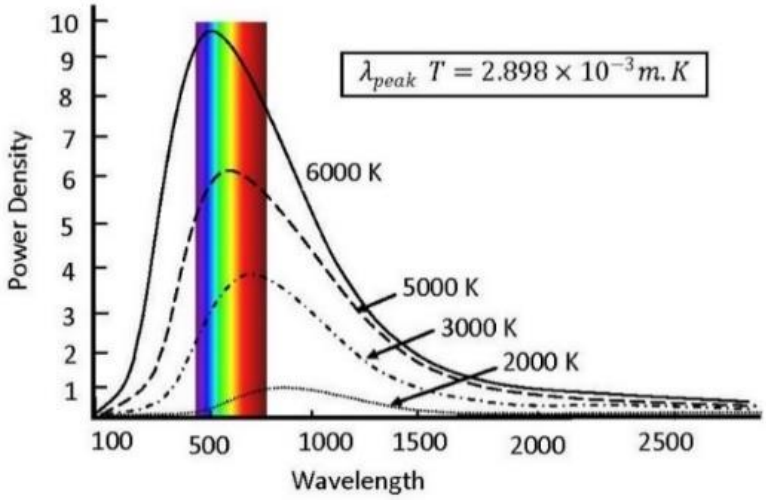

Fig. 2. Black-body spectrum. Power density is measured in the unit of 10^3 W/m^3 and wavelength in nm.

(1) The radiation spectrum is not influenced by factors like the substance of emitting body or condition of its surface. The black-body spectrum is then a pure and ideal case. If one could describe the energy distribution of this ideal case then one would learn something about radiation process in all cases.

(2) It is the basic thermodynamic state of light in which radiation is in thermal equilibrium with a given temperature. Light is an electromagnetic field. The black-body radiation shows that the continuous electromagnetic field can have temperature dependence. This point was not physically realizable at that time.

In view of the above there were attempts to explain the nature of the black-body spectrum by using thermodynamical methods. The thermodynamical consideration of perfect gas led to far-reaching consequences like the discovery of temperature radiation. In this context we note the following similarities between a perfect gas and black-body radiation both of which may be supposed to be confined in enclosures.

(i) In the kinetic theory we assume a perfect gas as being an assembly of particles having all velocities from zero to infinity and moving in all directions.

(ii) In the case of black-body radiation, the radiation also proceeds in all directions and is composed of waves of all lengths.

(iii) The gas molecules in a perfect gas exert pressure on the wall.

(iv) In the case of radiation also, the light waves carry momenta and exert pressure when they are incident on the walls.

Thus, it was tempting to find analogy between black-body radiation and a perfect gas. Studies in the distribution of energy in the black-body spectrum were begun by Wien [14]. The radiation emitted by a black body is not confined to a single wavelength but spreads over a continuous spectrum. The problem was to determine how the energy is distributed over different wavelengths. Wien showed that $E_\lambda d\lambda$ i. e. the amount of energy contained in the spectral region included within the wavelengths λ and $\lambda + d\lambda$ emitted by a black body at a temperature T is of the form

$$E_\lambda d\lambda = \frac{A}{\lambda^5} f(\lambda T) d\lambda. \qquad (1)$$

Using $\lambda = c/\nu$, Eq. (1) can be written in the equivalent form

$$v_\nu d\nu = B\nu^3 \varphi\left(\frac{\nu}{T}\right) d\nu \qquad (2)$$

with v_ν, the energy density of the radiation having frequency ν. This expression was obtained from purely thermodynamical consideration applied on a Gedanken experiment which involves a spherical enclosure having perfectly reflecting walls capable of slowly moving outwards. The enclosure was assumed to be maintained at some temperature and a small black-body of negligible heat capacity was placed inside it. Formula in Eq. (1) was derived by considering thermal equilibrium between the two. As a consequence of adiabatic expansion Wien could deduce

$$\lambda T = \text{Constant}/ \qquad (3)$$

Equation (3) is often called the displacement law [2,14]. The physical interpretation of the law is that if radiation of a particular wavelength at a certain temperature is adiabatically altered to another wavelength, then the temperature changes in the inverse ratio. Wien also made assumptions regarding the mechanism for emission and absorption of radiation. The radiation inside a hallow enclosure was supposed to be produced by a resonator of molecular dimension and the frequency of the wave emitted is proportional to the kinetic energy of the resonators. The resonators were supposed to obey the Boltzmann statistics [15]. This consideration converts the energy distribution law in Eq. (1) in the form

$$E_\lambda d\lambda = \frac{A}{\lambda^5} e^{-c_2/\lambda T} d\lambda, \qquad (4)$$

where $c_2 = \alpha\, c/k_B$ and α, constant.

Let us now try to see to what extent the formula in Eq. (3) can explain the experimental black-body spectrum. For given values of c_2 and A, E_λ vanishes at $\lambda = 0$ and $\lambda = \infty$. Thus, it appears that the energy distribution law in (3) is a good candidate to explain black-body spectra as given in figure 2. More specifically,

(i) Paschen [16] working with light of short wavelength verified that Wien's formula fits the data for short waves.

(ii) On the other hand, Lummer and Pringshiem [17] working with long waves and high temperature found considerable disagreement of the theoretical values from the experimental results.

In the above context we note that thermodynamical consideration could not give any improved expression for $f(\lambda T)$ to fit the experimental data. Wien discovered his energy distribution law in 1893. After seven years Lord Rayleigh [18] attempted to find an energy distribution function by the use of classical electromagnetic theory. The work was completed by Sir James Jeans [19]. The law discovered by them goes by the name Rayleigh-Jeans law. To derive the law, they considered a black body chamber in the form of a parallelepiped with perfectly reflecting walls. Also, they assumed that there is a black particle inside. In the course of time the enclosure will be filled with stationary waves of all lengths, for the particle emits radiation which is reflected back by the wall. The reflected and incident waves interfere and form stationary waves.

The black body chamber is filled with diffuse radiation of all frequencies between 0 to $\propto$. Using the above picture Lord Rayleigh found out the number of possible wave motion having their frequencies between ν and $\nu + d\nu$. The number of vibrations per unit volume was calculated as $\frac{4\pi\nu^2}{c^3} d\nu$.

Since electromagnetic waves are transverse, they can be polarized and each polarized component is independent of the other. Thus, the required number of vibrations per unit volume is $\frac{8\pi\nu^2}{c^3} d\nu$. Converting frequency into wavelength the number becomes

$$\frac{8\pi}{\lambda^4} d\lambda. \qquad (5)$$

The energy of each vibration is $k_B T$. In view of this the energy distribution law obtained by Rayleigh and Jeans is given by

$$E_\lambda d\lambda = \frac{8\pi}{\lambda^4} k_B T\, d\lambda \qquad (6).$$

The distribution in Eq. (6) can account for the long wavelength part of the black-body spectrum. For smaller values of λ, E_λ tends to $\propto$. This is the so-called ultraviolet catastrophe. This implies that if the black body chamber is initially filled with infrared radiation, finally it will be filled up with ultraviolet radiation. Thus, we see that neither of the radiation formulas, one given by Wien and other given by Rayleigh and Jeans, can explain the black-body spectrum. Therefore, explanation of the black-body spectrum using theoretical consideration assumed the status of an unsolved problem.

(*c) Planck's Law of black-body radiation*

Planck [20] imagined that a black-body radiation chamber is filled up not only with radiation, but also with the molecules of a perfect gas. At that time, the exact mechanism of

generation of light by atomic vibrations or of absorption of light by atoms and molecules was unknown. Planck, therefore, introduced resonators of molecular dimensions as the via media between radiation and gas molecules. These resonators absorb energy from the radiation, and transfer energy partly or wholly to the molecules when they collide with them. In this way thermodynamical equilibrium is established.

The resonators introduced by Planck were dipole oscillators which may be described as Hertzian oscillators of molecular dimensions such that the density v_ν of radiation of frequency ν could be written as

$$v_\nu = \frac{8\pi\nu^2}{c^3} E_\nu \,, \tag{7}$$

where v_ν is the mean energy of a resonator emitting the radiation. According to classical idea $E_\nu = k_B\, T$. As a result, the expression in Eq. (7) gives the Rayleigh-Jeans law which is inconsistent with the experimental data. Planck abandoned the hypothesis of continuous emission of radiation by resonators, and assumed that they emit energy only when the energy is an integral multiple of certain minimum energy ϵ. As we know currently, this assumption is equivalent to light quantum hypothesis of Einstein [21]. In any case, let us try to calculate the mean energy of these resonators. The probability that a resonator will possess the energy E is $exp(-E/k_BT)$. Let $N_0,\ N_1,\ N_2, \dots, N_r, \dots.$ be the number of resonators having energies $0, \epsilon, 2\epsilon, 3\epsilon, \dots\dots, r\epsilon, \dots.$ Then we have

$$N = N_0 + N_1 + N_2 + \cdots + N_r + \cdots, \tag{8}$$

and

$$E = \epsilon[N_1 + 2N_2 + 3N_3 + \cdots + rN_r + \cdots] \tag{9}$$

with

$$N_r = N_0 e^{-r\epsilon/k_BT} \tag{10}$$

Using Eq. (10) in (8) we get

$$N = \frac{N_0}{1-\exp[-\frac{\epsilon}{k_BT}]}\,. \tag{11}$$

Again using Eq. (10) in (9) we get,

$$E = \epsilon N_0 \frac{\exp[-\epsilon/k_BT]}{(1-\exp[-\epsilon/k_BT])^2}. \tag{12}$$

Dividing Eq. (12) by (11) we can write

$$\frac{E}{N_0} = \frac{\epsilon}{\exp\left[-\frac{\epsilon}{k_BT}\right]-1}. \tag{13}$$

We know from the law of equipartition of energy that the mean energy of a resonator is k_BT. This result agrees with that given in Eq. (13) only at an extremely high temperature. The energy assigned to the resonators, namely, $0, \epsilon, 2\epsilon, 3\epsilon, \dots\dots, r\epsilon, \dots.$ correspond to the light quantum hypothesis in that resonators can have only discrete set of energies. Thus, the mean energy given in Eq. (13) is a quantum law. Using Eq. (13) in Eq. (7) we get the energy density inside the enclosure as

$$u_\nu d\nu = \frac{8\pi\nu^2}{c^3} \frac{\epsilon\, d\nu}{\exp\left[-\frac{\epsilon}{k_BT}\right]-1}. \tag{14}$$

Comparing Eq. (14) with (2), the Wien's distribution law, we see that ϵ must be proportional to ν. In view of this, Planck took $\epsilon = h\nu$, where h is the so-called Planck's constant. Thus

$$u_\nu d\nu = \frac{8\pi h\nu^3}{c^3} \frac{d\nu}{\exp\left[-\frac{h\nu}{k_BT}\right]-1}. \tag{15}$$

Using $d\nu = -\frac{c}{\lambda^2}d\lambda$, we get

$$u_\lambda d\lambda = \frac{8\pi hc}{\lambda^5}\frac{d\lambda}{\exp\left[-\frac{ch}{\lambda k_B T}\right]-1}. \quad (16)$$

Equation (16) is known as the Planck's law of radiation. In the short wavelength limit Eq. (16) gives the Wiens distribution law and in the long wavelength limit we get Rayleigh-Jeans law. Thus, the Planck's formula could explain the black -body spectrum satisfactorily.

Planck's hypothesis that resonators can have only discrete energies resolved the essential mysteries of the black-body radiation. The subsequent works of Einstein on the photoelectric effect and of Compton on the scattering of X-rays established the discrete or quantum nature of radiation [22]. Thus, Planck's work is a statement of quantum hypothesis of light. A quantum of radiation goes by the name photon. It was then natural to look for derivation of Planck radiation formula by treating the black-body radiation as a gas of photons in a similar way as Maxwell derived his distribution law for a gas of conventional molecules. But a gas of photons differs radically from a gas of conventional molecules because Maxwell's molecules are classical objects while photon is a purely quantum mechanical concept and is thus indistinguishable. In this context Bose derived a Statistics for indistinguishable particles (quantum statistics) and made use of it to deduce Planck's formula. In his historic paper of 1924, Bose [11] treated black-body radiation as a gas of photons; however, instead of considering the allocation of the "individual" photons to the various energy states of the system, he fixed his attention on the number of states that contained a particular number of photons. We shall try to elucidate this point in some detail.

(d) Bose Statistics

Let us try to calculate the distinct number of ways in which N_s indistinguishable particles can be distributed in A_s indistinguishable boxes. We refer to these boxes as cells since they represent minimum volume in the phase space when we apply this method for the derivation of Planck's law. Let the cells be designated as $x_1, x_2, x_3 \ldots\ldots, x_{A_s}$. A particular distribution can be represented by

$$x_1^\alpha x_2^\beta \ldots\ldots\ldots x_{A_s}^\gamma, \quad (17)$$

where $\alpha, \beta, \ldots\ldots\ldots, \gamma$ are the number of particles in the cells $x_1, x_2, \ldots\ldots x_{A_s}$ respectively. Clearly,

$$\alpha + \beta + \cdots + \gamma + \cdots = N_s. \quad (18)$$

Now consider the product

$$(x_1^0 + x_1^1 + x_1^2 + \cdots x_1^r + \cdots)(x_2^0 + x_2^1 + x_2^2 + \cdots x_2^r + \cdots) \ldots \left(x_{A_s}^0 + x_{A_s}^1 + x_{A_s}^2 + \cdots x_{A_s}^r + \cdots\right), \quad (19)$$

where each factor consists of an infinite number of terms. In this product we have all possible combinations of the powers of $x_1, x_2, x_3 \ldots\ldots, x_{A_s}$. Hence the number of ways of distributing N_s particles in the A_s cells is equal to the number of those terms of type (17) for which the condition (18) is satisfied.

Now let $x_1 = x_2 = x_3 = \cdots = x_{A_s} = x$. The number of combinations in which the N_s indistinguishable particles can be distributed in A_s cells is equal to the coefficient of x^{N_s} in this expression

$$(x^1 + x^2 + x^3 + \cdots + x^r + \cdots)^{A_s} = (1 - x)^{-A_s}. \quad (20)$$

Thus, the number of ways in which N_s number of indistinguishable particles can be distributed in A_s indistinguishable cells is

$$\frac{(A_s+N_s-1)!}{(A_s-1)!\,N!}. \quad (21)$$

This is the so-called Bose statistics.

e) Bose's deduction of Planck's law

A black-body chamber may be supposed to be full of photons in thermal equilibrium. The problem of finding spectral distribution of energy then reduces to that of finding the number of photons possessing energy $h\nu$ in a black-body chamber having temperature T. Bose realized the problem in this way and gave a very powerful method for the derivation of Planck's law [23]. According to quantum hypothesis, a radiation of frequency ν consists of photons of energy $h\nu$. The photons move in all possible directions with the constant velocity c and momentum $h\nu/c$. Thus

$$p_x = \frac{h\nu_x}{c}, p_y = \frac{h\nu_y}{c} \text{ and } p_z = \frac{h\nu_z}{c} \quad (22)$$

such that

$$p_x^2 + p_y^2 + p_z^2 = \frac{h^2\nu^2}{c^2}. \quad (23)$$

Let us now find out the phase space volume described by the photons within the energy layers $h\nu_s$ and $h(\nu_s + d\nu_s)$. This is given by

$$G_s = \int \ldots \int dx\, dy\, dz\, dp_x dp_y dp_z \quad (24)$$

with $G_s = V\frac{4\pi h^3\nu_s^2}{c^3}\, d\nu_s$. This is the phase space volume at the disposal of the photons in the energy range $h\nu_s$ and $h(\nu_s + d\nu_s)$. But each photon has a phase volume h^3. Thus, the number of cells per unit volume

$$A_s d\nu_s = \frac{4\pi\nu_s^2 d\nu_s}{c^3}. \quad (25)$$

Since two photons are distinguished by their state of polarization from each other, instead of (20) we must write

$$A_s d\nu_s = \frac{8\pi\nu_s^2 d\nu_s}{c^3}. \quad (26)$$

The result in Eq. (26) is in agreement with that in (7) obtained by Rayleigh. Let the number of photons of frequency between ν_s and $(\nu_s + d\nu_s)$ be denoted by $N_s d\nu_s$. We have then to find out the number of ways in which the $N_s d\nu_s$ oscillators can be distributed amongst the $A_s d\nu_s$ cells. We make supposition that each cell may contain $1,2,3, \ldots, r, \ldots$ upto $N_s d\nu_s$ photons. Then we get

$$W = \prod_s \frac{(A_s+N_s)d\nu_s!}{A_s d\nu_s!\, N_s d\nu_s!}, \quad (27)$$

according to Bose statistics in Eq. (21), as the probability of $N_s d\nu_s$ indistinguishable particles to be distributed in $A_s d\nu_s$ cells. Using W in the Boltzmann relation between entropy and probability

$$S = k_B \ln W \quad (28)$$

we get

$$S = k_B \sum \ln \frac{(A_s+N_s)d\nu_s!}{A_s d\nu_s!\, N_s d\nu_s!}. \quad (29)$$

To obtain the law of distribution, Bose optimized the entropy subject to the constraint

$$E = \sum_s (N_s d\nu_s) h\nu_s, \text{ Constant} \quad (30)$$

which imply that the total energy E of the photon gas is conserved. From (28) we have

$$\delta \sum_s [(A_s + N_s)\ln(A_s + N_s) - A_s \ln A_s - N_s \ln N_s] = 0, \quad (31)$$

using Stirling's formula

$$\ln n! \approx n \ln n - n. \tag{32}$$

Accommodating the energy constraint

$$\sum \nu_s \delta N_s = 0 \tag{33}$$

through the method of Lagrange undetermined multiplier, we get

$$N_s = \frac{A_s}{e^{\alpha \nu_s - 1}}. \tag{34}$$

Here α, is the undetermined multiplier. Using $\alpha = \frac{h}{k_B T}$, Eq. (34) becomes

$$N_s = \frac{A_s}{e^{h\nu_s/k_B T - 1}}. \tag{35}$$

From Eq. (26) and the fact that the energy density

$$\rho_{\nu_s} d\nu_s = N_s h\nu_s d\nu_s, \tag{36}$$

we get the Planck's result

$$\rho d\nu = \frac{8\pi\nu^2 d\nu}{c^3} \frac{h\nu}{e^{h\nu/k_B T - 1}}. \tag{37}$$

We remember that Planck deduced this law by making use of hypothetical molecular resonators of discrete energies. On other hand, the treatment of Bose explicitly demonstrates that the concept of photons can be used to derive the Planck's law. In this way Bose's treatment provided a definitive proof for the light quantum hypothesis.

V. On the realization of Bose-Einstein conensation

(a) Einstein's quantum theory of ideal gas

We have seen how Bose derived his statistics for the probability of distributing N_s indistinguishable particles in A_s cells. This remarkable result provided a natural basis to deduce Planck's radiation law for the explanation of black-body spectrum without taking recourse to the use of classical electromagnetic theory. Bose's derivation of Planck's formula is an application of his statistics to massless particles. Einstein [24] recognized that the method employed by Bose can also be generalized to deal with massive particles and thus have a quantum theory for the ideal gas. To derive this quantum mechanical theory let us consider a gaseous system of N noninteracting indistinguishable particles confined in a volume V and sharing a given energy E. The statistical quantity of interest in this case is the number of distinct microstates $\Omega(N, V, E)$ accessible to the system characterized by (N, V, E). For large V, the single particle energy levels in the system are very close to one another. Thus, we may divide the energy spectrum into a large number of groups of levels which may be referred to as the energy cells. This is schematically shown in figure 3.

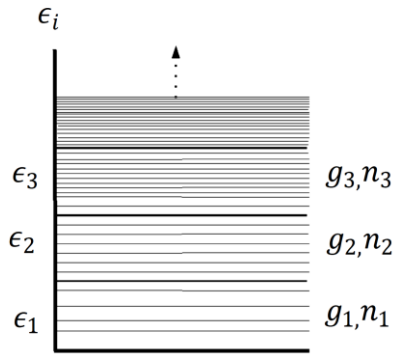

Fig. 3. Distribution of particles in the energy cells.

Let n_i be the number of particles in the i^{th} cell. Clearly, the set $\{n_i\}$ will satisfy the conditions

$$\sum_i n_i = N \tag{38}$$

and $$\sum_i n_i\, \varepsilon_i = E \tag{39}$$

with ε_i, the average energy of a level. If $W\{n_i\}$ stands for the number of distinct microstates associated with the distribution set $\{n_i\}$, then the number of distinct microstates accessible to the system will be given

$$\Omega(N,E,V) = \sum_{\{n_i\}} W\{n_i\}\,. \tag{40}$$

The summation in Eq. (40) is taken over all distinct sets that obey the conditions in Eqs. (38) and (39). Again if $w(i)$ is the number of distinct microstates associated with the i^{th} cell of the spectrum, then

$$W\{n_i\} = \prod_i w(i). \tag{41}$$

Bose statistics tells us that

$$w(i) = \frac{(n_i+g_i-1)!}{n_i!(g_i-1)!}, \tag{42}$$

where $g_i$is the number of levels in the i^{th} cell. Then

$$W\{n_i\} = \prod_i \frac{(n_i+g_i-1)!}{n_i!(g_i-1)!}. \tag{43}$$

The entropy of the system is given by

$$S(N,V,E) = k\, ln\, \Omega\,(N,V,E) = k\, ln\left[\sum_{\{n_i\}} W\{n_i\}\right]. \tag{44}$$

The expression in Eq. (44) can be replaced by

$$S(N,V,E) \approx k\, ln\, W\,\{n_i^*\}, \tag{45}$$

where $\{n_i^*\}$ is the distribution set that maximizes the number $W\{n_i\}$; the numbers n_i^* are clearly the most probable values of the distribution number n_i. The maximization should be carried out under the constraints implied by Eqs. (38) and (39). Thus

$$\delta\, ln\, W\,\{n_i\} - [\alpha \sum_i \delta n_i + \beta \sum_i \varepsilon_i \delta n_i] = 0, \tag{46}$$

where α and β are Lagrange's undetermined multipliers.
Now

$$ln\, W\,\{n_i\} = ln \prod_i w(i) \; = \sum_i ln\, w\,(i) \tag{47}$$

Using Stirling's formula $ln\, x\,! = x\, ln\, x - x$, we can write
from Eqs. (42) and (47)

$$ln\, W\,\{n_i\} \approx \sum_i \left[n_i\, ln\left(\frac{g_i}{n_i}+1\right) + g_i\, ln\left(1+\frac{n_i}{g_i}\right)\right], \tag{48}$$

From Eqs. (46) and (48) we get

$$n_i^* = \frac{g_i}{e^{\alpha+\beta\varepsilon_i}-1}. \tag{49}$$

Equivalently,

$$\frac{n_i^*}{g_i} = \frac{1}{e^{\alpha+\beta\varepsilon_i}-1}. \tag{50}$$

may be interpreted as the most probable number of particles per energy level in the i^{th} cell. It is important to note that the final result in Eq. (50) is totally independent of the manner in which the energy levels of the particles are grouped into the cells so long as the number of levels in each cell is sufficiently large. From Eqs. (45), (48) and (49), the entropy of the gas is given by

$$\frac{S}{k} = \sum_i \left[n_i^*(\alpha+\beta\varepsilon_i) - g_i\, ln\left(1-e^{-\alpha-\beta\varepsilon_i}\right)\right] = \alpha N + \beta E - \sum_i g_i\, ln\left(1-e^{-\alpha-\beta\varepsilon_i}\right). \tag{51}$$

From Eq. (51) we write

$$\frac{S}{k} = \beta\left[\frac{\alpha}{\beta}N + E - \frac{1}{\beta}\sum_i g_i\, ln\left(1-e^{-\alpha-\beta\varepsilon_i}\right)\right]. \tag{52}$$

Equation (52) in conjunction with the second law of thermodynamics gives $\beta = 1/kT$ and $\alpha =$

$-\mu/kT$, where μ stands for the chemical potential defined as $\mu = \left(\frac{\partial E}{\partial N}\right)_{V,T}$.

As we noted the result in Eq. (50) is independent of the manner in which the energy levels of the particles are grouped into cells so long as the number of levels in each cell is sufficiently large. In view of this, we use the value of α and β in Eq. (50) and get the mean occupation number of the level ε in the form

$$\langle n_\varepsilon \rangle = \frac{1}{e^{(\varepsilon-\mu)/kT}-1} \ . \tag{53}$$

From Eq. (53) it is clear that for the mean occupation number to be positive, $\mu < \varepsilon$ for all values of ε. When μ becomes equal to the lowest value of ε, say ε_0, the occupancy of that particular level becomes infinitely high. This implies that all particles in the gaseous states can go to the lowest energy state. For temperatures at which

$$e^{(\varepsilon-\mu)/kT} >> 1. \tag{54}$$

The gaseous particles obey the Maxwell-Boltzmann statistics given by

$$\langle n_\varepsilon \rangle_{M,B} = e^{(\mu-\varepsilon)/kT}. \tag{55}$$

Equation (54) tells us that the chemical potential of the system must be negative. Thus, the fugacity $z = e^{\mu/kT}$of the system must be smaller than unity. The quantity z reflects the tendency of a substance to prefer one phase to another and can literally be defined as the tendency to escape. Moreover, in a quantum mechanical theory z is related to N and V by

$$\frac{N}{V} = z\frac{(2\pi mkT)^{3/2}}{h^3}. \tag{56}$$

In terms of the de Broglie wavelength

$$\lambda = \frac{h}{\sqrt{2\pi mkT}} \tag{57}$$

Eq. (56) can be written as

$$\frac{N}{V} = \frac{z}{\lambda^3}. \tag{58}$$

From Eq. (58), z to be less than unity we must have

$$\frac{\lambda^3 N}{V} << 1. \tag{59}$$

The quantity $n\lambda^3$ $(n = N/V)$ is an appropriate parameter in terms of which the various physical properties of the system can be addressed. For example, one can consider three cases (i) $n\lambda^3 -> 0$: In this case $\lambda -> 0$ such that the particle aspect of the gas molecules or atoms dominates over the wave aspect. Obviously, the system is classical. (ii) $1 > n\lambda^3 >$: We can expand all physical quantities as a power series in that parameter and investigate how the system tends to exhibit non-classical or quantum behavior. (iii) $n\lambda^3 \approx 1$: The system becomes significantly different from the classical one and the typical quantum effects dominate.

From Eq. (57) we write

$$n\lambda^3 = \frac{nh^3}{(2\pi mkT)^{3/2}}. \tag{60}$$

This expression clearly shows that the system is more likely to display quantum behavior when it is at a relatively low temperature or has a relatively high density of particles. Moreover, for smaller particle mass, the quantum behavior will be more prominent. From Eq. (53) the total number of particles N in the system is obtained as

$$N = \sum_\varepsilon \langle n_\varepsilon \rangle = \sum_\varepsilon \frac{1}{z^{-1}e^{\beta\varepsilon}-1}. \tag{61}$$

For a large volume V, the spectrum of the single-particle state is almost continuous such that the summation on the right side of Eq.(61) can be replaced by integration. The density of states in the neighborhood of ε is given by

$$\rho(\varepsilon)d\varepsilon = \frac{2\pi V}{h^3}(2m)^{3/2}\varepsilon^{1/2}d\varepsilon \quad (62)$$

so that

$$\frac{N}{V} = \frac{2\pi}{h^3}(2m)^{3/2}\int_0^\infty \frac{\varepsilon^{1/2}d\varepsilon}{z^{-1}e^{\beta\varepsilon}-1} + \frac{1}{V}\frac{z}{1-z}. \quad (63)$$

In writing Eq. (63) we have separated out the $\varepsilon = 0$ term in Eq. (61) which has a statistical weight equal to one. Denoting $\frac{z}{1-z}$ by N_0 we write Eq. (63) in the form

$$\frac{N-N_0}{V} = \frac{2\pi}{h^3}(2\pi mkT)^{3/2}\int_0^\infty \frac{x^{1/2}dx}{z^{-1}e^{x}-1} \quad (64)$$

with $x = \beta\varepsilon$. In terms of Bose-Einstein functions

$$b_\nu(z) = \frac{1}{\Gamma(\nu)}\int_0^\infty \frac{x^{\nu-1}dx}{z^{-1}e^{x}-1} = z + \frac{z^2}{2^\nu} + \frac{z^3}{3^\nu} + \ldots . \quad (65)$$

The result in Eq. (64) can be written as

$$\frac{N-N_0}{V} = \frac{1}{\lambda^3}b_{3/2}(z). \quad (66)$$

The quantity $(N - N_0)$ denotes the number of particles (N_e) in the excited states. Therefore,

$$N_e = V\left(\frac{2\pi mkT}{h^2}\right)^{3/2} b_{3/2}(z). \quad (67)$$

The function $b_{3/2}(z)$ increases monotonically and is bounded with the largest value

$$b_{\frac{3}{2}}(z) = 1 + \frac{1}{2^{\frac{3}{2}}} + \frac{1}{3^{\frac{3}{2}}} + \cdots \ldots = \zeta(3/2) = 2.812. \quad (68)$$

Hence, for all z of interest

$$b_{3/2}(z) \leq \zeta(3/2). \quad (69)$$

In view of Eq. (69) N_e in Eq. (67) will satisfy the condition

$$N_e \leq V\left(\frac{2\pi mkT}{h^2}\right)\xi(3/2). \quad (70)$$

The quantity in Eq. (70) gives the maximum number of particles in the excited states. If the actual number of particles N of the system exceeds this limiting value, then N_0 number of particles given by

$$N_0 = N - V\left(\frac{2\pi mkT}{h^2}\right)^{3/2}\zeta(3/2) \quad (71)$$

will be pushed into the ground state. Since $N_0 = z/(z-1)$, the precise value of z can be determined using

$$z = \frac{N_0}{N_0-1} \approx 1. \quad (72)$$

For z to be one, the chemical potential μ must be zero. Thus from Eq. (53),$\langle n_e\rangle = \frac{1}{e^{\epsilon/KT}-1}$. This result shows that for large N, there is no limit to the number of particles that can go onto the ground state $\varepsilon = 0$. This curious phenomenon of a macroscopically large number of particles accumulating in a single particle state $\varepsilon = 0$ is referred to as Bose-Einstein condensation. It is purely of quantum mechanical origin and takes place in the momentum space.

The condition for the onset of Bose-Einstein condensation is

$$N > N_e \quad (73)$$

which gives a critical value of temperature

$$T_c = \frac{h^2}{2\pi mk}\left(\frac{N}{V\zeta(3/2)}\right)^{2/3}. \quad (74)$$

For given values of N and V Bose-Einstein condensation takes place when temperature T of the gas is less than T_c.

(b) Physical picture of condensate formation

An atom of mass m at temperature T can be regarded as a quantum mechanical wave packet that has spatial extension of the thermal de Broglie wave length $\lambda = /\sqrt{2\pi mkT}$ given in Eq. (57). From this expression for λ one can study the physical changes that occur in the ideal gas as one gradually lowers the temperature. (i) As long as the temperature is high, the wave packet is very small such that we can use the classical concept for the trajectory of the wave packet. At such temperatures we imagine atoms as billiard balls that move in the container and occasionally collide. Atoms are distinguishable. This is shown in figure 4(a). (ii) As the temperature is lowered the wave length increases and the wave aspect of atoms tends to compete with the particle aspect. This is shown in figure 4(b). (iii) At $T = T_c$ given in Eq. (74) the individual wave packets overlap and we have identity crisis.

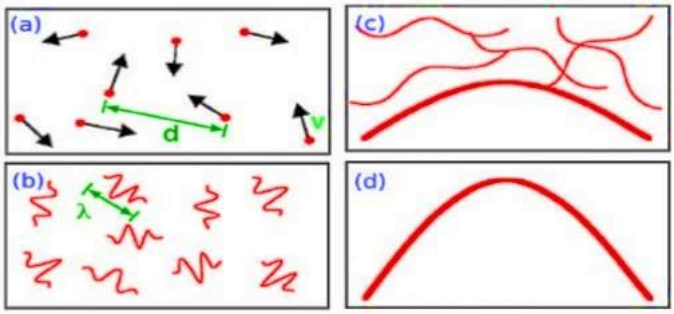

Fig. 4. Physical changes of atoms during the formation of Bose-Einstein condensation.

The wave packets no longer follow the classical trajectories. At that point indistinguishability becomes important and we need quantum statistics. When quantum indistinguishability dominates, there is a transition to a new phase of matter. The particles come together in a single state and they behave as one big matter wave as shown in figure 4 (c). This is the onset of Bose-Einstein condensation. (iv) At $T = 0$, we get a pure Bose condensate or a giant matter wave. This is shown in figure 4(d).

It is now clear that the phenomenon of Bose-Einstein condensation, as demonstrated by Einstein, is a consequence of quantum statistics associated with indistinguishability of particles. Naturally, in this context, a very important question arose: What kind of particles obeys Bose statistics and is likely to undergo a phase transition leading to Bose-Einstein condensation? Immediately, after the demonstration of BEC by Einstein, Pauli exclusion principle was formulated. Only after one year the Fermi-Dirac statistics was proposed. Pauli and Dirac thought that all massive particles in the world obey Fermi-Dirac statistics and are fermions. If this was true, Bose-Einstein condensation would never be observed. This was a remark made by Pauli. Meanwhile, Dirac remarked that photons which obey Bose statistics have symmetric wave functions. Thus, particles which are likely to undergo Bose-Einstein condensation at $T < T_c$ must have symmetric wave functions. Understandably, elementary particles (not the carrier of energy) cannot have symmetric wave functions since they are fermions. But there is no bar for composite particles like atoms to undergo Bose-Einstein condensation provided these atoms have integral spins. The total spin of a Bose particle must be an integer, and therefore a boson made up of fermions must contain an even number of them. Neutral atoms contain equal numbers of electrons and protons, and therefore the statistics that an atom obeys is determined solely by the number of neutrons: if N is even, the atom is a boson, and if it is odd, a fermion. Since the alkalis

have odd atomic number Z, boson alkali atoms have odd mass numbers A. Likewise for atoms with even Z, bosonic isotopes have even A. In **Table I** we list N, Z and the nuclear spin quantum number I for some alkali atoms and hydrogen.

Table I. The proton number Z, the neutron number N, the nuclear spin I.

Isotope	Z	N	I
^{1}H	1	0	½
^{6}Li	3	3	1
^{7}Li	3	4	3/2
^{23}Na	11	12	3/2
^{39}K	19	20	3/2
^{40}K	19	21	4
^{41}K	19	22	3/2
^{85}Rb	37	48	5/2
^{87}Rb	37	50	3/2
^{133}Cs	55	78	7/2

To date, most experiments on Bose-Einstein condensation have been made with states having total electronic spin 1/2. The majority of these have been made with atoms having nuclear spin I = 3/2 (^{87}Rb, ^{23}Na, and ^{7}Li), while others have involved I = 1/2 (H) and I = 5/2 (^{85}Rb). In addition, Bose-Einstein condensation has been achieved for four species with other values of the electronic spin, and nuclear spin I = 0: $^{4}He^{*}$ (^{4}He atoms in the lowest electronic triplet state, which is metastable) which has S = 1, ^{170}Yb and ^{174}Yb (S = 0), and ^{52}Cr (S = 3).

The ground-state electronic structure of alkali atoms is simple: all electrons but one occupies closed shells, and the remaining one is in s-orbital in a higher shell. In **Table II** we list the ground-state electronic configurations for alkali atoms. The nuclear spin is coupled to the electronic spin by the hyperfine interaction. Since the electrons have no orbital angular momentum (L = 0), there is no magnetic field at the nucleus due to the orbital motion, and the coupling arises solely due to the magnetic field produced by the electronic spin.

Table II. The electron configuration and electronic spin for selected isotopes of alkali atoms and hydrogen.

Element	Z	Electronic Spin	Electronic Configuration
H	1	1/2	$1s^1$
Li	3	1/2	$1s^2 2s^1$
N*a*	11	1/2	$1s^2 2s^2 p^6 3s^1$
K	19	1/2	$1s^2 2s^2 p^6 3s^2 3p^6 4s^1$
R*b*	37	1/2	(Ar) $3d^{10} 4s^2 4p^6 5s^1$
Cs	55	1/2	(Kr)$4d^{10} 5s^2 5p^6 6s^1$

(c) Steps towards experimental realization

It is now appropriate to ask the question: What are the requirements for observing BEC in the laboratory? We have pointed out that alkali metal atoms are bosons. Thus, any experiment for observation of BEC should start with a gas of alkali metal atoms at the room temperature. The gaseous system should be precooled, trapped and cooled to a temperature preferably below the

critical temperature and then imaged to get the signature of BEC. In fact, the first three experiments on BEC used dilute atomic gases of rubidium [8], lithium [9] and sodium [10]. It is true that BEC was first observed in these three experiments. However, it appears that superfluidity in helium was considered by London as early as 1938 as a possible manifestation of BEC. However, evidence for BEC in helium was found much later from the analysis of momentum distribution of the atoms measured in neutron-scattering experiment [25]. On the other hand, in a series of experiments hydrogen atoms were first cooled in a dilute refrigerator, then trapped by magnetic field and further cooled by evaporation. This approach has come very close to observing BEC. The main problem in observing BEC in this system comes from the fact that the hydrogen atoms, rather than being in atomic state, form molecules [26].

In the 1980's laser-based techniques were developed to trap and cool neutral atoms [27]. Technically, trapping and cooling in this approach go by the names magnetooptical trapping and laser cooling. Alkali metal atoms are well suited to laser-based methods because their optical transitions can be excited by available lasers and because they have a favorable internal energy-level structure for cooling to very low temperatures. Once they are trapped, their temperature can be lowered further by evaporative cooling. Let us first briefly outline what are the effects of trapping on the atomic system and how atoms are trapped.

(i) The effects of trapping

The number of atoms that can be put into the trap is not truly macroscopic such that the thermodynamic limit is never achieved. We, therefore, begin by considering the effect of finite particle numbers on T_c, the critical temperature for the onset of Bose-Einstein condensation. The expression for T_c in Eq. (74) refers to *N* (very large) number of particles confined in a three-dimensional box. If instead we consider the atoms to be confined in a three-dimensional harmonic well, the expression for T_c modifies to

$$T_c = \frac{\hbar\bar{\omega}N^{1/3}}{[\zeta(3)]^{1/3}}, \tag{75}$$

where $\bar{\omega} = (\omega_1\omega_2\omega_3)^{1/3}$, ω be the classical oscillator frequency. In this context we note that in most cases the confining traps are well approximated by harmonic potentials. When the number of particles is extremely high, we can neglect the zero-point energy in the harmonic trap. This is, however, not true when the system consists of finite number of atoms. The finiteness of the number of particles calls for zero-point energy to be taken into account. This reduces the critical temperature by an amount ΔT_c such that

$$\frac{\Delta T_c}{T_c} = -\frac{\zeta(2)}{2[\zeta(3)]^{2/3}}\frac{\omega_m}{\bar{\omega}}N^{-1/3}. \tag{76}$$

where $\omega_m = (\omega_1 + \omega_2 + \omega_3)/3$. Clearly, from Eq. (76) $\frac{\Delta T_c}{T_c} -> 0$, as $N -> \infty$. Thus, we see that one of the effects of trapping is to lower the critical temperature by confining a finite number of atoms. Besides finiteness of the system trapping makes the Bose gas inhomogeneous such that density variation occurs on a characteristic length scale, $a_{ho} = \sqrt{\hbar/(m\omega_m)}$, provided by the frequency of the trapping oscillator. This is a major difference with respect to other systems like the super fluid helium where the effects of inhomogeneity take place on a microscopic scale in the coordinate space. Inhomogeneity of super-fluid helium, in fact cannot be detected in the coordinate space such that all observations are made in the momentum space. As opposed to this, the inhomogeneity of the Bose gas is such that both coordinate and momentum spaces are equally suitable for observations.

In the above we talked about harmonic confinement. Physically such confinements are achieved by applying appropriately chosen inhomogeneous magnetic fields, often called magnetic trap. Magnetic traps are used to confine precooled gaseous system. We shall first discuss the method of precooling and then talk about the principle of magnetic trapping.

(ii) Method of precooling

Laser beams are often used to precool the atomic vapour and the method used goes by the name laser cooling. The physical mechanism by which the collision between photons and atoms reduces the temperature of the atomic vapour can be visualized as follows.

If an atom travels toward the laser beam and absorbs a photon from the laser it will be slowed down by the photon impact. Understandably, totality of such events will lower the temperature. On the other hand, if the atom moves away from the photon, the latter will speed up resulting in the increase of temperature. Thus, it is necessary to have more absorptions from head on photons if our goal is to slow down the atoms
with a view to lower the temperature. One simple way to accomplish this in practice is to tune the laser slightly below the resonance absorption of the atom.

Suppose that the laser beam is propagating in a definite direction. An atom in the gaseous system can move towards the beam or it may move away from the beam. In both cases the frequency of the photon will be Doppler shifted. In the first case the frequency of the laser beam will increase while in the other case the frequency will be decreased. In the case of head on collision the photon will be absorbed by the atom via resonance only when the original laser beam is kept below the frequency of atomic resonance absorption. When the atom and photon travel in the opposite direction there cannot be momentum transfer from the photon to the atom because Doppler shift in this case produces further detuning of the already detuned laser beam.

The explanation presented above provides only a simple-minded realization of laser cooling. The physics of any typical experiment is much more complicated than that because the absorption of photon by atom is also accompanied by an emission process. The emission and absorption produce a velocity dependent force that is responsible for cooling. A technique of laser cooling based on velocity-dependent absorption process goes by the name Doppler cooling. Doppler cooling can also be used in an arrangement called optical molasses where cooling is done in all three-dimensions. There is still another variant of laser cooling that goes by the name Sisyphus cooling. The mechanism of Sisyphus cooling is somewhat sophisticated. It involves a polarization gradient generated by two counter propagating linearly polarized laser beams with perpendicular polarization directions.

(iii) Basic principles of magnetic trapping

Magnetic traps are used to confine low temperature atoms produced by laser cooling. These traps use the same principle as that in the Stern-Gerlach experiment. Otto Stern and Walter Gerlach used the force produced by a strong inhomogeneous magnetic field to separate the spin states in a thermal atomic beam as it passes through the magnetic field. But for cold atoms the force produced by a system of magnetic coils bends the trajectories right around so that low energy atoms remain within a small region close to centre of the trap. This can be realized as follows.

A magnetic dipole moment $\vec{\mu}$ in a magnetic field $\vec{B}$ has energy

$$V = -\vec{\mu}.\vec{B}. \quad (77)$$

For an atom in a hyperfine state $|IJFM_F\rangle$, V corresponds to a Zeeman energy

$$V = g_F \mu_B M_F B, \quad (78)$$

where μ_B= Bohr magneton and

$$g_F \approx g_J \frac{F(F+1)+J(J+1)-S(S+1)}{2F(F+1)}. \quad (79)$$

The magnetic force acting along z - direction

$$P = -g_F \mu_B M_F \frac{dB}{dz}. \quad (80)$$

We shall now make use of Eqs. (77) and (78) to indicate (*i*) why precooling is necessary for the use of magnetic trap? and (*ii*) what should be the nature of the magnetic field that produces a trap useful for confining BEC? From Eq. (77) the energy depth of the magnetic trap is determined by $\mu_i B$. The atomic magnetic moment μ_i is of the order of Bohr magneton μ_B which in temperature units $\approx$ 0.67 Kelvin/Tesla. Since laboratory magnetic fields are generally considerably less than 1 Tesla, the depth of magnetic traps is much less than a Kelvin, and therefore atoms must be cooled in order to be trapped magnetically.

For confinement, Zeeman energy must have a minimum. We can consider two different cases for Eq. (78). Case 1: $M_F g_F > 0$. Here the Zeeman energy can be minimum if *B* has a local minimum. Case 2: $M_F g_F < 0$. In this case *V* can have a local minimum if *B* has a local maximum. Maxwell's equations do not allow a maximum of a static field. As a result, the trapping of atoms for $M_F g_F < 0$ is not allowed. In view of the above one can trap atoms only in a minimum of a static magnetic field.

(iv) More details for magnetic trapping of neutral atoms

We have noted the following.

Confinement of neutral atoms depends on the interaction between an inhomogeneous magnetic field and atomic multipole moment. (Dipoles may be trapped by the local field minimum. Field configurations with a minimum in $|\vec{B}|$ may be divided into two classes: (a) where the minimum of the field is zero, and (b) where it is non-zero. The original quadrupole trap as devised by Paul in NIST or the so-called Paul trap is shown in figure 5. It belongs to class (a). This trap consists of two identical coils carrying opposite currents and has a single center where the field is zero. It is the simplest of all possible magnetic traps. When the coils are separated by 1.25 times their radius, such a trap has equal depth in the radial (x-y*)* plane and longitudinal (z - axis) directions. Its experimental simplicity makes it most attractive, both because of construction and of optical access to the interior.

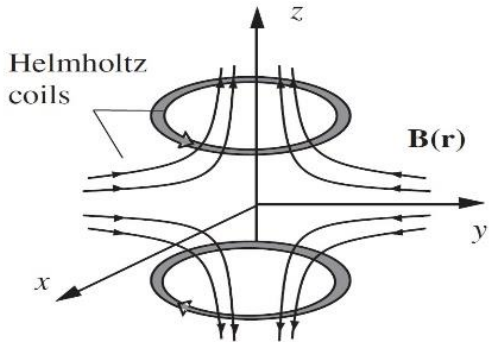

Fig. 5. Diagram of Paul trap.

The quadrupole trap suffers from an important disadvantage. The atoms assemble near the center where $B \approx 0$. As a result, Zeeman sublevels ($|IJFM_F\rangle$) have very small energy separation. The states with different magnetic quantum numbers mix together and atoms can make transition from one value of M_F to another due to fluctuation in the field. These nonadiabatic transitions allow the atoms to escape and reduce the lifetime of atoms in the trap. There have been two major efforts to circumvent the disadvantage of using the simple quadrupole trap. In the first case one superimposes an oscillating biased magnetic field on the quadrupole trap. Admittedly, this makes the magnetic field $\vec{B}$ time dependent. The time average of the resulting field remains nonvanishing at the center. An alternative approach, adapted by the MIT group of Ketterle, is to apply a laser field in the region of the node in the magnetic field.

Instead of using traps having a node in the magnetic field, one can remove the hole by working with magnetic field configurations that have a nonzero field at the minimum. The schematic diagram of such a magnetic field configuration is given in figure 6. Here four parallel wires arranged at the corner of a square produces a quadrupole magnetic field when currents in adjacent wires flow in the opposite directions. The resulting radiation forces repel atoms from the vicinity of the node, thereby reducing losses. This field has a linear dependence on the radial coordinate r and is given by

$$\left|\vec{B}\right| = b'r, \tag{81}$$

where $b' = \frac{\partial B_x}{\partial x} = -\frac{\partial B_y}{\partial y}$ obtained from $\vec{\nabla}.\vec{B} = 0$. Using Eqs. (78) and (79)

$$V(r) = g_F \mu_B M_F b' r. \tag{82}$$

Variation of the quantity $\left|\vec{B}\right|$ in Eq. (77) for the quadrupole trap is shown in figure 6(b).

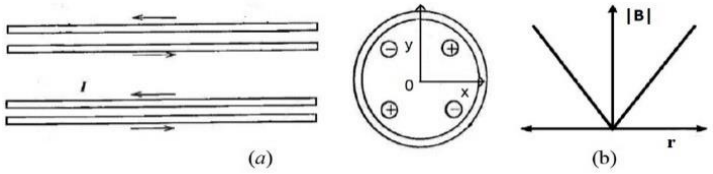

Fig. 6. (*a*) Linear quadrupole trap and (b) Magnetic field with radial coordinate *r*.

Clearly, $\left|\vec{B}\right| = 0$ at r = 0. In the so-called Iofee trap this problem is circumvented by using two circular coils which enclose the parallel wires as shown in figure 7(a). In both coils current flow in the same direction. The magnetic field for this configuration if given by

$$\left|\vec{B}\right| \approx B_0 + \frac{b'^2 r^2}{2B_0} \tag{83}$$

where B_0 is a magnetic field in the z direction produced by currents in the circular coils. For $\left|\vec{B}\right|$ in (83) a plot similar to that in figure 6(b) looks like the plot in figure 7(b). Clearly, this field has a nonzero value at $r = 0$.

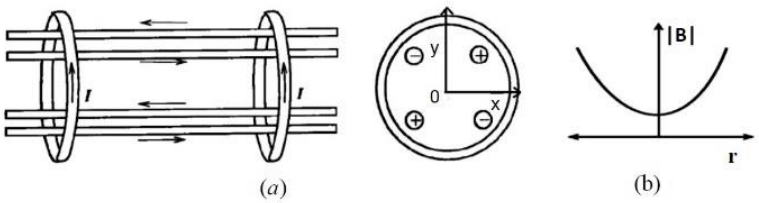

Fig. 7. (*a*) Iofee trap: combination of a linear magnetic quadrupole and an axial biased field. (b) Magnetic field that provides radial confinement of atoms *r*.

(v) Optical trapping

Magnetic traps provide an efficient method to confine cold atoms. The basic principle of optical trapping is as follows. The interaction between an atom and the electric field is given by

$$H' = -\vec{d}.\vec{\varepsilon}, \tag{84}$$

where $\vec{d}$, electric dipole moment and $\vec{\varepsilon}$, the electric field vector. Perturbation H'changes the ground-state energy by

$$\Delta E_g = -\frac{1}{2}\alpha\varepsilon^2, \tag{85}$$

where α = static atomic polarizability. Expression in Eq. (85) refers to an energy change produced by a static electric field.

The electric field in laser light is time-dependent. For a time-dependent electric field the expression in Eq. (85) modifies to

$$\Delta E_g = -\frac{1}{2}\alpha(\omega)\langle\varepsilon(\vec{r},t)^2\rangle, \tag{86}$$

where $\alpha(\omega)$ is the frequency-dependent polarizability.

An atom excited by the electric field is likely to decay by spontaneous emission. If this fact is taken into account, the frequency dependent polarizability becomes a complex quantity such that ΔE_g (86) could be written as

$$E_g = V_g - i\hbar\Gamma_g/2, \tag{87}$$

where the real part Vg corresponds to a shift in energy of the ground state while the imaginary part represents the finite lifetime $1/\Gamma_g$of the ground state due to the transition to the excited state induced by the radiation. In more detail,

$$\alpha(\omega) \approx \frac{|\langle e|\vec{d}.\hat{\varepsilon}|g\rangle|}{E_e - i\hbar\Gamma_e/2 - E_g - \hbar\omega}. \tag{88}$$

Here $1/\Gamma_e$= lifetime of the excited state. Using Eq. (88) in Eq. (86) and comparing the result with (50) we get

$$V_g = -\frac{1}{2}\alpha_R(\omega)\langle\varepsilon(\vec{r},t)^2\rangle_t \tag{89}$$

with the real part of $\alpha(\omega)$

$$\alpha_R(\omega) = \frac{(\omega_{eg}-\omega)|\langle e|\vec{d}.\hat{\varepsilon}|g\rangle|^2}{\hbar\left[(\omega_{eg}-\omega)^2+(\Gamma_e/2)^2\right]}, \tag{90}$$

where $\omega_{eg} = \left(E_e - E_g\right)/\hbar$. The force corresponding to the potential in Eq. (89) is given by

$$F_{dipole} = \frac{1}{2}\alpha_R(\omega)\vec{\nabla}\langle\varepsilon(\vec{r},t)^2\rangle_t. \tag{91}$$

From (90) we see that if $\omega > \omega_{eg}$, $\alpha_R(\omega)$ is negative and if $\omega < \omega_{eg}$, $\alpha_R(\omega)$ is positive. In the first case the laser beam is called blue detuned while in the second case we have red detuning. For red detuning the force acts along the higher field. On the other hand, for blue detuning the force acts along lower field. By focusing a laser beam it is possible to create a radiation field whose intensity has a maximum in space. If the frequency of the light is detuned to the red, the energy of the ground-state atom has a spatial minimum, and therefore it is possible to trap atoms.

(vi) Evaporative cooling

The temperature reached by laser cooling is quite low, but not low enough to produce Bose-Einstein condensation in gases at densities that are realizable experimentally. A very

effective technique of reducing the temperature of the magnetically trapped laser cooled atoms goes by the name evaporative cooling. In the experiment performed to date, Bose-Einstein condensation of alkali gases is achieved by using evaporative cooling. The basic physical effect in evaporative cooling is that, if particles escaping from a system have an energy higher than the average energy of particles in the system, the remaining particles are cooled. Evaporative cooling could be carried out by lowering the strength of the trap. But this reduces the density and eventually makes the trap too weak to support atoms against gravity. However, this method has been successfully used for *Rb* and *Cs* atoms in dipole-force traps. There is another important method for evaporative cooling. Here precisely controlled evaporation is carried out by using radio frequency radiation that changes the spin state of an atom from a low field seeking one to a high field seeking one, hereby expelling atoms from the trap.

(d) Observing the BEC in the laboratory

In a BEC the observable quantity is the density profile. There are two important methods to observe the density profile. The first one is called absorptive imaging while the second one goes by the name phase-contrast imaging.

(i) Absorptive imaging

Light at a resonant frequency for the atom will be absorbed on passing through an atomic cloud. Thus, measuring the absorption profile one can obtain information about the density distribution. The spatial resolution can be improved by allowing the cloud to expand before measuring the absorptive image. A drawback of this method is that it is destructive, since absorption of light changes the internal states of atoms and heats the cloud. An observation of Bose-Einstein condensation by absorption imaging is displayed in figure 8. It shows absorption vs. two spatial dimensions. The Bose-Einstein condensate is characterized by its slow expansion observed 6 ms after the atom trap was turned off. The left picture shows an expanding cloud cooled just above the critical temperature; middle: just after the condensate appeared; right: after further evaporative cooling has left an almost a pure condensate.

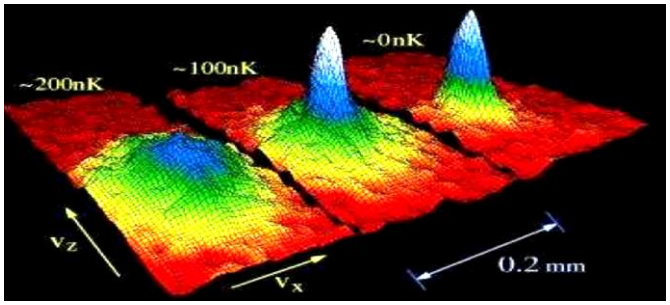

Fig. 8. Velocity distribution of ^{87}Rb condensates where red colour represents the region having lower number of atoms while white colour represents region of larger number of atoms [10].

(ii) Phase-contrast imaging:

This method exploits the fact that the refractive index of a gas depends on its density. Therefore, the optical path length is changed by the medium. Here a light beam is passed through the cloud. This is allowed to interfere with a reference beam that has been phase shifted. The change in optical path length as evident from the interference pattern is then converted into intensity variation for observation.

VI. Condensed atomic gases

(a) A new platform for studying condensed-matter physics

Dilute atomic gases in BECs are distinguished from the condensed-matter systems by the absence of strong and complex interaction. Despite that, studies in these quantum gases have become an interdisciplinary field of atomic and condensed matter physics. Topics of many-body physics can now be studied with the methods of atomic physics. In this way, BEC provides a new subfield that can confidently be used to simulate properties condense-matter systems [28].

The observation of the condensate's density distribution can be regarded as a direct visualization of the microscopic wave function. The time evolution of the squared wave function of a single condensate has been recorded non-destructively in real time [29, 30]. In a recent article Hannaford and Sacha [31] reviewed the case of a BEC of ultracold atoms bouncing resonantly on an oscillating atom mirror such that the period of the bouncing atoms is equal to an integer multiple of the period of the driving mirror. The bouncing BEC can exhibit dramatic breaking of time-translation symmetry, allowing the creation of discrete time crystals.

(b) Problem to inject spin-orbit coupling in BECs

The ultracold atoms which form the condensates are electrically neutral. Consequently, the intrinsic physics relevant to the charge degrees of freedom is absent in these systems. Ever since Bose-Einstein condensation (BEC) was achieved in atomic gases, one of the main tasks for both theory and experiment has been to introduce charge physics into neutral atoms creating gauge fields by artificial means. Experimentally, the first artificial magnetic field was synthesized in a harmonically trapped BEC through the rotation of the external trapping potential [32]. In the rotating frame, this leads to a Lorentz force and an antitrapping potential for atoms, where the amplitude and frequency of the anti-trap are proportional to the rotational frequency. However, this technique is limited because the strength of the anti-trap cannot exceed that of the trapping potential, which implies that it cannot be used for spatially homogeneous BECs. In this case, the magnetic field has to be generated artificially.

(c) Way to artificial gauge field

In the last few years there have been several attempts [33] to realize artificial gauge fields for quantum gases and thus overcome the problem arising due to neutrality of atoms to introduce spin-orbit interaction in an atomic cloud. One of these schemes relies on the notion of geometric phase [34] acquired by a quantum mechanical wave function while evolving in a parameter space of the Hamiltonian. The phase angle is defined in terms of an integral over a vector valued function often called the Berry connection. The Berry connection corresponds to an artificial vector potential for neutral atoms. To implement this idea the researchers from NIST and from University of Maryland exploited the space-dependent coupling of the atoms with a properly designed configuration of laser beams. The synthetic gauge field arises when the system adiabatically follows one of the local eigenstates of the light-atom interaction Hamiltonian [35]. Since 2009 several experiments have been successful in realizing ultra-cold atomic gases coupled to artificial gauge fields. For instance, a space dependent atom-light coupling was employed to generate an effective magnetic field to exert a Lorentz-like force on neutral bosons [36]. This procedure has also been used to generate quantized vortices in BECs.

(d) Spin-orbit coupled BECs

After engineering gauge fields in BEC the same group of workers attempted to simulate the coupling between an atom's spin and its motion with a view to realize the effect of spin-orbit coupling (SOC) in ultra-cold atomic systems. In atomic physics, SOC is an interaction between the electron's spin and its motion about the nucleus. For solids, SOC provides a link between the electron's spin and its motion in the crystal lattice. In both cases the SOC arises due to interaction of electrons with the electric fields that exist inside atoms and solids. But there is no charge field for atoms moving in a BEC. Consequently, Spielman and his group [37] sought a way to link the internal spin of an atom to its momentum. They had chosen to work with a BEC of ^{87}Rb atoms and focused their attention on the atom's electronic ground state, $5S_{1/2}$ $F=1$. In a typical experiment, a degenerate cloud of ^{87}Rb is prepared in a crossed optical dipole trap.

By applying a homogeneous magnetic bias field along the x -direction (as shown in figure 9), the $F=1$ ground state is split into three energy levels, m_f = 0, ±1. Two Raman lasers whose projections on the x-direction point oppositely are used to couple the energy levels $|F = 1, m_f = -1\rangle$ and $|F = 1, m_f = 0\rangle$, and $|F = 1, m_f = 0\rangle$ and $|F = 1, m_f = 1\rangle$. These energy levels can be interpreted as pseudo-spins. However, to simulate spin ½ systems, the third energy level have to be moved out of resonance. This can be done by applying a large magnetic field so that quadratic Zeeman effect shifts the energy splitting between $|F =1, m_f = -1\rangle$ and $|F = 1, m_f = 0\rangle$ to a larger value than that of the $|F = 1, m_f = 0\rangle$ and $|F = 1, m_f = 1\rangle$. Choosing an appropriate frequency between the Raman Lasers then allows one to address only the $|F = 1, m_f = -1\rangle$ and $|F = 1, m_f = 0\rangle$ transitions.

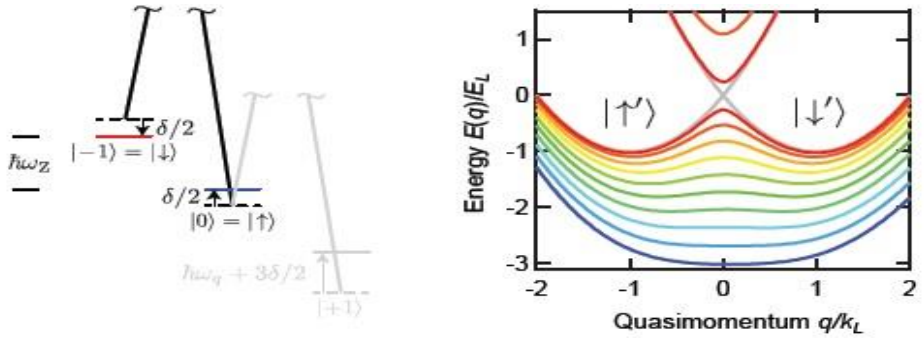

Fig. 9. Level diagram. Two Raman lasers couple the two states $|F = 1, m_f = -1\rangle$ and $|F = 1, m_f = 0\rangle$ of the F = 1 hyperfine manifold of ^{87}Rb, which differ in energy by a Zeeman splitting. The lasers have frequency difference $\Delta\omega_L = \omega_Z + \delta$, where δ is a small detuning from the Raman resonance. The state $|F = 1, m_f = +1\rangle$ can be neglected since it has a much larger detuning, due to the quadratic Zeeman shift.

This is how, by dressing two spin states with a pair of lasers, Spielman et al could engineer SOC with equal amount of Rashba [38] and Dresselhaus [39] coupling in a neutral atomic Bose-Einstein condensate. The synthetic spin-orbit coupling for neutral atoms was subsequently realized in other laboratories [40-43]. Thus, it became quite urgent to investigate theoretically how does the SOC affect the properties of usual BECs (without spin-orbit coupling) [44-46].

(e) Effect of spin-orbit coupling on the condensates

The behaviour of Bose-Einstein condensates is studied in the first-order of approximation by using Gross-Pitaevskii equation (GPE) [47,48] which is, in fact, the well-known Schrödinger equation plus a nonlinear term that takes into account of the interaction between atoms forming the condensates. The self-trapped localized states can be considered both in one-dimensional or higher-dimensional geometries. In multidimensional settings, stability of these states becomes a major issue due to critical and supercritical collapse [49, 50]. As opposed to this, in the one-dimensional case we have stable soliton states in diverse systems [51]. For a one-dimensional model of the BEC we assume that we have a dilute Bose gas and the radial trapping frequency of the condensate is much larger than the axial frequency, i. e. the BEC is cigar shaped. In this case the GPE is given by

$$i\hbar\frac{\partial\psi}{\partial t} = \left(-\frac{\hbar^2}{2m}\partial_x^2 + V_{tr}(x) - g|\psi|^2\right)\psi, \qquad (92)$$

where m stands for the mass of atoms in the condensate and $\psi$for the complex order parameter or wave function of the condensate. The quantities V_{tr} and g represent the trapping potential and coupling constant of the atom-atom interaction. It is well known that for attractive inter-atomic interaction $(g > 0)$, Eq. (92) supports soliton solution such that we have a highly stable condensate.

Equation (92) governs the dynamics of the BEC in the absence of spin-orbit coupling. A BEC with experimentally realized SOC is characterized by a spinor order parameter $\psi = (\psi_\uparrow, \psi_\downarrow)$ where $\psi_\uparrow$ and $\psi_\downarrow$ are related to the two pseudospin components of the BEC. The dimensionless equations of motion for $\psi_{\uparrow\downarrow}$ can be written as [52]

$$i\partial_t\psi_\uparrow = \left(-\frac{1}{2}\partial_x^2 - ik_L\partial_x + V_{tr}(x) - |\psi_\uparrow|^2 - \beta|\psi_\downarrow|^2\right)\psi_\uparrow + \Omega\psi_\downarrow, \qquad (93)$$

$$i\partial_t\psi_\downarrow = \left(-\frac{1}{2}\partial_x^2 + ik_L\partial_x + V_{tr}(x) - \beta|\psi_\uparrow|^2 - \gamma|\psi_\downarrow|^2\right)\psi_\downarrow + \Omega\psi_\uparrow\,. \qquad (94)$$

Here k_L is the wave number of the Raman laser which couples two atomic hyperfine states and Ω, the Raman or Rabi frequency. The quantities β and γ related to the *s*-wave scattering $\alpha_{ij}(i, j = 1, 2)$. In an interesting paper Xu, Zhang and Wu [53] made use of equations similar to those given above to study the properties of bright solitons ($\alpha_{ij} < 0$) and observed that the stationary bright solitons which are the ground states of the system have nodes in their wave function. For a conventional BEC without SOC its ground state must be nodeless. This is consistent with the so-called 'no node' theorem for the ground state of bosonic system [54]. In fact, the soliton in SOC-BEC is fundamentally different from the conventional one since the spin-orbit coupling breaks the Galilean invariance of the system. This lack of invariance was experimentally demonstrated [55] by studying the dynamics of SOC-BEC loaded in a translating optical lattice.

Optical lattices use standing wave patterns of counter-propagating laser beams to create a periodic potential for ultracold atoms. In most experiments [56-58] optical lattices act as external potentials and thus introduce a state- independent intrinsic periodicity in the system. We shall refer to these type lattices as linear optical lattice (LOL). Besides LOL, it is possible to consider a nonlinear optical lattice (NOL). The latter possess symmetry properties that depend on the wave function representing the state of the system [59].

The BECs loaded in optical lattices (OLs) are known to exhibit many interesting physical phenomena such as Bloch oscillation, Landau-Zener tunnelling, Mott Transition etc. [60]. In view of this, there has been a great deal of activities for studying dynamics of BEC solitons in OLs. It will be interesting to study the effect of optical lattices on the structure of the bright

soliton in the quasi-one-dimensional SOC-BEC. Recently, it has been found that parameters of the lattice potentials can be used to provide useful control over the number of nodes of the bright soliton and thereby make attempts to restore the Galilean invariance [61]. In this context we note that studies un restoration of Galilean invariance of physical systems are of relatively recent origin and have mainly been undertaken for nuclear force problem [62,63]. While looking for control over the number of nodes it has been seen that the soliton with large number of nodes is less stable compared to one having fewer number of nodes. This indicated that the synthetic spin-orbit coupling induces instability in the ordinary matter-wave soliton. In the following we shall study how the synthetic spin-orbit affect the atomic density distribution in the BEC.

As is well known that in atoms the spin-orbit coupling is the interaction between the electron's spin and its orbital motion around the nucleus. When an electron moves in the finite electric field of the nucleus, the spin–orbit coupling causes splitting in the electron's atomic energy levels thus leads to new spectroscopic phenomena. Spin-orbit coupling also lies at the core of condensed matter. In the presence of strong SOC, there can appear a wide variety exotic physical phenomenon in solid-state systems. For example, the coupling between an electron's spin and its momentum is crucial for topological insulators [64, 65] as well as for Majorana fermions [66]. In this context we also note that magnetic fields influencing the motion of electrons in a semiconductor are at the base of quantum Hall effect [67]. The spin electronics also called spintronics is an emerging field of basic and applied research in physics that aims to exploit the role played by electron spin in solid materials with a view to develop semiconductors that can manipulate the magnetic property of an electron [68].

Ultracold atomic gases are good candidates to investigate the above interesting quantum phenomena. In this respect, as already noted, the main difficulty arises from the fact that atoms are neutral particles, and consequently, like electrons, they cannot be coupled to gauge fields so as to exhibit any coupling between their spin and their center of mass motion. But the experimental realization of synthetic spin-orbit coupling [37] has removed this stumbling block and opened the door for simulating many observed phenomena in condensed-matter physics. In this respect a very important problem consists in studying the response of condensates' density profile to changes in the strength of the tuneable synthetic spin-orbit coupling. As regards the density profile of a quasi-one dimensional SOC-BEC we focus our attention on the solution of the coupled Eqs.(93) and (94). From these equations it is clear that the dynamics of SOC-BEC, in addition to the parameters of the trapping potential and strength of the inter-atomic interaction, depends crucially on the spin-orbit coupling parameter κ_L and the so-called Rabi frequency Ω. The parameter κ_L physically represents the wave number of the Raman laser that inject spin-orbit coupling in the condensate. Depending on the choice for the values of κ_K and Ω one can distinguish two different regions in the linear energy spectrum of the system. In region I, characterized by $\kappa_L^2 < \Omega$ has a single minimum and the associated GPE with attractive atom-atom interaction supports bright soliton solution [69] of the nonlinear Schrodinger equation. On the other hand, in region II with $\kappa_L^2 > \Omega$, the dispersion curve posses two minima say, $\pm k_0$, of the system. Two different solutions corresponding to these minima have also been given in ref. 52. In addition, we can have a linear superposition of these solutions that form a strip phase [40,70]. These wave functions can be used to obtain results for corresponding normalized to unity probability density distributions. Information theoretic measures of such probability densities have been found to provide a useful basis to examine the effect of any perturbation in the system [71,72]. In our case the synthetic SOC perturbs the density distribution of the conventional BEC. We now discuss below how such measures have recently been used [73] to study the perturbative effect of our interest.

Two popular information measures of a normalized to unity probability density $\rho(x)$ are given by the so-called Shannon entropy [74]

$$S_\rho = -\int_{-\infty}^{\infty} \rho(x)\, ln\, \rho\,(x) dx \tag{95}$$

and Fisher information [76]

$$I_\rho = \int_{-\infty}^{\infty} \rho(x) \left[\frac{d}{dx} ln\, \rho\,(x)\right]^2 dx. \tag{96}$$

In the momentum space, results corresponding to the one-dimensional quantities in Eqs. (95) and (96) are given by

$$S_\gamma = -\int_{-\infty}^{\infty} \gamma(p)\, ln\, \gamma\,(p) dp \tag{97}$$

and $I_\gamma = \int_{-\infty}^{\infty} \gamma(p) \left[\frac{d}{dp} ln\, \gamma\,(p)\right]^2 dp,$ (98)

The results of the above information theoretic quantities are subject to the constraints

$$S_\rho + S_\gamma \geq 2.14473 \tag{99}$$

and $I_\rho I_\gamma \geq 4.$ (100)

The relation in Eq. (99) represents a stronger version of the uncertainty relation introduced by Bialynicki-Birula and Mycielski [76] while that in Eq. (100) is due to Hall [77]. The Fisher based uncertainty relation has been re-derived by Dehesa et. al [78].

The information measures defined in Eqs. (97) and (98) provide complementary descriptions of disorder in the system. From mathematical point of view, one is a convex while the latter is concave [80]. When one grows the other diminishes. The larger values of the position-space Shannon entropy are associated with delocalization of the underlying densities while the smaller values imply localization Understandably, the opposite is true for the Fisher information. In view of this properties of S and I can be gainfully used to investigate how does the density distribution of a quantum many-body system respond to external perturbations.

Thus, numbers for both Shannon entropy and Fisher indicate that by increasing the strength of the spin-orbit coupling constant we go from a delocalized to localized atomic distribution in the condensate. The corresponding momentum -space quantities $S_\gamma(I_\gamma)$ increase(decrease) as κ_L become large. The results for position - and momentum - space information measures never violate uncertainty relations in Eqs. (99) and (100). In region II ($\kappa_L^2 > \Omega$), $S_\rho, S_\gamma,$ I_ρ and I_γ as a function of κ_L exhibit opposite behavior as observed for these quantities in region I. This establishes that for $\kappa_L^2 > \Omega$ the atomic distribution in the condensate becomes delocalized as we increase the strength of the SOC. This is just opposite to what we observed for the condensate in spectral region I. For the BEC in the stripe phase the results for S and I exhibit similar behavior as that of the condensate in region II i. e. BEC becomes more localized as we increase the strength of the SOC. At the lowest admissible value of κ_L under the constraint $\kappa_L^2 > \Omega$ the result for I_ρ has been found to be rather inconsistent. This implies that the strip phase cannot exist in BECs unless the synthetic spin-orbit coupling is strong enough. In general, the numbers for I_ρ are greater than the corresponding values of I_ρ in spectral region II by an order of magnitude. Very high values of I_ρ tend to establish that in the stripe phase the density distribution is highly localized. This is quite expected since this phase characterizes the supersolid properties of the SOC BEC. From the results for I_ρ and I_γ it is seen that values of the uncertainty $I_\rho I_\gamma$ are very large for all admissible values of κ_L. It is, therefore, tempting to infer that supersolidity is a purely quantum mechanical Phenomenon.

VII. Concluding remarks

The present work is a modest attempt to pay homage to the great Indian scientist Satyendra Nath Bose. His pioneering work came from India when the center of intense scientific activity was Europe. We began by noting that Bose's intellectual development was unusual and he was destined to play an inspiring role in the scientific and cultural life of our country. He was well versed in Bengali, English, French, German and Sanskrit. Bose always had wanted science to be taught in mother language and he tried his best to achieve the goal. In recognition of Bose's effort to popularize science through the mother language, poet Rabindra Nath Tagore invited Bose to Santiniketan and dedicated the book 'Visva-Parichaya' to him [80]. This book gives an elementary account of cosmic and microcosmic world in Bengali. We noted in the text that, in honor of S. N. Bose, the British physicist P. A. M. Dirac, the originator of the relativistic electron theory, coined the term 'boson' for particles which obey Bose statistics.

Next, we focused our attention on the statistics introduced by Bose and its application to derive Planck's law of radiation, which opened a new window into the quantum world and made him immortal in the history of science. In fact, Bose read Planck's paper on the distribution of energy in blackbody radiation to teach this material in his class. He was disturbed by the ad hoc assumptions of Planck as were used to derive the law. In 1924, Saha stayed with Bose in Dacca (now called Dhaka) and pointed out the papers of Wolfgang Pauli, Paul Ehrenfest and their relation to Einstein's 1917 paper. This led him to develop the so-called Bose statistics - a new method to count the states of indistinguishable particles - and apply it to his derivation of Planck's law. After the publication of Bose's work by the recommendation of Albert Einstein, Einstein himself extended the work of Bose to material particles. This led to the birth of Bose-Einstein statistics and theoretical prediction of a macroscopic quantum phenomenon - Bose-Einstein condensation (BEC). Since then, there were many attempts to observe BEC in the laboratory. Now we know that BECs are produced by cooling a dilute atomic gas to nano kelvin temperature using laser and evaporative cooling. We have tried to briefly outline the series of events that ultimately led to the experimental realization of BECs.

There has been a growing interest in the physics of cold atoms. For example, the NIST group generated Abelian gauge fields to introduce a synthetic spin - orbit interaction in the electrically neutral cold atoms of the Bose-Einstein condensates. Such interactions have been found to drastically affect properties of the conventional condensates without spin-orbit coupling. We have provided here two examples in respect of this. In the first one we studied the interplay between the spin-degrees of freedom and nonlinear atomic interaction by loading a one-dimensional SOC BEC in an optical lattice. In the second one we made use of two information theoretic measures to critically examine the effect of spin-orbit coupling on the density profiles of a quasi-one-dimensional condensate with attractive inter - atomic interaction. Interestingly enough, it was found that the BEC in the stripe phase exhibits supersolid properties and supersolidity is a purely quantum mechanical phenomenon.

Acknowledgments. One of the authors (GAS) would like to acknowledge funding from the 'Science and Engineering Research Board, Govt. of India' through Grant No.CRG/2019/000737.

References

[1] Narlikar, J. V., Lectures on general relativity and cosmology, (Mcmillan Press, London, 1979).

[2] Mehra, J. and Rechenberg, H., The Historical Development of Quantum Theory, (Springer-Verlag New York, Inc. 1982).
[3] A. Pais, Subtle is the Lord: The science and the life of Albert Einstein, (Oxford University Press, USA,1998).
[4] Blanpied, W. A., Satyendranath Bose: Co-Founder of Quantum Statistics, Am. J. Phys., 1972, vol. **40**, p. 1212-1220.
[5] Hau, L. V., Busch, B. D., Liu, C., Burns, M. M. and Golovchenko, J. A., Cold Atoms and Creation of New States of Matter: Bose-Einstein Condensates, Kapitza States, and '2D Magnetic Hydrogen Atoms', arXiv:cond-mat/9804277v1; 24 Apr. (1998).
[6] Chatterjee, S. and Chatterjee, E., Satyendra Nath Bose, (National Book Trust, India, 1976).
[7] Wali, K. C., Satyendra Nath Bose: His life and times, (World Scientific, Singapore, 2009).
[8] Anderson, M. H. J., Ensher, J. R., Metthews, M. R., Wieman, C. E., and Cornel, C. A., Observation of Bose-Einstein condensation in a dilute atomic vapour, Science, 1995, vol. **269**, p. 198-201.
[9] Bradley, C. C., Sackett, C. A., Tollett, J. J., and Hulet, R. G., Evidence of Bose-Einstein condensation in an atomic gas with attractive interaction, Phys. Rev. Lett., 1995, vol. **75**, p. 1687.
[10] Davis, K. B., Mewes, M. O., Andrews, M. R., van Druten, N. J., Durfee, D. S., Kurn, D. M. and Ketterle, W., Bose-Einstein condensation in a gas of sodium atoms, Phys. Rev. Lett., 1995, vol. **75**, p. 3969.
[11] Bose, S. N., Plancks Gesetz und Lichtquantenhypothese, Zeitschrift für Physik, 1924, vol. **26**, p. 178-181.
[12] Tyndall, J., On the Absorption and Radiation of Heat by Gases and Vapours, and on the Physical Connexion of Radiation, Absorption, and Conduction, Phil. Mag. and Journal of Science, 1861, vol. **22**, p. 169.
[13] Kirchhoff, G., On the relation between the radiating and absorbing powers of different bodies for light and heat, The London, Edinburgh, and Dublin Phil. Mag. and Journal of Science, 1860, vol. **20**, p. 1.
[14] Heilbron, J. L., A History of Atomic Models from the Discovery of the Electron to the Beginnings of Quantum Mechanics, diss. (University of California, Berkeley, 1964)
[15] Pathria, R. K., and Beale, P. D., Statistical Mechanics (3rd Ed., Elsevier, New York, 2021).
[16] Paschen, F., Uber gesetzmassigkeiten in den spectren fester korper, Annalen der Physik, 1896, vol. **294**, p. 455-492.
[17] Carson, T. R., Steps to the Planck function: A Centenary Reflection, arXiv: astro-ph/0011219v1 10 Nov 2000.
[18] Rayleigh, L., The dynamical theory of gases and radiation, Nature, 1905, vol. **72**, p. 54-55.
[19] Jeans, J. H., The dynamical theory of gases and radiation, Nature, 1905, vol. **72**, p. 101-102.
[20] Planck, M., On the law of the energy distribution in the normal spectrum, Ann. Phys., 1901, vol. **4**, p. 553 -563.
[21] Pais, A., Einstein and the quantum theory, Rev. Mod. Phys., 1979, vol. **51**, p. 863.
[22] Schiff, L. I., Quantum Mechanics, (Tata McGraw-Hill Edition, New Delhi, India, 2010).
[23] Saha, M. N. and Srivastava, B. N., A treatise on heat, (4th Ed., The Indian Press (Publication) Private Ltd., 1958).
[24] Einstein, A., Quantentheorie des einatomigen idealen Gases, Sitzungsberichte, 1924, p. 261-267.
[25] Sokol, P. E., Bose-Einstein condensation in Liquid Helium, edited by A. Griffin, D. W. Snoke and S. Stringari (Cambridge University press, Cambridge 1995) p. 51

[26] Silvera, I. F., Spin-Polarized Hydrogen: Prospects for Bose–Einstein Condensation and Two-Dimensional Superfluidity, edited by A. Griffin, D. W. Snoke and S. Stringari (Cambridge University press, Cambridge 1995) p. 160.
[27] Cohen-Tannoudji, C. N., Manipulating atoms with photons, Rev. Mod. Phys., 1998, vol. **70**, p. 707.
[28] Pethick, C. J., and Smith, H., Bose-Einstein Condensation in Dilute Gases (Cambridge University Press, Cambridge, 2004).
[29] Andrews, M. R., Mewes, M. -O., van Druten, N. J., Durfee, D. S., Kurn, D. R. and Ketterle, W., Direct, Nondestructive observation of a Bose-Condensate, Science, 1996, vol. **273**, p. 84 - 87.
[30] Andrews, M. R., Kurn, D. M., Miesner, H.-J., Durfee, D. S., Townsend, C. G., Inouye, S. and Ketterle, W., Propagation of sound in a Bose-Einstein Condensate. Phys. Rev. Lett. 1997, vol. **79**, p. 553.
[31] Hannaford, P. and Sacha, K., Condensed Matter Physics in Big Discrete Time Crystals, arXiv:2202.05544v1 [cond-mat.quant-gas] 11 Feb 2022.
[32] Fetter, A. L., Rotating trapped Bose-Einstein condensates, Rev. Mod. Phys., 2009, vol. **81**, p. 647.
[33] Dalibard, J., Gerbier, F., Juzeliūnas, G. and Öhberg, P. Artificial gauge potentials for neutral atoms, Rev. Mod. Phys. 2011, vol. **83**, p. 1523.
[34] Bohm, A., Quantum Mechanics and Applications (3rd Edition, Springer-Verlag, 1993)
[35] Lin, Y.-J., Compton, R. L., Jiménez-García, K., Porto, J. V., and Spielman, I. B., Synthetic magnetic fields for ultracold neutral atoms, Nature, 2009, vol. **462**, p. 628-632.
[36] Lin, Y.-J. Compton, R. L., Jiménez-García, K., Phillips, W. D., Porto, J. V., and Spielman, I. B., A synthetic electric force acting on neutral atoms, Nature Physics, 2011, vol. **7**, p. 531-34.
[37] Y. -J. Lin, K. Jiménez-García and I. B. Spielman, Spin–orbit-coupled Bose–Einstein condensates, Nature, 2011, vol. **471**, p. 83-86.
[38] Bychkov, Yu. A. and Rashba, E. I., Oscillatory effects and the magnetic susceptibility of carriers in inversion layers, J. Phys. C: Solid State Phys., 1984, vol. **17,** p. 6039-6045.
[39] Dresselhaus, G., Spin-Orbit Coupling Effects in Zinc Blende Structures, Phys. Rev., 1955, vol. **100**, p. 580.
[40] M. Aidelsburger, M. Atala, S. Trotzky, Y. A. Chen and Bloch, I., Experimental realization of strong effective magnetic fields in an optical lattice, Phys. Rev. Lett., 2011, vol. **107**, p. 255301.
[41] Wang, P., Yu, Z. Q., Miao, Z. F., Huang, L., Chai, S., Zhai, H. and Zhang, J., Spin-orbit coupled degenerate Fermi gases, Phys. Rev. Lett., 2012, vol. **109**, p. 095301.
[42] Cheuk, L. W., Sommer, A. T., Hadzibabik, Z., Yefsah, T., Bakr, W. S. and Zwierlein, M. W., Spin-injection spectroscopy of a spin-orbit coupled Fermi gas, Phys. Rev. Lett., 2012, vol. **109**, p. 095302.
[43] Zhang, L. -Y., Ji, S. –C., Chen, Z., Zheng, J., Du, Z. -D., Yan, B., Pan, G. -S., Zhao, B., Deng, Y. -J., Zhai, H., Chen, S. and Pan, J. -W., Collective Dipole Oscillations of a spin-orbit coupled Bose-Einstein condensate, Phys. Rev. Lett. 2012, vol. **109**, p. 115301.
[44] Sinha, S., Nath, R. and Santos, L., Trapped two-dimensional condensates with synthetic spin-orbit coupling, Phys. Rev. Lett. 2011, vol. **107**, p. 270401.
[45] Ramachandhran, B., Opanchuk, B., Liu, X. –J. , Pu, H., Drummond, P. D., and Hu, H., Half-quantum vortex state in a spin-orbit-coupled Bose-Einstein condensate, Phys. Rev. A, 2012, vol. **85**, p. 023606.

[46] Li, Y., Martone, G. I. and Stringari, S., Sum rules, dipole oscillation and spin polarizability of a spin-orbit coupled quantum gas, Eur. Phys. Lett., 2012, vol. **99**, p. 56008.
[47] E. P. Gross, Hydrodynamics of a superfluid condensate, J. Math. Phys., 1963, no. 2, vol. **4**, p. 195-207.
[48] Pitaevskii, L. P., Vortex lines in an imperfect Bose gas, Sov. Phys. JETP, 196, vol. **13**, p. 451.
[49] Berge, L., Wave collapse in physics: Principles and applications to light and plasma waves. Phys. Rep.,1998, vol. **303**, p. 259.
[50] Vuong, L. T., Grow, T. D., Ishaaya, A. Gaeta, A. L, 't Hooft, G. W., Eliel, E. R., and Fibich, G., Collapse and l Vortices, Phys. Rev. Lett., 2006, vol. **96**, p. 133901.
[51] Y. V. Kartashov, L. Torner, M. Modugno, E. Ya Sherman, B. A. Malomed and V. V. Konotop, Multidimensional hybrid Bose-Einstein condensates stabilized by lower-dimensional spin-orbit coupling, Phys. Rev. Res., 2020, vol. **2**, p. 013036.
[52] Achilleos, V. Frantzeskakis, D. J., Kevrekidis, P. G. and Palinovsky, D. E., Matter-Wave Bright Soliton in Spin-Orbit Coupled Bose-Einstein Condensates, Phys. Rev. Lett. 2013, vol. **110**, p. 264101.
[53] Xu, Y., Zhang, Y., and Wu, B., Bright solitons in spin-orbit coupled Bose-Einstein condensate, Phys. Rev. A, 2013, vol. **87**, p. 013614.
[54] R. P. Feynman, Statistical Mechanics, A Set of Lectures (Addison-Wesley Publishing Company, 1972).
[55] C. Hammer, Y. Zhang, M. A. Khamehchi, M. J. Davis and P. Engels, Spin-orbit coupled Bose- Einstein condensates in a one-dimensional optical lattice, Phys. Rev. Lett., 2015, vol. **114**, p. 070401.
[56] Eiermann, B., Anker, T., Albiez, M., Tagieber, M., Treulein, P., Marzlin K. P., and Oberthalar, M. K., Bright Bose-Einstein gap solitons of atoms with repulsive interaction, Phys. Rev. Lett., 2004, vol. **92**, p. 230401.
[57] Anderson, B. P., and Kasevich, M. A., Macroscopic quantum interference from atomic tunnel arrays, Science, 1998, vol. **282**, p. 1686.
[58] Greiner, M., Mandal, O., Esslinger, T., Hansch, T. W., and Bloch, I., Quantum phase transition from a superfluid to a Mott insulator in a gas of ultracold atoms, Nature (London), 2002, vol. **415,** p. 39.
[59] Abdullaev, F. Kh., and Garnier, J., Propagation of matter-wave solitons in periodic and random nonlinear potentials, Phys. Rev. A, 2005, vol. **72**, p. 061605 (R).
[60] Morsch, O., and Oberthaler, M., Dynamics of Bose-Einstein condensates in optical lattices, Rev. Mod. Phys., 2006, vol. **78**, p. 176.
[61] Sekh, G. A. and Talukdar, B., Effects of optical lattices on bright solitons in spin-orbit coupled Bose-Einstein condensates, Phys. Lett. A, 2021, vol. **415**, p. 127665.
[62] N. Li, S. Elhatisari, E. Epelbaum, D. Lee, B. Lu and Ulf-G. Meiβner, Galilean invariance restoration on the lattice, Phys. Rev. C, 2019, vol. **99**, p. 064001.
[63] P. Massella, F. Barranco, D. Lonardoni, A. Lovato, F. Pederiva and E. Vegezzi. Exact restoration of Galilei invariance in density functional calculations with quantum Monte Carlo, J. Phys. G. Nucl. Part. Phys., 2020, vol. **47**, p. 035105.
[64] Hassan, M. Z., and Kane, C. L., Colloquium: Topological insulators, Rev. Mod. Phys., 2010, vol. **82**, p. 3045.
[65] Qi, X. -L. and Zhang, S. -C. Topological insulators and superconductors, Rev. Mod. Phys., 2011, vol. **83**, p.1057.
[66] Wilczek, F., Majorana returns, Nat. Phys., 2009, vol. **5**, p. 614.

[67] von Klitzing, K., The quantized Hall effect, Rev. Mod. Phys., 1986, vol. **58**, p. 519.
[68] Flatte, E. M., IEEE Transaction on Electronic Devices, 2007, vol. **54**, no. 5, p. 907-920.
[69] Golam Ali Sekh, Dynamics of Matter-wave Solitons in Bose-Einstein Condendate, Ph. D Thesis (unpublished) Visva-Bharati University, Santiniketan, India (2010).
[70] Tin-Lun, Ho. and Zhang, S., Bose-Einstein condensation with spin-orbit interaction, Phys. Rev. Lett., 2011, vol. **107**, p. 150403.
[71] Romera, E. and Dehesa, J. S., The Fisher-Shannon information plane, an electron correlation tool, J. Chem. Phys., 2004, no. 9, vol. **120**, p. 8906-8912.
[72] Sekh, G.A., Saha, A. and Talukdar, B., Shannon entropies and Fisher information of K-shell electrons of neutral atoms, Phys. Lett. A, 2018, vol, **382**, p. 315-320.
[73] Sekh, G.A., Talukdar, B., Chatterjee, S. and Khan, B. A., Physica Scripta, 2022, vol. **97**, p. 115404.
[74] Shannon, C. E., A Mathematical Theory of Communication, Bell Syst. Tech. J, 1948, vol. **27,** p. 379.
[75] Fisher, R. A., Theory of Statistical Estimation, Proc. Cam. Phil. Soc., 1925, vol. **22,** p. 700.
[76] Bialynicki-Birula, I. and Myceilski, J., Uncertainty relations for information entropy in wave mechanics, Commun. Math. Phys**.,** 1975, vol. **44**, p. 129.
[77] Hall, M. J. W., Quantum properties of classical Fisher information, Phys. Rev. A, 2000, vol. **62**, p. 012107.
[78] Dehesa, J. S., Gonzalez-Feres, R. and Sanchzes-Moreno, P., The Fisher information-based relation, Cramer-Rao inequality and kinetic energy for the D-dimensional central problem, J. Phys. A: Math. Theor., 2007, vol. **40**, p. 1845.
[79] Vadrel, V., Introduction to Quantum Information Science, (Oxford University Press, Oxford, 2006).
[80] Rabindranath Tagore (1861-1941), Indian poet; Nobel Prize in Literature, 1913, for *Gitanjali,* a collection of his lyric poems originally in Bengali, translated into English by Tagore himself and into French by Andre Gide.

LUMINESCENT PROPERTIES OF LOW-DIMENSIONAL ZnO:Ag POWDERS OBTAINED BY CHEMICAL DEPOSITION FROM AQUEOUS SOLUTION

T. Goglidze[1], E. Goncearenco[2], I. Dementiev[1], N. Nedeoglo[1,*], T. Iurieva[1], D. Nedeoglo[1]

[1] Physics of Semiconductors and Devices Laboratory, Department of Physics and Engineering, Moldova State University, A. Mateevici str. 60, MD-2009 Chișinău, Moldova
[2] National Institute for Lasers, Plasma and Radiation Physics, Atomistilor str. 409, RO-077125 Bucharest-Magurele, Romania
**E-mail: natalia.nedeoglo@usm.md*

(Received, 15 November, 2023)

https://doi.org/10.53081/mjps.2023.22-1.02

Abstract

Photoluminescence (PL) spectra of ZnO:Ag highly dispersed powders obtained by chemical deposition from aqueous solution are investigated in the wavelength range between 360 and 750 nm at room temperature under excitation between 250 and 350 nm. Before starting the synthesis, the Ag dopant was introduced into the initial solution in the form of $AgNO_3$ silver nitrate in the amount of 12, 102, and 252 mg. The PL spectra consist of an ultraviolet emission (380 nm) attributed to Ag_{Zn} acceptor-bound exciton, a short-wavelength violet emission (400 – 450 nm) and a wide long-wavelength yellow-orange emission (560 – 600 nm). With decreasing excitation energy, the violet emission decreases in intensity, while the yellow-orange emission increases. This is caused by the phenomenon of self-absorption of the short-wavelength emission and energy transmission to the centers of the long-wavelength emission. A rapid decrease in intensity of all the PL bands is found for the sample with maximum Ag concentration. This fact is due to the appearance of the second phase in the form of silver oxide and, consequently, a decrease in the concentration of Ag_{Zn} point defects responsible for the bands.

Keywords: ZnO, highly dispersed powders, photoluminescence, self-absorption, Ag impurity.

Rezumat

În intervalul de lungimi de undă între 360 și 750 nm, la temperatura camerei, prin excitare cu o radiație din regiunea (250 – 350) nm, sunt investigate spectrele de fotoluminescență (FL) a nanopulberilor de ZnO:Ag obținute prin metoda de depunere chimică din soluția acvatică. Impuritatea de Ag a fost introdusă în soluția inițială sub formă de azotat de argint $AgNO_3$ în cantitate de 12, 102 și 252 mg. Spectrele de PL conțin benzile de emisie ultravioletă (380 nm), atribuită excitonului legat de acceptor de Ag_{Zn}, emisie violetă (400 – 450 nm) și emisie galbenă-oranjă (560 – 600 nm). Odată cu scăderea energiei de excitare, intensitatea emisiei violete descrește, în timp ce intensitatea emisiei galbene-oranje crește. Acest fapt este cauzat de

fenomenul de autoabsorbție a emisiei din regiunea undelor scurte și transmitere de energie către centrele de emisie din regiunea undelor lungi. O descreștere rapidă a intensității tuturor benzilor de PL se observă pentru proba cu concentrația maximă de Ag. Acest fapt este stiplulat de apariția celei de-a două faze sub formă de oxid de argint și, ca rezultat, de scăderea concentrației defectelor punctiforme de Ag_{Zn} responsabile de aceste benzi.

Cuvinte cheie: ZnO, nanopulberi, fotoluminescența, autoabsorbție, impuritate de Ag.

1. Introduction

Wide band-gap ZnO semiconductor (E_g(300K) = 3.37 eV) is of great interest both for investigation of radiative properties and applications in optoelectronics and solar energy [1]. Being optically transparent in a wide wavelength range, zinc oxide is used for high-performance light-emitting devices operating in the ultraviolet (UV) and blue regions of the spectrum, UV filters, solar cells, thin-film transistors, sensor devices, etc. [1-3].

It is well known that PL spectra of ZnO samples consist of near-band-edge emission at (370 – 390 nm), violet emission at (396 – 410 nm), and three wide bands of visible emission: "green" (500 – 530 nm), "yellow-orange" (590 – 620 nm) and "red" (700 – 780 nm) [4]. The predominance of one or another PL bands essentially depends on the impurity-defect composition of the samples.

PL study of ZnO thin films obtained by magnetron sputtering and doped with the group I acceptor impurities (Cu, Ag, and Au) has showed the predominance of the "green" emission attributed to donor-acceptor (DA) pairs with intrinsic oxygen vacancies as the donors and introduced doping impurities as the acceptors [5]. At the same time, after oxygen enrichment during the growth and impurity doping of ZnO:Cu and ZnO:Ag films by electron-beam deposition, PL spectra consist of near-band-edge and exciton emission lines in the violet spectral region [6]. Introduction of dopants into zinc oxide nanocrystals allows modifying the functional properties of ZnO, thereby expanding their applications [7–9].

In the present paper, the evolution of PL spectra of low-dimensional ZnO:Ag powders with increasing dopant concentration and excitation wavelength is analyzed.

2. Experimental techniques

Highly dispersed zinc oxide powders were synthesized by chemical deposition from aqueous solution. The solutions of 0.05M zinc nitrate hexahydrate and urotropine (hexamethylenetetramine, HMTA) in a molar ratio of 1:1 were used as the main components of the synthesis. ZnO is formed in the solution that contains zinc nitrate as a Zn^{2+} precursor and urotropine due to the following chemical reactions between $Zn(NO_3)_2$ and HMTA [10]:

$$(CH_2)_6N_4 + 6\ H_2O \leftrightarrow 6\ HCHO + 4\ NH_3 \quad (1)$$

$$NH_3 + H_2O \leftrightarrow NH_4 + OH^- \quad (2)$$

$$2\ OH^- + Zn^{2+} \rightarrow ZnO + H_2O \quad (3)$$

Hydroxide ions appearing during the decomposition of HMTA react with Zn^{2+} and form zinc oxide.

The doping impurity of Ag was introduced into the solution before the synthesis in the

form of a salt of nitric acid ($AgNO_3$) in the amount of 12, 102, and 252 mg. Chemical deposition of zinc oxide was carried out with continuous stirring using a magnetic stirrer in a two-stage heating mode. At the first stage, the temperature of the reaction mixture reached (48 – 50) °C, the duration was 1 hour. At the second stage, the temperature was increased to (78 – 80) °C, and, under these conditions, the synthesis continued for 2 hours. After completing the synthesis, a sediment of zinc oxide settled at the bottom of reaction cell was cooled, washed many times in a distilled water, and dried. The obtained powders were gray in color and the color intensity increased with increasing Ag concentration in the powder.

PL spectra and PL excitation spectra of ZnO:Ag powders were measured at room temperature between 360 and 750 nm under excitation with UV radiation between 250 and 350 nm. The spectra were registered using a standard synchronous detection system with Fluorolog-3 (HORIBA) fluorospectrometer. A xenon lamp of 500 W was used as an excitation source. A two-monochromator system was used for the lamp radiation decomposition into individual wavelengths and registration of emission spectra of the samples. PL spectra were recorded in an automatic mode at every 10 nm of the excitation radiation wavelength.

3. Experimental results and discussion

Fig. 1 shows the evolution of PL spectra with excitation radiation wavelength for ZnO:Ag samples with various concentrations of Ag. The spectra consist of two bands in the short-wavelength (400 – 450 nm) and long-wavelength (560 – 600 nm) regions.

The short-wavelength violet emission in the range between 390 nm (3.179 eV) and 420 nm (2.952 eV) was previously observed at room temperature in the spectra for ZnO thin layers grown under an excess of oxygen, regardless of the growth method [11-17]. The nature of emission centers and mechanism of violet emission were analyzed in detail in [4]. The violet PL band in the spectra for ZnO crystals and thin films was attributed to the recombination of non-equilibrium charge carriers within DA pairs. The defects, such as the group III elements as substitutional defects (Al_{Zn}, Ga_{Zn}, In_{Zn}) and Li_i, Zn_i interstitial atoms, may be the donors. Zinc vacancies (V_{Zn}) or ($Al_{Zn}V_{Zn,}$), ($Ga_{Zn}V_{Zn}$), ($In_{Zn}V_{Zn}$) associates may be the acceptors [12]. In our ZnO:Ag nanopowders, the Ag_{Zn} point substitutional defects may be the acceptors. It was previously established [6] that the monovalent silver atoms were incorporated into ZnO in the form of Ag_{Zn} substitutional defects with $3d^{10}$ electron configuration.

The long-wavelength yellow-orange emission is due to Li and Na background impurities, which take part in the formation of DA pairs [18]. Transitions of electrons to these centers from the conduction band or shallow donors localized close to these centers are responsible for the PL bands at 575 nm (2.157 eV) (Na-DA pairs) and 615 nm (2.016 eV) (Li-DA pairs) [18, 19]. However, in later works [20-23], the yellow-orange emission in PL spectra of low-dimensional ZnO was attributed to interstitial oxygen atoms or oxygen-based complexes. The authors note that this PL band is more often observed for zinc oxide grown from an aqueous solution at relatively low temperatures and, therefore, enriched with oxygen, which corresponds to our case.

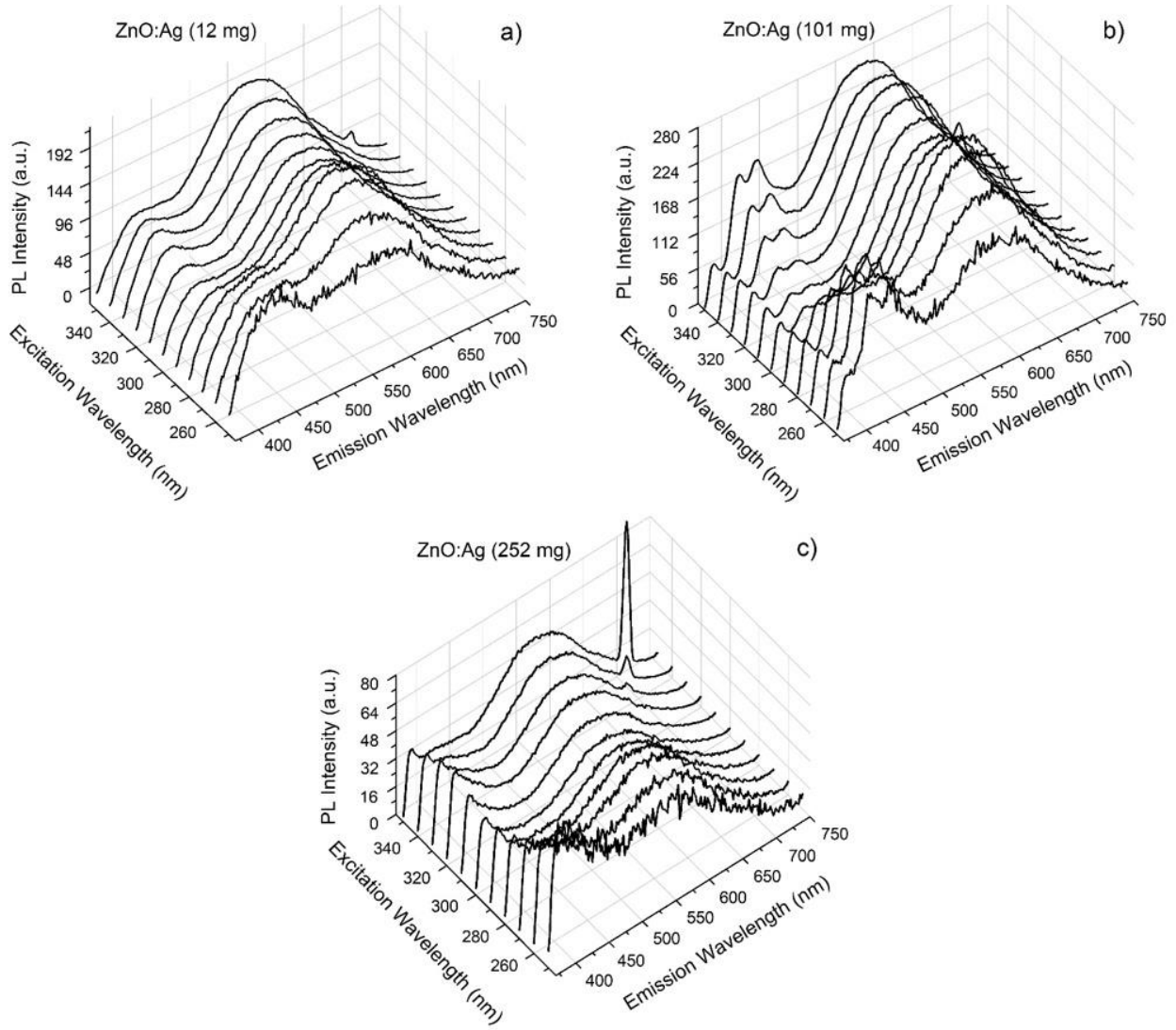

Fig. 1. PL spectra of ZnO:Ag powders with Ag content in aqueous solution of 12 mg (a), 102 mg (b), 252 mg (c). λ_{exc} = (250 – 350) nm. T = 300 K.

It is worth to note that the intensity ratio at the maximum of the long-wavelength emission to that of the short-wavelength one depends on the excitation radiation energy (Fig. 2). At high excitation radiation energy, the short-wavelength emission is predominant in intensity (Fig. 2 a), while at lower excitation radiation energy, the long-wavelength emission becomes predominant (Fig. 2 b). This modification is due to a self-absorption effect that was observed in thin ZnO films [12]. With decreasing excitation radiation energy, generation of quanta of the short-wavelength emission occurs at higher depth of the sample. As a result, the energy of this emission is partially absorbed in the material, and the centers of the long-wavelength emission are excited.

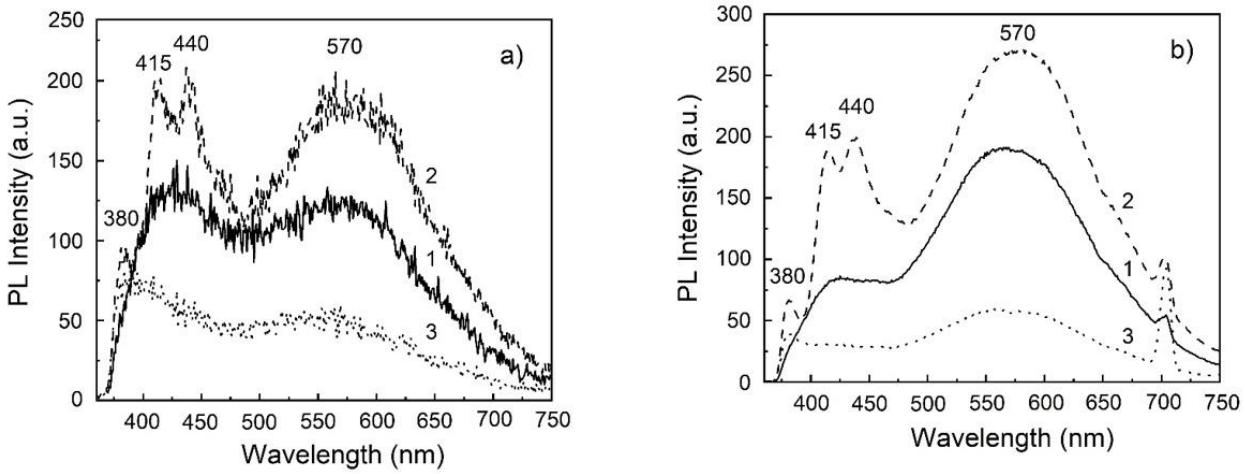

Fig. 2. PL spectra of ZnO:Ag powders under excitation radiation wavelength of 250 nm (a) and 350 nm (b). Ag content in aqueous solution, mg: 1 – 12; 2 – 102; 3 – 252. T = 300 K.

In addition to these PL bands, the short-wavelength band of exciton emission is observed at 380 nm (3.263 eV) in the PL spectrum of ZnO:Ag sample with medium doping level (102 mg Ag) (Fig. 2, curve 2). Increasing doping concentration decreases this PL band intensity (Fig. 2, curve 3). For the sample with minimum doping impurity concentration (12 mg Ag), this PL band is absent both at low and high excitation radiation energy (Fig. 2, curve 1). The spectral position of the exciton PL band is in good agreement with localization of (A^0X) acceptor-bound exciton (ABE) PL band at 381 nm (3.255 eV) at room temperature that was observed earlier for ZnO nanocrystals [24]. According to the empirical Haynes rule [25], the ionization energy of Ag_{Zn} acceptor, which is responsible for this ABE, is equal to:

$$\Delta E_A\left(Ag_{Zn}\right) = 10 \cdot \left(3.293 - 3.263\right) \text{ eV} = 0.300 \text{ eV}, \quad (4)$$

where 3.293 eV is the energy of free exciton emission in ZnO at 300 K [24], 3.263 eV is the energy of ABE emission at 300 K (Fig. 2). The value of 0.20 eV as the ionization energy of Ag_{Zn} acceptor is reported in [6] for ZnO:Ag thin films.

The structure of PL spectra of ZnO:Ag powders is slightly changed, mainly in the short-wavelength range, with increasing doping impurity concentration (Fig. 2). As Ag concentration increases, intensity of all the PL bands first increases and then decreases. A similar behavior for ZnO:Ag thin films was explained by the appearance of the second phase in the form of silver oxide at high concentration of Ag impurity [6]. A higher value of ionic radius for Ag (0.113 nm) relative to that for Zn^{2+} (0.083 nm) [26] induces a lattice strain during the doping process, and this strain is compensated by the second phase appearance. As a result, the concentration of Ag_{Zn} point defects decreases, and the PL intensity decreases too (Fig. 2).

Fig. 3 shows PL excitation spectra for the short-wavelength violet emission (380 nm) (Fig. 3 a) and long-wavelength yellow-orange emission (570 nm) (Fig. 3 b) for ZnO:Ag samples with various concentrations of doping impurity. Spectral position of the maxima of PL and PL excitation spectra is shown in Table 1.

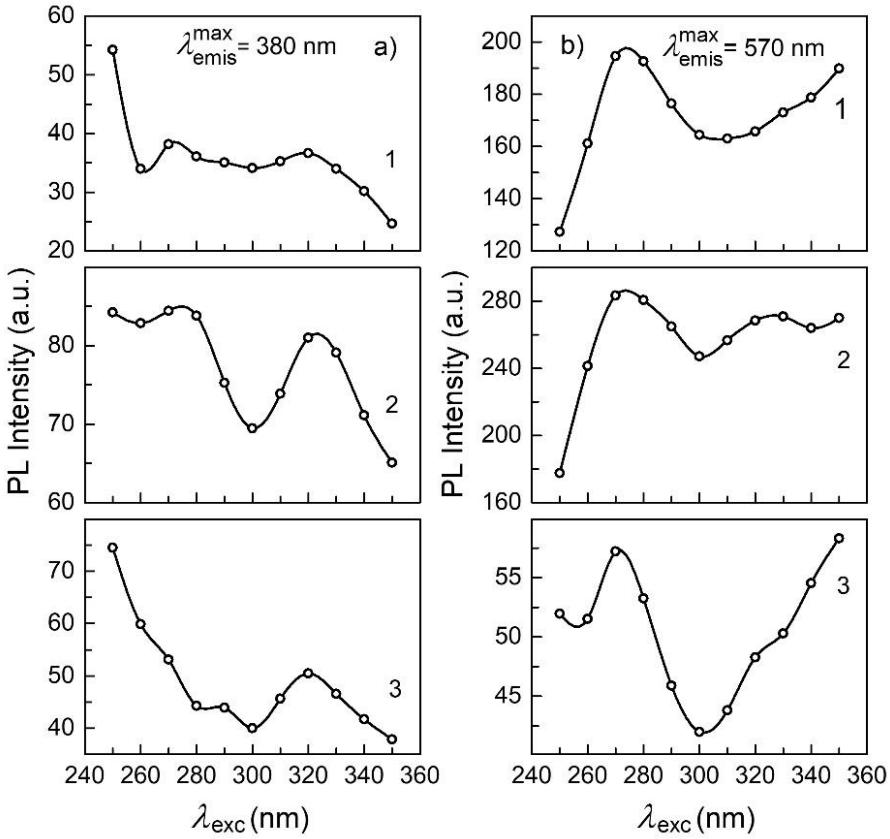

Fig. 3. PL excitation spectra for the short-wavelength violet emission (a) and long-wavelength yellow-orange emission (b). Ag content in aqueous solution, mg: 1 – 12; 2 – 102; 3 – 252. T = 300 K. Lines are guide to the eye.

Table 1

Maxima for PL and PL excitation spectra of ZnO:Ag nanopowders

	Ag content in aqueous solution, mg		
	12	102	252
λ_{emis}^{max}, nm	λ_{exc}^{max}, nm		
380	272 320	275 323	290 320
415	270 330	260	323
440	270 337	260	320 340
570	274 330	274 328	272 320

With increasing excitation radiation wavelength above 320 nm, the exciton PL band (380 nm) decreases in intensity (Fig. 3 a), while the impurity PL band (570 nm) increases (Fig. 3 b). For the short-wavelength emission, a maximum of low intensity is observed at 290 nm for the sample with maximum Ag content (252 mg) (Fig. 3 a, curve 3). This maximum is probably stipulated by the appearance of the second phase in the form of silver oxide, as it was mentioned above. For the long-wavelength emission, this maximum is not observed (Fig. 3 b, curve 3), since Ag impurity, apparently, is not a part of the luminescence center responsible for this emission (570 nm). A lack of pronounced maximum at (270-275) nm in the excitation spectrum of exciton emission (Fig. 3 a, curve 3) is also the evidence of structural modifications caused by the appearance of the second phase in ZnO:Ag powders with maximum Ag concentration.

5. Conclusions

The synthesis of ZnO low-dimensional powders by chemical deposition from aqueous solution accompanied by Ag impurity doping is realized in this work. A series of ZnO:Ag powders with various concentrations of doping impurity is obtained. It is found that monovalent silver atoms introducing into ZnO as Ag_{Zn} substitutional defects of acceptor type with the ionization energy of ~ 300 meV form emission centers, and namely, acceptor-bound excitons and donor-acceptor pairs, which are responsible for the ultraviolet (380 nm) and violet (415-440 nm) emissions respectively.

All the observed PL bands are decreased in intensity for the sample with maximum Ag concentration (252 mg in initial aqueous solution). This fact is due to the appearance of the second phase in the form of silver oxide and, as a result, a decrease in the concentration of Ag_{Zn} point defects responsible for the bands. It is shown that, with increasing excitation radiation wavelength, the violet emission decreases in intensity, while the yellow-orange emission (570 nm) increases. This behavior is caused by the phenomenon of self-absorption of the short-wavelength emission and energy transmission to the centers of the long-wavelength emission.

Acknowledgements

This work was supported by the National Agency for Research and Development (Republic of Moldova) [research grant 20.80009.5007.12].

References

[1] Ü. Özgür, Ya.I. Alivov, C. Liu, A. Teke, M.A. Reshchikov, S. Doğan, V. Avrutin, S.-J. Cho, H. Morcoç, J. Appl. Phys. 98, 041301 (2005).
[2] Z.L. Wang, Materials Today, 7, 26 (2004).
[3] D. Lincot, Thin Solid Films, 487, 40 (2005).
[4] I.P. Kuz'mina, V.A. Nikitenko, Preparation and optical properties of zinc oxide [in Russian], Moscow, 1984.
[5] A.N. Gruzintsev, V.T. Volkov, I.I. Khodos, T.V. Nikiforova, M.N. Koval'chuk, Russian Microelectronics, 200, 31 (2002).
[6] A.N. Gruzintsev, V.T. Volkov, E.E. Yakimov, Semiconductors, 37, 259 (2003).

[7] V.V. Malyshev, A.V. Pislyakov, Sensors and Actuators B: Chemical, 123, 71 (2007).
[8] S.C. Pillai, J.M. Kelly, D.E. McCormack, R. Ramesh, Material Chemistry, 14, 1572 (2004).
[9] S.Y. Davydov, V.A. Moshnikov, A.A. Fedotov, Technical Physics Letters, 30, 727 (2004).
[10] L. Schmidt-Mende, J.L. MacManus-Driscoll, Materials Today, 10, 40 (2007).
[11] S.S. Kurbanov, Sh.Z. Urolov, Z.Sh. Shaymardanov, H.D. Cho, T.W. Kang, Semiconductors, 52, 757 (2018).
[12] T.I. Goglidze, I.V. Dementiev, A.V. Coval, E.P. Goncearenco, N.D. Nedeoglo, D.D. Nedeoglo, J. Luminescence, 197, 396 (2018).
[13] A.A. Chaaya, R. Viter, M. Bechelany, Z. Alute, D. Erts, A. Zalesskaya, K. Kovalevskis, V. Rouessac, V. Smyntyna, P. Miele, Beilstein J. Nanotechnol. 4, 690 (2013).
[14] R.B. Kale, Y.-J. Hsu, Y.F. Lin, S.Y. Lu, Sol. St. Commun. 142, 302 (2007).
[15] G. Hua, Y. Zhang, Ch. Ye, M. Wang, L. Zhahg, Nanotechnology, 18, 145605 (2007).
[16] X.M. Fan, J.S. Lian, L. Zhao, Y.H. Liu, Appl. Surface Sci. 252, 420 (2005).
[17] S.H. Jeong, B.S. Kim, B.T. Lee, Appl. Phys. Lett. 82, 2625 (2003).
[18] E. Mollwo, D. Zwingel, J. Luminescence 12/13, 441 (1976).
[19] B.C. Cavenett, Advances in Physics 30, 475 (1981)
[20] X.L. Wu, G.G. Siu, C.L. Fu, H.C. Ong, Appl. Phys. Lett. 78, 2285 (2001).
[21] X. Liu, X. Wu, H. Cao, R.P.H. Chang, J. Appl. Phys. 95, 3141 (2004).
[22] A.B. Djurišić, Y.H. Leung, K.H. Tam, L. Ding, W. K. Ge, H.Y. Chen, S. Gwo, Appl. Phys. Lett. 88, 103107 (2006).
[23] J.W.P. Hsu, D.R. Tallant, R.L. Simpson, N.A. Missert, R.G. Copeland, Appl. Phys. Lett. 88, 252103 (2006).
[24] J.-P. Biethan, V.P. Sirkeli, L. Considine, D.D. Nedeoglo, D. Pavlidis, H.L. Hartnagel, Materials Science and Engineering B, 177, 594 (2012).
[25] R.E. Halsted, M. Aven, Phys. Rev. Lett. 14, 64 (1965).
[26] M. Aven, J.S. Prener, Physics and Chemistry of II-VI Compounds. Nort-Holland, Amsterdam, 1967.

THE INFLUENCE OF TEMPERATURE AND PRESSURE TECHNOLOGICAL PARAMETERS ON THE CHARACTERISTICS OF ZnO NANOSTRUCTURES SYNTHESIZED BY SOL-GEL PROCESS IN ISOPROPANOL

Fatah Mouzaia[1], Djamel Djouadi[1*], Azeddine Chelouche[1], Tahar Touam[2]

[1]Laboratoire de Génie de l'Environnement (LGE), Université de Bejaia, Route de Targa ou Zemmour, Bejaia, (06000), Algeria,
[2]Laboratoire des Semi-conducteurs, Université Badji Mokhtar-Annaba, BP12, 23000 Annaba, Algeria
**E-mail: djamel.djouadi@univ-bejaia.dz*

(Received, 16 November, 2023)

https://doi.org/10.53081/mjps.2023.22-1.03

Abstract

The sol-gel process was employed to successfully synthesize ZnO nanostructures in isopropanol, employing various subcritical temperature and pressure conditions: (90°C, 2 bar), (120°C, 6 bar), (160°C, 14 bar), and (200°C, 30 bar). The resulting products were subsequently annealed at 500°C for 2 hours and subjected to characterization using different analytical techniques, including X-ray diffraction (DRX), infrared (ATR), UV-Visible, and photoluminescence (PL) spectroscopies. The DRX measurements confirmed that the ZnO nanostructures exhibited a polycrystalline structure of the hexagonal wurtzite type. The cell parameters and stresses within the crystallites were found to be influenced by the synthesis conditions (temperature and pressure), in contrast to the particle size. ATR spectra indicated high purity of the produced nanostructures, and it was observed that the position of the absorption band associated with the Zn-O vibrational bond of ZnO shifted towards lower wavenumbers as the temperature increased. UV-Visible spectra demonstrated that the absorption band shifted towards shorter wavelengths with increasing temperature and pressure. The optical gap displayed a similar trend to the lattice parameters and strain within the nanoparticles. PL measurements revealed that the processing temperature and pressure resulted in increased UV emission and decreased visible emission. However, the positions of the UV emission bands were independent of the synthesis parameters.

Keywords: ZnO, temperature, pressure, isopropanol, wurtzite structure, photoluminescence.

1. Introduction

Currently, the scientific community's focus is directed towards zinc oxide due to its remarkable characteristics, which include a wide band gap of 3.37 eV and a strong excitation bond of 60 meV at room temperature. These properties have garnered significant attention and interest from researchers in various fields [1,2]. Due to its abundance, non-toxicity, and stability,

this material holds great appeal across multiple domains, including electronics, optoelectronics, and photocatalysis. Its plentiful availability, lack of harmful effects, and durability make it an extremely desirable material in these fields [3]. The intended applications of zinc oxide differ depending on its form of usage. When utilized in thin film form, it serves as a crucial component for producing a diverse range of devices. These devices include transparent semiconductor electrodes, piezoelectric transducers, optical waveguides, and gas detectors. Each of these applications leverages the unique properties of zinc oxide in thin film configuration to enable their functionality [4,5]. When zinc oxide is harnessed in the form of nanowires, it holds promising potential for various applications such as solar cells, UV lasers, light-emitting diodes, piezoelectric nanogenerators, and photoelectrocatalysts [6,7]. On the other hand, nanostructures of zinc oxide offer distinct advantages, allowing it to be employed as a photocatalyst, pigment, sunscreen, and more. The utilization of zinc oxide in these different forms enables a wide array of functionalities and applications across several fields [1,8-11].

Fabricating ZnO nanostructures can be accomplished through diverse methodologies, including precipitation [12], hydrothermal synthesis [13], vapor deposition [14], electrodeposition [15], wet impregnation [16], and sol-gel techniques [17]. These different approaches provide researchers with a range of options to create ZnO nanostructures tailored to their specific needs, enabling the exploration of various properties and applications of these nanostructures [10,11,18]. The properties of nanostructures are intricately associated with the specific fabrication method employed and the experimental parameters involved, including temperature and pressure. These factors significantly influence the structural, morphological, and functional attributes of the resulting nanostructures. Consequently, meticulous control of these parameters is crucial in tailoring the characteristics of ZnO nanostructures to meet specific requirements for a wide range of applications [19].

Therefore, the objective of this work is to fabricate ZnO nanostructures at varying temperatures and pressures of isopropanol, and investigate their structural and optical properties. Additionally, the study aims to examine and discuss the influence of these parameters on the characteristics of the obtained nanomaterials. Through this analysis, a comprehensive understanding of the relationship between temperature, pressure, and the resulting properties of ZnO nanostructures can be obtained.

2. Experimental procedures

For the synthesis of pure ZnO, we employed zinc acetate dihydrate as the precursor, methanol as the primary solvent, and isopropanol as the co-solvent. The sample preparation procedure entailed dissolving 8 g of zinc acetate in 56 ml of methanol while maintaining constant magnetic stirring at room temperature. This stirring process continued for approximately 10 minutes until the solution achieved a uniform and whitish appearance, indicating homogeneity. Subsequently, the prepared solution is transferred into a 1L autoclave, and the heating process commences with the addition of 300 ml of isopropanol. The heating continues until the desired temperatures and pressures are achieved within the autoclave. Once these conditions have been reached, the solvents are evacuated from the autoclave in vapor form. The resulting product is then left undisturbed to naturally cool down to room temperature over a duration of 24 hours. Following this cooling period, the samples undergo thermal annealing at 500°C for 2 hours. Finally, the resulting samples are subjected to analysis to evaluate their properties and characteristics.

In order to study the sample, several analytical methods were employed. The crystal structure analysis was conducted using a Rigaku diffractometer (MiniFlex) with X-rays generated by a copper cathode, where the wavelength of CuKα radiation was 1.54 Å. Infrared spectra were recorded utilizing an Agilent Technologies Cary 630 FTIR spectrophotometer, employing the ATR (Attenuated Total Reflectance) method. The UV-Visible properties were examined using a Thermo-Scientific Evolution 201 spectrophotometer. Additionally, photoluminescence spectra were acquired at room temperature using a LabSolutions RF 6000 spectrophotometer, with an excitation wavelength of 350 nm. These analytical techniques were employed to gain insights into various aspects of the sample's properties and characteristics. Uniform processing conditions were maintained for all samples throughout the experiment. The specific processing temperature was predetermined and played a crucial role in determining the corresponding final pressure value. The processing conditions, denoted by temperature (T) and pressure (P), are summarized in Table 1, providing a clear overview of the experimental parameters employed for each sample.

Table 1. Elaboration conditions (T, P)

	T (°C)	P(Bars)
Sample 1 (S1)	90	2
Sample 2 (S2)	120	6
Sample 3 (S3)	160	14
Sample 4 (S4)	200	30

An electric furnace, regulated by a temperature programmer with two heating speeds, is employed to heat the autoclave. Additionally, a manometer is used to measure the pressure within the autoclave. The time-dependent changes in temperature (T) and pressure (P) within the autoclave, as well as the relationship between pressure and temperature (P = f(T)), are graphically depicted in Figure 1. This figure provides a visual representation of the dynamic variations in temperature and pressure throughout the experimental process.

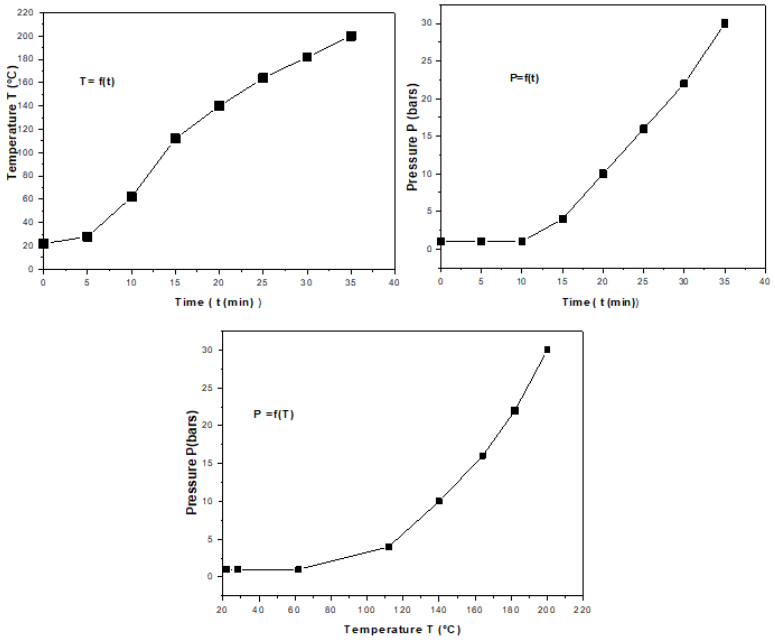

Fig. 1. Pressure and Temperature parameters variations in the autoclave (T= f(t), P=f(t) and P=f(T)) during the elaboration of the sample S4.

3. Results and discussions

Figure 2 displays the X-ray diffraction (XRD) spectra of the four samples, each processed at distinct temperatures. Within the range of 25° to 75°, the observed diffraction peaks align precisely with the characteristic peaks of ZnO, exhibiting a hexagonal wurtzite crystal structure (JCPDS 36-1451). These diffraction peaks display a high intensity, sharpness, and fine resolution, indicating excellent crystallinity of the nanostructures and confirming their polycrystalline nature. The XRD analysis provides concrete evidence of the well-defined crystal structure and favorable crystalline quality of the synthesized ZnO nanostructures.

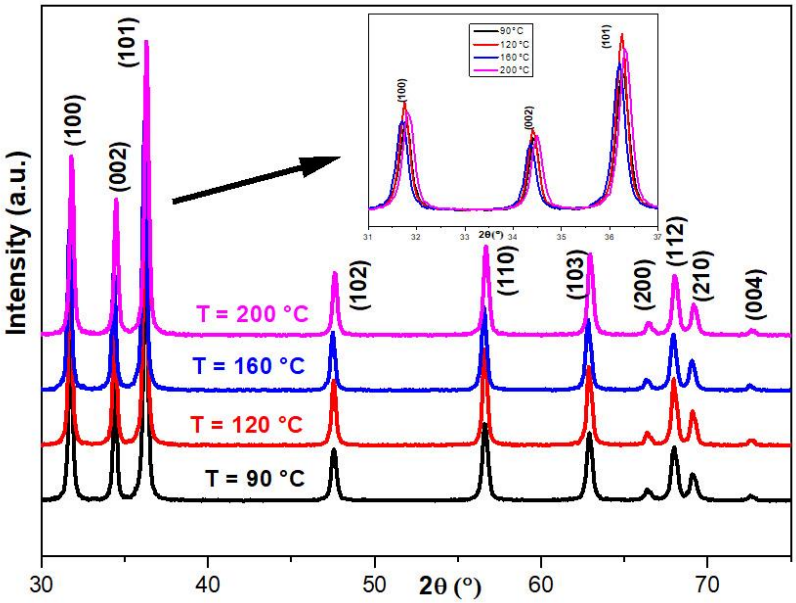

Fig. 2. X-ray diffractograms of ZnO samples produced under parametric conditions (90°C, 2bar), (120°C, 6bar), (160°C, 14bar) and (200°C, 30bar). Insert: diffractograms of the most prominent peaks.

Following the annealing process at 500°C for a duration of 2 hours, the XRD spectra display a remarkable similarity among all the peaks, with minimal fluctuations in intensity and position. This observation indicates that the chemical reactions, which were incomplete at the synthesis temperatures of 90°C, 120°C, 160°C, and 200°C, have been successfully finalized through the formation of ZnO from zinc hydroxide ($Zn(OH)_2$). The nearly identical peaks suggest that the annealing process facilitated the completion of these reactions, resulting in the transformation of zinc hydroxide into ZnO [20-22]:

Before the annealing process: $Zn^{2+} + 2OH^- \rightarrow Zn(OH)_2$

After the annealing process: $Zn(OH)_2 \rightarrow ZnO + H_2O$

The observed variations in peak intensity indicate fluctuations in the number of atoms refracting in each direction. Similarly, the variations in peak position suggest changes in structural parameters such as lattice parameters and lattice volume. These variations can arise from different types of stresses, including compressive or tensile stresses, exerted on the material. These stress-induced changes in the structural parameters contribute to the observed variations in peak position, providing insights into the mechanical behavior and properties of the synthesized nanostructures [23,24].

Conversely, the presence of prominent peaks corresponding to the (100), (002), and (101) crystallographic orientations indicates that a significant portion of the ZnO crystallites exhibit growth along these three specific directions. However, the absence of a preferential orientation suggests the polycrystalline nature of these nanostructures. This indicates that the synthesized ZnO nanostructures consist of multiple crystalline domains with varying orientations, rather than a single crystal with a dominant growth direction [25]. The purity of our elaborated samples is evident from the absence of any additional peaks originating from other crystalline phases. The absence of extraneous peaks confirms that the synthesized samples predominantly consist of ZnO and do not contain impurities or the presence of other crystalline phases.

The insert of Figure 2 illustrates the X-ray diffractograms of the most prominent peaks in the ZnO nanostructures. Notably, the positions of these peaks remain nearly constant and exhibit minimal variation across different processing conditions. The crystallite size (D), calculated using the Scherrer formula, as well as the lattice parameters ($a = b = \lambda/\sqrt{3}sin\theta_{100}$) and ($c = \lambda/sin\theta_{002}$), derived from the peak positions (101) and (002), are conveniently summarized in Table 2. The average crystallite size (D_a) is determined by calculating and averaging the values obtained from the three peaks (100), (002), and (101). Additionally, the stress values within the ZnO crystallites are computed based on the XRD results, specifically the largest peak (101), employing the formula ($\varepsilon = \beta/4tg\theta$) [26]. These stress values are also presented in Table 2.

Table 2. Structural parameters of ZnO nanostructures produced under different conditions.

Sample (T, P)	$\boldsymbol{a = b}$ $(\boldsymbol{nm})$	$\boldsymbol{c}$ $(\boldsymbol{nm})$	$\boldsymbol{c/a}$	$\boldsymbol{V}$ $(\boldsymbol{nm^3})$	$\boldsymbol{D_m}$ $(\boldsymbol{nm})$	$\boldsymbol{\varepsilon}$ (%)	$\boldsymbol{Eg}$ $(\boldsymbol{eV})$
S1 (90°C, 2 bars)	0.3248	0.5204	1.602	0.0475	32.8	3.75	3.07
S2 (120°C, 4 bars)	0.3250	0.5207	1.602	0.0476	36.0	3.54	3.02
S3 (160°C, 14 bars)	0.3255	0.5215	1.601	0.0478	33.0	3.24	2.96
S4 (200°C, 30 bars)	0.3242	0.5194	1.602	0.0472	32.1	3.62	3.00

Table 2 illustrates the relationship between cell parameters, temperature, and pressure in the autoclave. It indicates that the cell parameters initially increase as the temperature and pressure in the autoclave rise, reaching a peak at 160°C and 14 bars. However, for the sample processed at 200°C and 30 bars (S4), the cell parameters decrease. Conversely, the stress exerted on the crystallites demonstrates an inverse trend, decreasing with decreasing cell parameters and increasing with increasing cell parameters. This suggests that the slight variations in structural parameters are primarily attributed to residual stresses experienced by the crystallites during the elaboration process. Furthermore, it is noteworthy that the average crystallite size of our samples is not significantly affected by the processing conditions.

Figure 3 presents the ATR spectra of the four samples. Notably, in the frequency range of 650 to 400 cm^{-1}, the spectra appear flat, indicative of the high purity of the processed samples. This suggests the absence of chemical elements associated with potential impurities that could be present in the synthesized products. Moreover, it confirms that the chemical reactions involving the synthesis products used in the elaboration process have been successfully completed, leaving

no residual compounds. In the wavenumber range below 500 cm^{-1}, a prominent absorption band is observed, corresponding to the vibration of the Zn-O bond in ZnO. This distinctive absorption feature further confirms the presence of ZnO in the synthesized samples [27,28]. Within the frequency range of 430-550 cm^{-1}, the absorption band associated with the Zn-O bond undergoes a shift towards smaller wavenumber values as the temperature and pressure increase. This shift is clearly depicted in the insert of Figure 3. The ATR analyses consistently verify that the ZnO nanostructures have been fabricated with a high degree of purity. Furthermore, these analyses demonstrate that the characteristics of the ZnO nanostructures remain largely unaffected by the specific synthesis conditions.

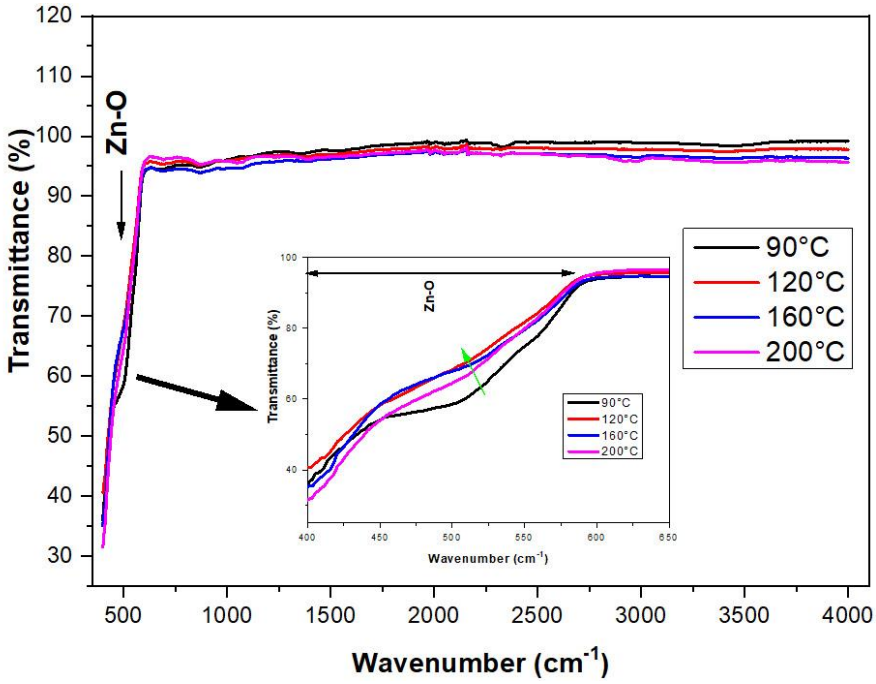

Fig. 3. ATR spectra of ZnO nanostructures elaborated under parametric conditions (90°C, 2bar), (120°C, 6bar), (160°C, 14bar) and (200°C, 30bar). Insert shows ATR spectra in the 430-550 cm^{-1} region.

Figure 4 exhibits the UV-Visible optical absorption spectra of ZnO nanostructures under different isopropanol temperatures and pressures, specifically (90°C, 2 bar), (120°C, 6 bar), (160°C, 14 bar), and (200°C, 30 bar). Each spectrum displays a prominent absorption band centered around 365 nm (corresponding to an energy level of 3.39 eV). This absorption band is attributed to the fundamental absorption process, resulting from the band-to-band transition between the valence and conduction bands of ZnO. As the processing temperature increases, the intensity of this absorption band strengthens, and it slightly shifts towards shorter wavelengths. This shift suggests an enhancement in the crystalline quality of the ZnO nanostructures, indicating an increased number of ZnO crystallites capable of absorbing light.

The nanostructures exhibit minimal absorption in the visible region, which further diminishes as the temperature and pressure in the autoclave during synthesis increase. Moreover, it is noteworthy that the slope of the absorption spectra demonstrates an upward trend in the absorption region as the synthesis temperature rises.

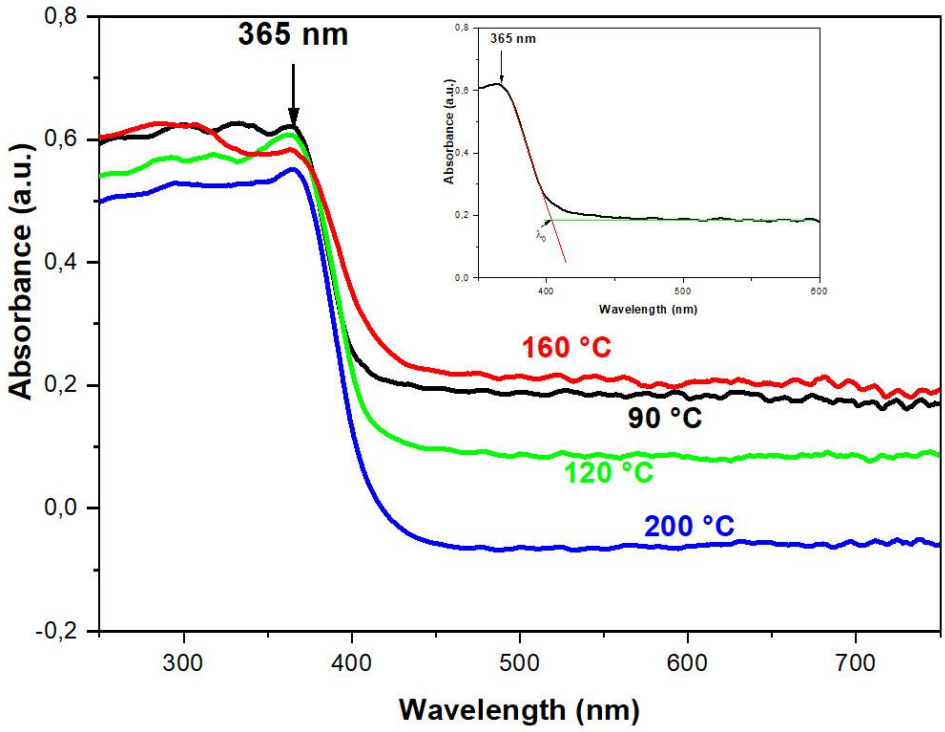

Fig. 4. UV-Visible spectra of ZnO nanostructures developed under parametric conditions (90°C, 2bars), (120°C,6 bars), (160°C, 14 bars) and (200°C, 30 bars). In the insert, the method for graphically determining the value of λ_0.

The following relationship can be used to determine the optical gap E_g [29]:

$$E_g\,(eV) = 1240/\lambda_0\,(nm)$$

where λ_0 is the wavelength at which ZnO crystallites begin to absorb photons.

To determine the value of λ_0, we employ a method that involves identifying the point of intersection between a horizontal line representing absorption in the visible range and the linear portion (slope) of absorption in the UV range. This approach, as depicted in the insert of Figure 4, enables us to estimate the wavelength at which ZnO nanoparticles begin to absorb photons, representing the energy at which electrons transition from the valence band to the conduction band. The estimated values of λ_0 for ZnO nanostructures grown under different conditions, namely (90°C, 2 bar), (120°C, 6 bar), (160°C, 14 bar), and (200°C, 30 bar), are 404 nm, 410 nm, 419 nm, and 413 nm, respectively. The optical gap values of the engineered nanostructures are computed and presented in Table 3. The data reveal that the optical gap diminishes with an increase in the synthesis temperature. For instance, the sample synthesized at 90°C with a pressure of 2 bars exhibits an optical gap of 3.07 eV, while the sample produced at 160°C with a pressure of 16 bar has an optical gap of 2.96 eV. However, at the higher temperature (200°C, 30 bar), the optical gap starts to increase.

Notably, the behavior of the optical gap exhibits similarities to that of strain and cell parameters. Specifically, as the lattice parameter values decrease, there is a corresponding decrease in both the stress within the crystallites and the optical gap. Conversely, when the lattice parameters increase, the stress and the optical gap also increase. These observations imply that the optical gap, structural parameters, and residual stresses share a similar response to the isopropanol synthesis conditions (temperature and pressure).

Figure 5 illustrates the photoluminescence (PL) spectra of ZnO nanostructures fabricated through the sol-gel process under subcritical isopropanol conditions. These spectra were recorded at room temperature using an excitation wavelength of 350 nm. In all spectra, a noticeable absorption band is observed around 388 nm, accompanied by a shoulder around 377 nm. The shoulder at 377 nm transforms into a distinct band for the sample processed at 120°C. These two emissions are referred to as excitonic emissions at 388 nm (originating from transitions between excitonic states and the valence band) and band-to-band emissions at 377 nm (associated with transitions between the conduction band and the valence band) [30,31]. Photoluminescence emissions in the visible range are often attributed to defects within the material's structure, such as oxygen vacancies, zinc vacancies, interstitials, and antisites. The sample processed at 90°C exhibits broad absorption in the visible spectrum, although this characteristic is nearly absent in the other samples. Additionally, all samples exhibit two weak emission bands at 466 nm (blue emission) and 539 nm (green emission), likely induced by defects in the crystallite structure [2,32].

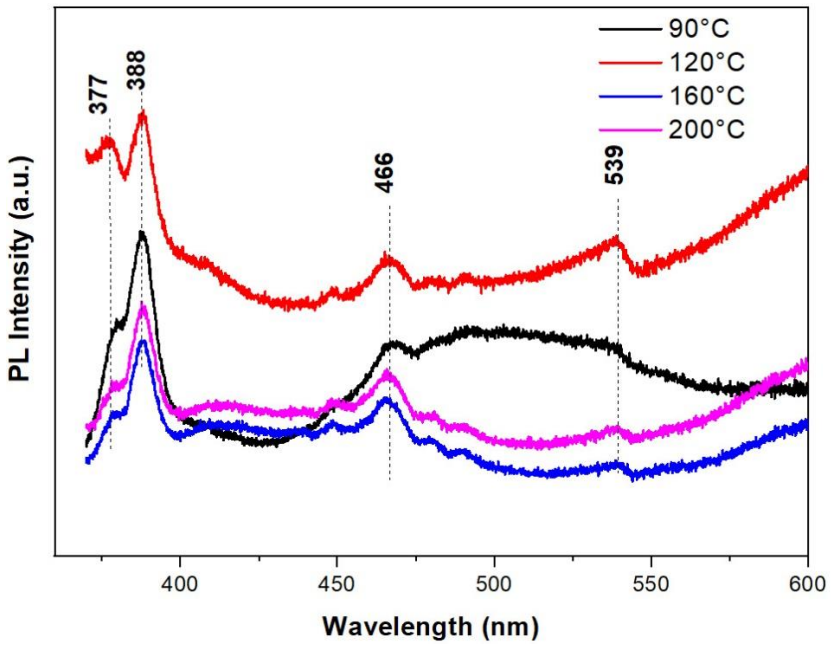

Fig. 5. PL spectra of ZnO nanostructures produced under parametric conditions (90°C, 2bar), (120°C, 6bar), (160°C, 14bar) and (200°C, 30bar).

Figure 6 illustrates the deconvolution curves of the photoluminescence (PL) spectra, allowing for the examination of changes in UV emissions from ZnO nanostructures in relation to the processing parameters. It is noticeable that the position of the bands, specifically at 388 nm and 377 nm, remains nearly identical across all samples, except for the one processed at 120°C. Moreover, the behaviors of the intensity and the width of these bands appear to be unaffected by the processing conditions, with the exception of the sample processed at 120°C.

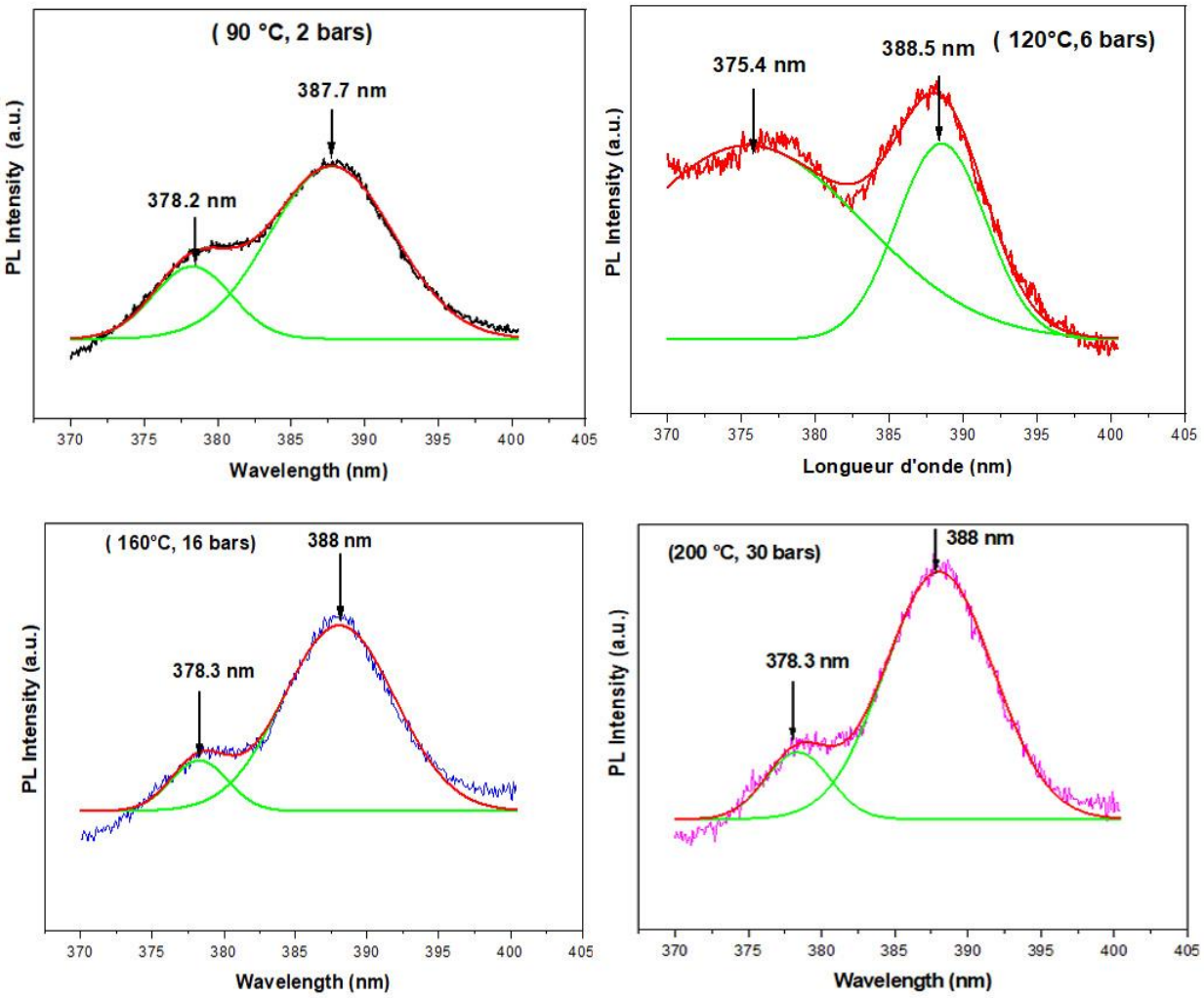

Fig. 6. Deconvolution of photoluminescence spectra in the UV region.

5. Conclusions

This study focuses on the synthesis, structural characterization, and optical properties of ZnO nanostructures. The samples were synthesized using the sol-gel method under different temperature and pressure conditions of isopropanol, specifically (90°C, 2 bar), (120°C, 6 bar), (160°C, 14 bar), and (200°C, 30 bar). The elaborated samples were subsequently annealed at 500°C for 2 hours and subjected to analysis using techniques such as X-ray diffraction (DRX), attenuated total reflection (ATR), UV-Visible spectroscopy, and photoluminescence (PL). The DRX analysis confirmed that all synthesized ZnO crystallites exhibited a polycrystalline structure of the hexagonal wurtzite type. Interestingly, the cell parameters and residual stresses were found to be dependent on the processing conditions (temperature and pressure), while the crystallite size remained unaffected. The ATR spectra indicated that the synthesized nanostructures possessed a high degree of purity. Additionally, the position of the absorption band associated with the Zn-O vibrational bond of ZnO shifted towards smaller wavenumber values as the temperature increased. The UV-Visible spectroscopy results revealed that the absorption band shifted towards shorter wavelengths with increasing temperature and pressure. The optical gap exhibited a similar

behavior to the lattice parameters and stress within the nanoparticles. Furthermore, the PL measurements demonstrated that higher processing temperatures and pressures led to increased UV emission and reduced visible emission. Importantly, the positions of the UV emission bands were not strongly influenced by the synthesis parameters.

References

[1] V. Ischenko, S. Polarz, D. Grote, V. Stavarache, K. Fink, and M. Driess, Zinc oxide nanoparticles with defects, Advanced Functional Materials, vol. 15, pp. 1945-1954, 2005.

[2] A. Ishizumi and Y. Kanemitsu, Structural and luminescence properties of Eu-doped ZnO nanorods fabricated by a microemulsion method, Applied physics letters, vol. 86, p. 253106, 2005.

[3] C. Klingshirn, ZnO: From basics towards applications, Physica status solidi (b), vol. 244, pp. 3027-3073, 2007.

[4] R. Kumar, G. Kumar, O. Al-Dossary, and A. Umar, ZnO nanostructured thin films: Depositions, properties and applications—A review, Materials Express, vol. 5, pp. 3-23, 2015.

[5] A. Di Mauro, M. E. Fragala, V. Privitera, and G. Impellizzeri, ZnO for application in photocatalysis: From thin films to nanostructures, Materials Science in Semiconductor Processing, vol. 69, pp. 44-51, 2017

[6] Z. Seow, A. Wong, V. Thavasi, R. Jose, S. Ramakrishna, and G. Ho, Controlled synthesis and application of ZnO nanoparticles, nanorods and nanospheres in dye-sensitized solar cells, Nanotechnology, vol. 20, p. 045604, 2008.

[7] A. Wibowo, M. A. Marsudi, M. I. Amal, M. B. Ananda, R. Stephanie, H. Ardy, and L. J. Diguna, ZnO nanostructured materials for emerging solar cell applications, RSC advances, vol. 10, pp. 42838-42859, 2020.

[8] X. Wang, M. Ahmad, and H. Sun, Three-dimensional ZnO hierarchical nanostructures: Solution phase synthesis and applications, Materials, vol. 10, p. 1304, 2017.

[9] C. L. Hsu and S. J. Chang, Doped ZnO 1D nanostructures: synthesis, properties, and photodetector application, small, vol. 10, pp. 4562-4585, 2014.

[10] F. Mouzaia, D. Djouadi, A. Chelouche, L. Hammiche, and T. Touam, Structural and optical investigations of pure and Al-doped ZnO nano-aerogels: effects of supercritical organic solvent, Applied Physics A, vol. 125, pp. 1-12, 2019.

[11] M. Meddouri, L. Hammiche, O. Slimi, D. Djouadi, and A. Chelouche, Effect of cerium on structural and optical properties of ZnO aerogel synthesized in supercritical methanol, Materials Science-Poland, vol. 34, pp. 659-664, 2016.

[12] H. R. Ghorbani, F. P. Mehr, H. Pazoki, and B. M. Rahmani, Synthesis of ZnO nanoparticles by precipitation method, Orient. J. Chem, vol. 31, pp. 1219-1221, 2015.

[13] Z. A. Abdelouhab, D. Djouadi, A. Chelouche, and T. Touam, Structural, morphological and Raman scattering studies of pure and Ce-doped ZnO nanostructures elaborated by hydrothermal route using nonorganic precursor, Journal of Sol-Gel Science and Technology, vol. 95, pp. 136-145, 2020.

[14] H. Van Han, D. H. Du, and D. A. Tuan, Comparing the Application of Gas Sensor Fabrication of Nanomaterials ZnO Fabricated by Hydrothermal and Chemical Vapor Deposition Method, in Advances in Engineering Research and Application: Proceedings of the International Conference on Engineering Research and Applications, *ICERA 2020*, 2021, pp. 254-261.

[15] A. Dauletbekova, L. Vlasukova, Z. Baimukhanov, A. Akilbekov, A. Kozlovskyi, S. Giniyatova, A. Seitbayev, A. Usseinov, and A. Akylbekova, Synthesis of ZnO nanocrystals in SiO_2/Si track template: effect of electrodeposition parameters on structure, Physica status solidi (b), vol. 256, p. 1800408, 2019.
[16] N. Kumaresan and K. Ramamurthi, Synthesis of ZnO/rGO nanocomposites by wet impregnation method for photocatalytic performance against RhB dye and 4-chlorophenol under UV light irradiation, Journal of Materials Science: Materials in Electronics, vol. 31, pp. 3361-3374, 2020.
[17] S. Arya, P. Mahajan, S. Mahajan, A. Khosla, R. Datt, V. Gupta, S.-J. Young, and S. K. Oruganti, Influence of processing parameters to control morphology and optical properties of Sol-Gel synthesized ZnO nanoparticles, ECS Journal of Solid State Science and Technology, vol. 10, p. 023002, 2021.
[18] S. Farhat, M. Rekaby, and R. Awad, Synthesis and characterization of Er-doped nano ZnO samples, Journal of Superconductivity and Novel Magnetism, vol. 31, pp. 3051-3061, 2018.
[19] B. Clarke and K. Ghandi, The Interplay of Growth Mechanism and Properties of ZnO Nanostructures for Different Applications, Small, p. 2302864, 2023.
[20] O. Marin, V. González, N. Budini, M. Tirado, and D. Comedi, The influence of methanol and NH 4 Cl on solvothermal ZnO synthesis and properties, Applied Physics A, vol. 126, pp. 1-13, 2020.
[21] R. Shi, P. Yang, X. Dong, Q. Ma, and A. Zhang, Growth of flower-like ZnO on ZnO nanorod arrays created on zinc substrate through low-temperature hydrothermal synthesis, Applied Surface Science, vol. 264, pp. 162-170, 2013.
[22] W. Tang and J. Wang, Mechanism for toluene detection of flower-like ZnO sensors prepared by hydrothermal approach: Charge transfer, Sensors and Actuators B: chemical, vol. 207, pp. 66-73, 2015.
[23] G. Vijayaprasath, R. Murugan, T. Mahalingam, Y. Hayakawa, and G. Ravi, Enhancement of ferromagnetic property in rare earth neodymium doped ZnO nanoparticles, Ceramics International, vol. 41, pp. 10607-10615, 2015.
[24] A. S. H. Hameed, C. Karthikeyan, A. P. Ahamed, N. Thajuddin, N. S. Alharbi, S. A. Alharbi, and G. Ravi, In vitro antibacterial activity of ZnO and Nd doped ZnO nanoparticles against ESBL producing Escherichia coli and Klebsiella pneumoniae, Scientific reports, vol. 6, pp. 1-11, 2016.
[25] S. Kumar and P. Sahare, Nd-doped ZnO as a multifunctional nanomaterial, Journal of Rare Earths, vol. 30, pp. 761-768, 2012.
[26] B. Abdullah and D. Tahir, Quantitative analysis of X-Ray diffraction spectra for determine structural properties and deformation energy of Al, Cu and Si, Journal of Physics: Conference Series, 2019, p. 012052.
[28] Y. Zong, Z. Li, X. Wang, J. Ma, and Y. Men, Synthesis and high photocatalytic activity of Eu-doped ZnO nanoparticles, Ceramics International, vol. 40, pp. 10375-10382, 2014.
[28] Y. Liu, W. Luo, R. Li, G. Liu, M. R. Antonio, and X. Chen, Optical spectroscopy of Eu3+ doped ZnO nanocrystals, The Journal of Physical Chemistry C, vol. 112, pp. 686-694, 2008.
[29] J. Yang, X. Li, J. Lang, L. Yang, M. Wei, M. Gao, X. Liu, H. Zhai, R. Wang, and Y. Liu, Synthesis and optical properties of Eu-doped ZnO nanosheets by hydrothermal method, Materials Science in Semiconductor Processing, vol. 14, pp. 247-252, 2011.
[30] M. Wang, C. Huang, Z. Huang, W. Guo, J. Huang, H. He, H. Wang, Y. Cao, Q. Liu, and J. Liang, Synthesis and photoluminescence of Eu-doped ZnO microrods prepared by hydrothermal method, Optical Materials, vol. 31, pp. 1502-1505, 2009.

[31] A. Singh, P. Arya, D. Choudhary, S. Kumar, A. Srivastava, and I. Singh, Cost-effective ZnO–Eu 3+ films with efficient energy transfer between host and dopant, SN Applied Sciences, vol. 2, pp. 1-9, 2020.

[32] M. Meddouri, D. Djouadi, A. Chelouche, T. Touam, and A. Chergui, Effect of co-solvent on structural and morphological properties of ZnO aerogel prepared by a modified sol-gel process, The European Physical Journal-Applied Physics, vol. 66, 2014

CHARACTERIZATIONS OF PURE AND Eu-DOPED ZnO AEROGELS NANOSTRUCTURES ELABORATED BY A MODIFIED SOL GEL PROCESS

Fatiha Bedhouche[1,2], Djamel Djouadi[2*], Ahcène Soualah[1], Azeddine Chelouche[2], Tahar Touam[3]

[1]Laboratoire de Physicochimie des Matériaux et Catalyse (LPCMC), Université de Bejaia, Route de Targa ou Zemmour, Bejaia, (06000), Algeria,
[2]Laboratoire de Génie de l'Environnement (LGE), Université de Bejaia, Route de Targa ou Zemmour, Bejaia, (06000), Algeria,
[3]Laboratoire Laboratoire des Semi-conducteurs, Université Badji Mokhtar-Annaba, BP12, 23000 Annaba, Algeria
**E-mail: djamel.djouadi@univ-bejaia.dz*

(Received, 20 november, 2023)

https://doi.org/10.53081/mjps.2023.22-1.04

Abstract

Herein we report on the structural and optical properties of pure and Eu-doped (3% at.) ZnO aerogels nanostructures (ZnO-ans) synthesized by sol-gel associated with drying at supercritical conditions of isopropanol (254 °C, 54 bars). The samples were investigated using X-ray diffraction (XRD), SEM, UV-visible spectroscopy, FTIR and photoluminescence (PL). XRD studies exhibit the formation of a high crystal quality ZnO wurtzite hexagonal structure. The UV-visible measurements point out that the absorption intensity and the band gap energy increase after Eu-doping. FTIR analysis confirms the formation of ZnO phase and reveals a shift toward longer wavenumber of the Zn-O absorption band after Eu -doping. SEM images show that Eu^{3+} ions lead to change the morphology of ZnO crystalline from pastille to sphere. PL measurements reveal a decrease of UV luminescence intensity and an increase of the visible one due to Eu-doping.

Keywords: ZnO, Eu-doping, supercritical isopropanol, structure, morphology, photoluminescence.

1. Introduction

Zinc oxide (ZnO) nanostructures have garnered significant attention in research due to their exceptional and distinctive characteristics, rendering them highly valuable in various fields including optics, photonics, sensors, and catalysis [1]. With its considerable band gap of 3.37 eV and a substantial excitonic binding energy of 60 meV at room temperature, ZnO holds great promise as a photoactive material specifically suited for generating short wavelength light emitting devices. Additionally, it serves as an excellent host matrix for incorporating optically active impurities [2]. By altering the shape and size of particles through the incorporation of different elements, the band gap and optical properties of ZnO nanostructures can be adjusted.

One effective approach is doping with rare-earth (RE) elements, which is a widely recognized technique for tailoring the properties of ZnO nanostructures to suit specific applications and to overcome their inherent limitations [3]. The luminescent properties of rare-earth (RE) ions surpass those of transition metal elements due to the fact that their 4f intra-shell transitions arise from narrow and highly intense emission lines [4,5]. Trivalent rare-earth (RE) ions, such as Eu3+, find extensive usage in a range of applications that require red emissions, primarily because of their attributes including linear emission, exceptional color purity, long fluorescence lifetime, and the presence of stable intra-4f shell transitions within their ions [5,6]. The relationship between the synthetic method and the spontaneous emission probability of optical transitions involving Eu^{3+} ions incorporated into a host material, such as ZnO, is widely recognized [7]. ZnO nanostructures doped with Eu^{3+} ions have been successfully synthesized employing diverse methods, including gel-combustion [8], sonochemical [9], chemical bath [10], hydrothermal [11], and sol-gel techniques [12]. Of all those synthesis procedures, the sol-gel technology is one of common method to prepare Eu-doped ZnO nanostructures due to its simplicity, safety and low cost. The sol-gel method, combined with supercritical drying of organic fluids, represents a procedure that possesses distinctive characteristics, including rapid mass transfer, reproducibility, near-zero surface tension, and efficient solvent removal [13]. This approach enables direct control over various properties, such as size, crystal quality, and chemical composition, making it an effective strategy for comprehending the mechanism of nanostructure formation [14,15]. ZnO nanostructures aerogels have been successfully synthesized utilizing various supercritical fluids, including methanol [16], ethanol [17,18], acetone [16,17], and isopropanol [19]. Notably, among these supercritical organic solvents, isopropanol has demonstrated the capability to produce ZnO nanostructures with improved crystalline quality and optical properties [19].

To our knowledge, there is currently no existing literature on the properties of aerogel-form ZnO nanostructures doped with Eu (3% at.). Hence, in this study, we present the fabrication of pure ZnO aerogel nanostructures as well as Eu-doped ZnO aerogel nanostructures (referred to as ZnO-ans) through a sol-gel process combined with supercritical drying using isopropanol. Furthermore, we thoroughly investigate and discuss the structural and optical properties of the synthesized samples.

2. Experimental procedures

Pure and Eu (3 at. %)-doped zinc oxide aerogels nanostructures (ZnO-ans) were synthesized using, in appropriate masses and volumes, zinc acetate dihydrate (Zn $(C_2H_3O_2)_2$, $2H_2O$) as precursor, methanol as solution solvent and europium nitrates (Eu $(NO_3)_3$, $6H_2O$) as doping element source. The mixture was subjected to continuous magnetic stirring for a duration of 20 minutes until a whitish solution was attained. Subsequently, the stable and homogeneous solutions were subjected to supercritical drying using isopropanol at conditions of 240 °C and 54 bars. In the case of the doped solution, the atomic ratio of [Eu] to [Zn] was fixed at 0.03 (3%). Both solutions were prepared under identical conditions. Once the supercritical conditions were reached, the solvent was promptly removed, and the autoclave was allowed to naturally cool down to room temperature. The resulting ZnO-ans were subsequently characterized without any additional treatments.

The crystal structure of the products was studied using a diffractometer type PanAlytical where the X-rays are produced from a radiation source CuK_α ($\lambda = 0.154$ nm), with an acceleration voltage of 40 kV and a current of 30 mA. FTIR spectra were recorded with an Agilent 630-IR spectrometer. A thermo-scientific evolution 201 UV-Vis spectrophotometer was used to

investigate the UV-visible properties. The morphology of the samples was characterized by scanning electron microscope type Thermo Scientific Quattro ESEM -ETD. The PL spectra were recorded at room temperature with LabSolutions RF 6000 spectrophotometer using an excitation wavelength of 350 nm.

3. Results and discussions

Figure 1 illustrates the X-ray diffraction (XRD) patterns of both pure and Eu-doped ZnO aerogels synthesized using supercritical isopropanol. In the patterns, distinct and well-defined peaks are observed for both samples, corresponding to the characteristic crystal structure of ZnO nanoparticles with a perfect wurtzite structure, as indicated by the JCPDS standard (N° 36-1451) data, with lattice parameters a_0 = 3.249 Å and c_0 = 5.206 Å. Notably, the XRD patterns reveal that the synthesized products are pure ZnO, exhibiting no secondary phases or impurities associated with metallic Eu or other europium compounds. This observation suggests that the Eu^{3+} ions have successfully incorporated into the ZnO lattice.

To examine the impact of Eu doping on the structural properties of ZnO aerogels (ZnO-ans), the three most significant XRD peaks are presented in the inset of Figure 1. In the inset, it can be observed that the diffraction peak positions of the doped aerogel exhibit a slight shift towards the lower diffraction angles in comparison to the undoped sample. This shift indicates a minor increase in the lattice parameters. The observed shift can be attributed to lattice mismatch, distortion, and strain within the ZnO lattice [20]. Similar trends in ZnO cell parameters following europium doping have been reported by other researchers [21,22]. Additionally, no significant changes are observed in the width and intensity of the XRD peaks, suggesting that Eu doping has not induced any notable modifications in the size of the synthesized ZnO-ans crystallites

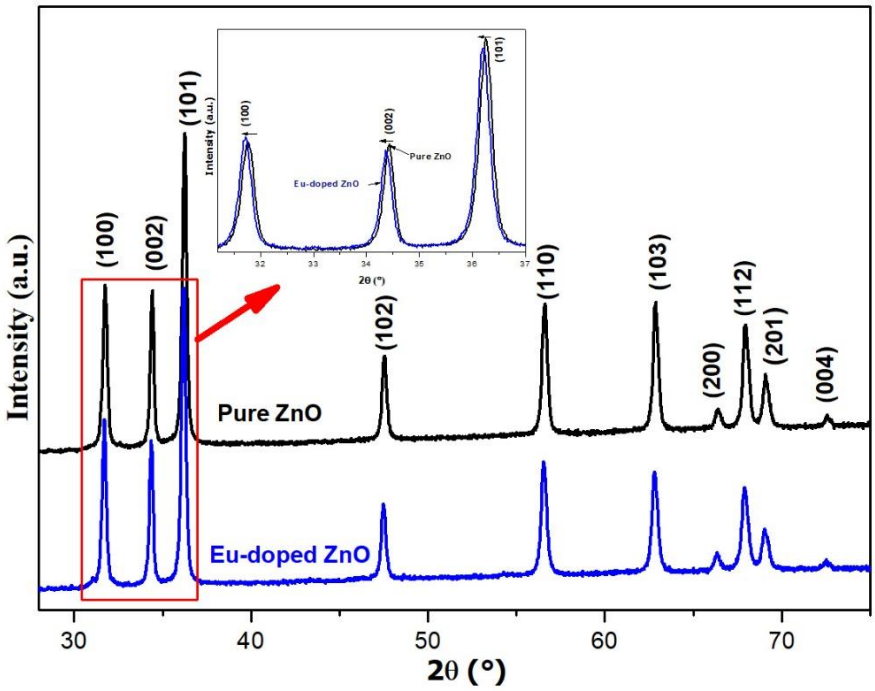

Fig. 1. XRD patterns of pure and Eu-doped ZnO-ans synthesized in supercritical isopropanol. The inset shows XRD patterns comparison of the three most important peaks.

The lattice constants *a* and *c* for both ZnO-ans are calculated respectively from the positions of (100) and (002) using the formulas ($a = \frac{\lambda}{\sqrt{3}sin\theta}$) and ($c = \lambda/sin\theta$), where θ is the diffraction angle and λ is the X-rays wavelength (1.54 Å) [23].

The average crystallites size of both ZnO-ans is calculated from the most pronounced XRD peaks using the well-known Scherrer formula ($D = 0.90/(\Delta\beta.cos\theta)$),where Δβ is the full-width at half maximum (in radians) of the XRD peak. The length L of Zn-O bond is calculated using the formula($L = \sqrt{\frac{a^2}{3} + (0.5 - u)^2c^2}$), where, in wurtzite crystallographic structure, the parameter u is given by $\left(u = \frac{a^2}{3c^2} + 0.25\right)$ [23]. The crystalline quality of the elaborated ZnO-ans is estimated by the empirical formula ($X_c = \left(\frac{0.24}{\beta_{002}}\right)^3$), where β_{002} is the full width at half maximum (in degrees) of (002) peak) [24]. The induced strain ϵ is calculated from the most pronounced XRD peaks using the equation ($\epsilon = (\beta_{hkl}\, cos\theta)/4$) [25]. The micro-strain along the c-axis (ε_z) is calculated using the formula ($\varepsilon_z = \frac{c - c_0}{c_0}$),where c and c_0 (5.206 Å) are the calculated and standard lattice constant parameters, respectively [26]. All these parameters are calculated and summarized in Table 1.

Table 1. Structural parameters of pure and Eu-doped ZnO aerogels nanostructures.

ZnO-ans	*a (Å)*	*c (Å)*	*D (nm)*	*L (Å)*	X_c	ϵ (Lines^{-2}.m^{-4})	ε_z(x10^{-4})	Cell volume V (Å^3)
Pure	3.2489	5.2044	33	1.8795	1.11	1.7 10^{-4}	-3.07	47.5643
Eu-doped	3.2531	5.2107	33	1.9626	1.36	9.8 10^{-4}	+9.02	47.7539
JCPDS 36-1451	3.2490	5.2060	/	1.9770				47.5906

The calculated values reveal that the lattice parameters of Eu-doped ZnO aerogels (ZnO-ans) exhibit minimal variation (*a* = 2.2531 Å, *c* = 5.2107 Å) compared to the pure ZnO-ans, which had lattice parameters of (*a* = 3.2489 Å, *c* = 5.2044 Å). This change in lattice parameters can be attributed to the substitutional replacement of Eu^{3+} impurity ions in the Zn^{2+} ionic sites within the ZnO lattice. Such substitution leads to a slight misfit due to the different ionic radii of Eu^{3+} ions (0.95 Å) compared to Zn^{2+} ions (0.74 Å). This interpretation is further supported by the increase in the unit cell volume (*V*) from 47.5643 Å^3 to 47.7539 Å^3 and the elongation of the Zn-O bond length (L) from 1.8795 Å to 1.9626 Å following Eu doping.

Similar observations have been reported in several other published studies [6,21,27]. The introduction of Eu doping in ZnO aerogels demonstrates a slight enhancement in the crystal quality, as evident from the increase in the X_C value from 1.11 to 1.36. This increase indicates that a majority of the Eu^{3+} ions occupy vacant Zn^{2+} sites within the lattice. The average size of the crystallites remains unchanged following the incorporation of Eu^{3+} ions into the ZnO lattice, measuring at around 33 nm. Additionally, it is noteworthy that there is an increase in induced strain within the lattice after Eu doping, leading to local distortion of the crystal structure. This distortion arises from the disparity in ionic radii between Zn^{2+} and Eu^{3+} ions. A similar phenomenon was observed by Sayari *et al*. [28] in (Ni, Al)-doped ZnO nanopowders synthesized

via the sol-gel process. Furthermore, it is worth mentioning that the micro-strain along the c-axis (ε_z) is found to be compressive in pure ZnO-ans and tensile in the doped samples. This behavior can be attributed to the initially trapped Eu^{3+} ions occupying non-equilibrium positions, which, at this concentration (3 at. %), may have shifted to equilibrium positions, thereby releasing the tensile strain. Belkhaoui *et al*. [26] also reported a similar behavior in (Al, Mn)-doped ZnO nanopowders synthesized through the coprecipitation method.

Figure 2 presents scanning electron microscope (SEM) images of undoped and Eu-doped ZnO aerogel nanostructures, displayed at two different magnifications. The SEM images reveal that the morphology of pure ZnO aerogels exhibits a capsular shape with non-uniform sizes, where the particles are well separated and randomly oriented. In contrast, the Eu-doped ZnO sample highlights particles with a spherical shape, exhibiting a more uniform size distribution within a narrow range. These nanospheres tend to agglomerate, forming denser micrograins that are practically spherical in nature. The alteration in morphology following Eu doping can be attributed to the disparity in ionic radii between Eu^{3+} and Zn^{2+} ions, as well as the difference in electronegativity between Eu and Zn. It is commonly understood that the growth rate and nucleation process of nanocrystals play a crucial role in determining the morphology of ZnO crystals during synthesis [29,30]. Based on these observations, it can be concluded that Eu doping significantly influences the morphology of ZnO-ans.

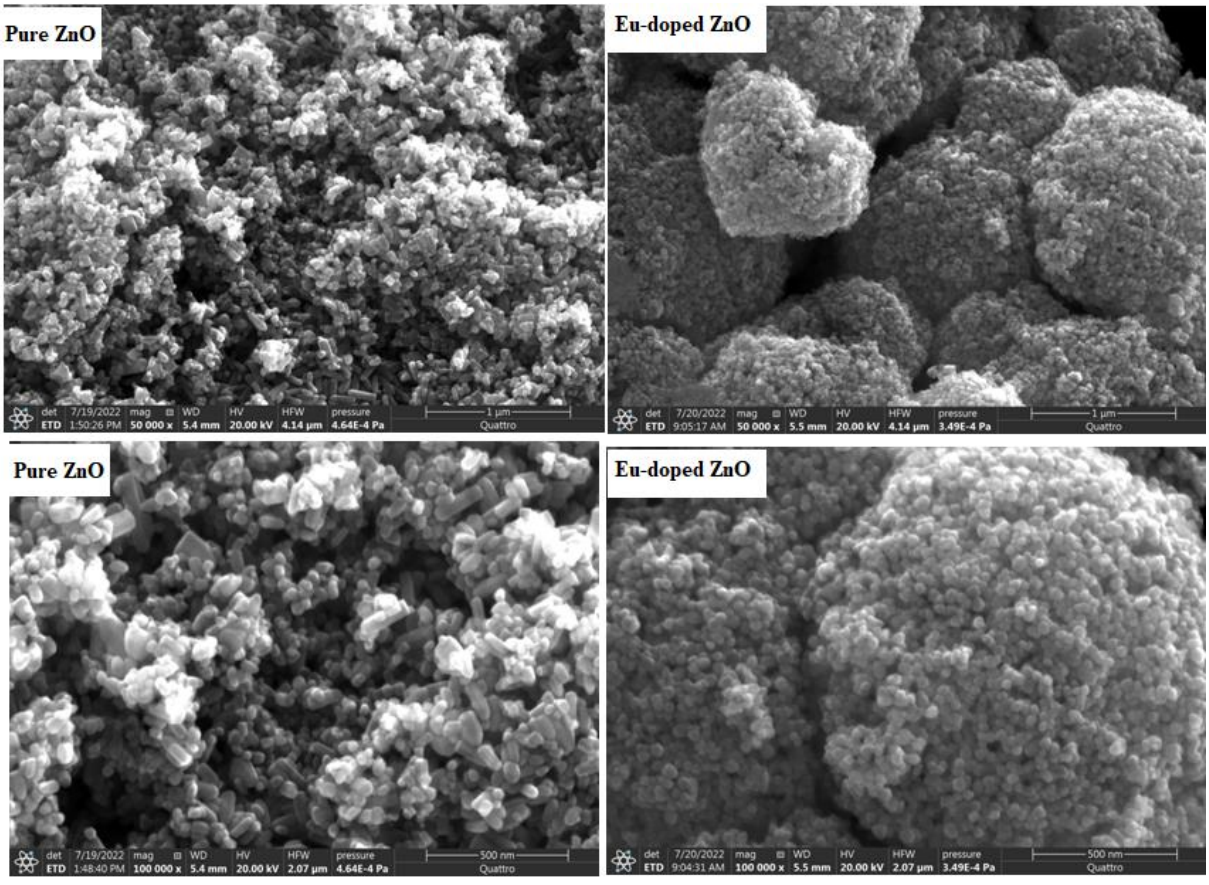

Fig. 2. SEM images of pure and Eu-doped ZnO aerogels nanostructures synthesized in supercritical isopropanol.

Infrared spectroscopy is a valuable technique employed to gather insights into the chemical bonding present in a material and to identify its elemental components. Attenuated Total Reflectance (ATR) is a contact sampling method that utilizes a crystal with remarkable infrared transmitting properties and a high refractive index. Among the various sampling techniques available to Fourier Transform Infrared (FT-IR) spectroscopists, ATR is widely favored due to its speed, non-destructiveness, and the absence of sample preparation requirements.

Figure 3 illustrates the ATR spectra of both pure and Eu-doped ZnO aerogels synthesized using supercritical isopropanol. The strong and sharp absorption band observed in the range of 400-590 cm^{-1} corresponds to the Zn-O stretching mode, confirming the presence of ZnO crystals. Notably, this absorption band undergoes a slight shift towards higher wavenumbers after Eu^{3+} doping, as depicted in the inset of Figure 3. This subtle change in the position of the absorption band following Eu^{3+} doping indicates the successful incorporation of Eu^{3+} ions into the ZnO lattice structure. The shift in the absorption band can be attributed to the alteration in bond length resulting from the substitution of Zn^{2+} with Eu^{3+} ions [31].

The substitution of Zn^{2+} sites with Eu^{3+} ions is expected to cause an upward shift in the transverse optical modes, as the Eu atom is heavier than Zn. This behavior aligns with established theories regarding vibrational modes in mixed crystals [23]. The observed increase in the intensity of the absorption band corresponding to Zn-O bond vibrations after Eu doping can be attributed to the higher number of these bonds resulting from the substitution process. Additionally, the increase in intensity could potentially be influenced by Eu-O vibration bonds, which are typically observed at around 462 cm^{-1} [32]. The infrared reflectance absorption bands observed at 1543 cm^{-1} and 1440 cm^{-1} are attributed to the asymmetric and symmetric stretching vibrations of carboxylate groups. These groups may originate from small residues of precursor materials [33]. Notably, no bands associated with the Eu-O stretching mode of europium oxides are detectable, which suggests that the segregation of Eu oxides is unlikely to have occurred in the sample.

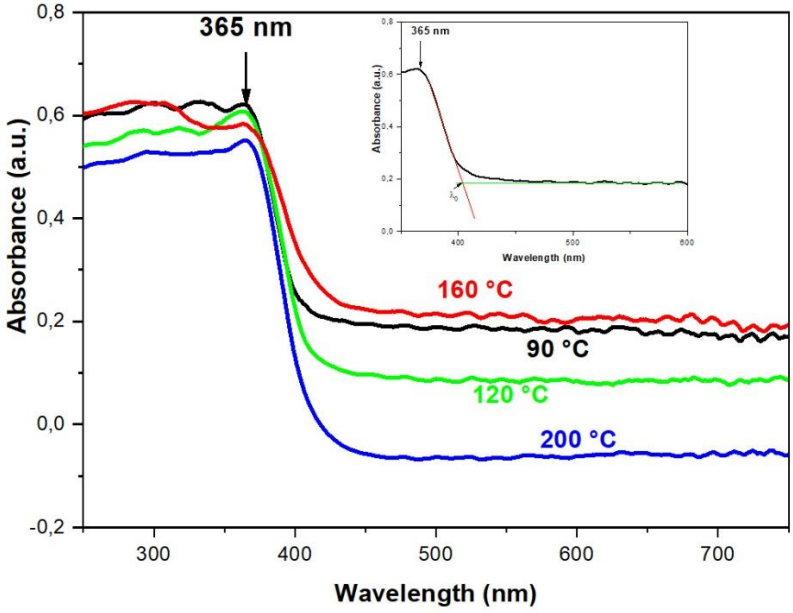

Fig. 4. ATR spectra of pure and Eu-doped ZnO aerogels nanostructures synthesized in supercritical isopropanol. The inset shows the magnification of Zn-O bond band.

Figure 4 presents the UV-visible diffuse reflectance spectra of both pure and Eu-doped ZnO aerogels (ZnO-ans). In both spectra, a prominent absorption peak is observed, which is attributed to the band gap absorption resulting from electron transitions in ZnO from the valence band to the conduction band [34]. Notably, after Eu doping, a noticeable blue shift is observed in the excitonic absorption maximum, indicating an enhancement in the optical band. This shift towards the lower-wavelength side suggests an improvement in the crystal quality of ZnO-ans, as the growth of ZnO-ans is inhibited. The exciton absorption maximum of the undoped ZnO-ans experiences a shift from 363 nm to 356 nm following Eu doping. It is widely recognized that a decrease in the size of crystallites typically results in a blue shift, indicating an increase in the band gap. However, in our specific case, X-ray diffraction (XRD) analysis reveals no significant variation in the size of crystallites following Eu doping. Therefore, the observed blue shift in the UV-visible spectra cannot be attributed to changes in crystallite size.

The optical band gap (E_g), determined from the absorbance spectrum and equal to the difference between the HOMO and LUMO energy levels, corresponds to the first optical transition of lower energy that can be absorbed by the material [35]. The estimated value of the optical band gap is given by the formula ($E_g(eV) = \frac{1240}{\lambda_0}\ (nm)$), where λ_0 is determined by the intersection of the linear region of the absorbance and the constant visible absorbance as shown in Figure 3. The estimated values of the band gap are found to be 3.14 eV in the doped and 3.11 eV in pure ZnO-ans. Zong *et al.* reported the same behavior of the UV-visible diffuse reflectance spectra in Eu-doped ZnO nanoparticles synthesized by precipitation method and attributed the blue shift to the broadening of the band gap [36]. Also, many authors suggested that dopant induced strain is likely to be responsible for blue shift of absorption peak in rare earths doped ZnO nanostructures [37,38]. Li *et al.* reported that the blue shift in Eu-doped ZnO is due to Moss-Burstein effect [34]. This means that the unoccupied energy states at the bottom of the conduction band are separated from the valence band, and the band gap becomes larger when Eu^{3+} ions are gradually increased.

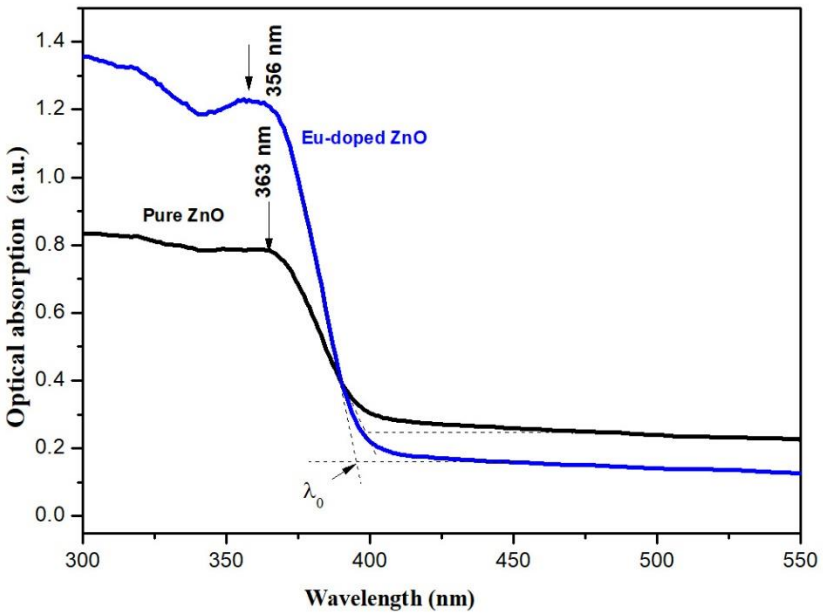

Fig. 4. UV-Visible reflectance spectra of pure and Eu-doped ZnO aerogels nanostructures synthesized in supercritical isopropanol.

Figure 5 illustrates the room temperature photoluminescence (PL) emission spectra of both pure and Eu-doped ZnO aerogels (ZnO-ans), with an excitation wavelength of 350 nm. In pure ZnO, the PL emission appears to be more intense in the ultraviolet (UV) range, whereas in the doped sample, the intensity is higher in the visible region. When excited at 350 nm and within the investigated wavelength range, two distinct bands are observed in the PL emission of ZnO-ans: (1) a UV emission band below 400 nm and (2) a broad visible emission band spanning from 400 nm to 650 nm. In the undoped ZnO-ans, the intense UV emission consists of two adjacent bands located at 379.3 nm (corresponding to 3.269 eV) and 386.6 nm (corresponding to 3.207 eV). The emission at 379.3 nm in the undoped ZnO-ans is attributed to the band-to-band transition, while the emission at 386.6 nm is assigned to free excitons. The small energy difference of approximately 0.062 eV (~62 meV) between these two emission lines supports this assignment. On the other hand, in the doped ZnO-ans, the UV emission is less intense and is characterized by a band centered around 388 nm (3.195 eV), which corresponds to excitonic transitions. Additionally, a shoulder is observed at 378.6 nm (3.275 eV), which is assigned to band-to-band transitions. The emission at 379.3 nm in the undoped ZnO-ans is attributed to the band-to-band transition, while the emission at 386.6 nm is assigned to free excitons. The small energy difference of approximately 0.062 eV (~62 meV) between these two emission lines supports this assignment. On the other hand, in the doped ZnO-ans, the UV emission is less intense and is characterized by a band centered around 388 nm (3.195 eV), which corresponds to excitonic transitions. Additionally, a shoulder is observed at 378.6 nm (3.275 eV), which is assigned to band-to-band transitions.

Following Eu doping, the band-to-band emission experiences a slight blue shift of 11 meV towards shorter wavelengths, while the exciton emission undergoes a small red shift of 6 meV towards longer wavelengths [39]. The decrease in UV emission intensity observed after Eu doping in the UV region can be attributed to a phenomenon known as concentration quenching, whereby the presence of Eu^{3+} ions leads to increased interactions and enhanced non-radiative processes that result in photoluminescence (PL) quenching. The introduction of europium atoms in the ZnO lattice results in a reduced recombination rate of electron-hole pairs, indicating that the photogenerated electrons are being trapped at energy levels created by defects within the band gap [40-43]. The visible emission in the spectrum is characterized by a broad and significant intensity, which can be attributed to point defects. This wide visible band consists of multiple bands, with three prominent ones observed around 466 nm, 522 nm, and 634 nm. Upon introducing Eu atoms into the ZnO lattice, the intensity of the visible emission increases due to the higher concentration of intrinsic defects resulting from the doping process [44-46]. Studies by Djurisic *et al*. [47,48] have indicated that the emission in ZnO nanostructures is primarily influenced by native defects. The blue emission is attributed to surface defects of ZnO crystallites, the green emission is associated with oxygen vacancies, and the red emission is linked to zinc deficiencies. Based on these findings, it can be inferred that the Eu-doped ZnO nanostructures synthesized in supercritical isopropanol exhibit a high abundance of intrinsic defects, including surface defects and oxygen vacancies, which contribute to the enhanced visible emission.

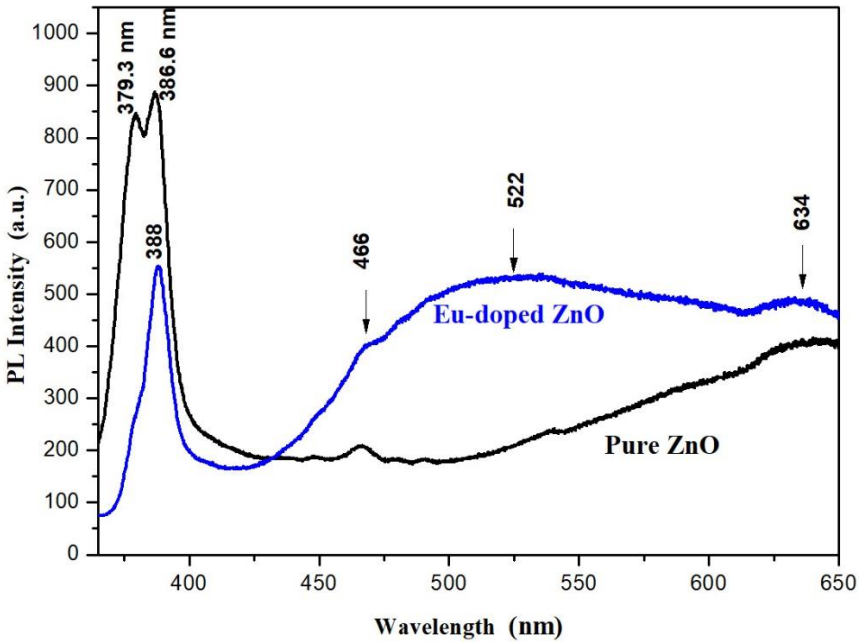

Fig. 5. Room temperature photoluminescence (PL) spectra of pure and Eu-doped ZnO aerogels nanostructures synthesized in supercritical isopropanol.

5. Conclusions

Pure and Eu-doped ZnO aerogel nanostructures, with a doping concentration of 3 at. %, were successfully synthesized using a sol-gel process under supercritical drying conditions with isopropanol. X-ray diffraction (XRD) analysis confirmed that the obtained samples exhibit a polycrystalline hexagonal wurtzite structure of ZnO, with slight changes observed in the cell parameters after Eu doping. Infrared spectroscopy revealed that the intensity of the absorption band associated with the Zn-O vibration bond increased and shifted towards higher wavenumbers. The absorption measurements indicated an increase in both absorption and the optical gap energy following Eu doping. Furthermore, photoluminescence measurements demonstrated that the UV emission decreased while the visible emission increased upon Er doping.

References

[1] V.S. Bhati, M. Hojamberdiev, M.J.E.R. Kumar, Enhanced sensing performance of ZnO nanostructures-based gas sensors: A review, Energy Repprts 6 (2020) 46-62.

[2] L. Armelao, F. Heigl, A. Jürgensen, R. Blyth, T. Regier, X.-T. Zhou, T.J.T.J.o.P.C.C. Sham, X-ray excited optical luminescence studies of ZnO and Eu-doped ZnO nanostructures, J. Phys. Chem. C 111 (2007) 10194-10200.

[3] S.M. Ahmed, H.J.M.S.i.S.P. Imam, Characterization and photocatalytic activity of Eu: ZnO & Au/Eu: ZnO nanoparticles prepared by laser ablation in water, Materials Science in SemiconductorProcessing 115 (2020) 105128.

[4] P. Aneesh, M.J.B.o.M.S. Jayaraj, Red luminescence from hydrothermally synthesized Eu-doped ZnO nanoparticles under visible excitation, Bulletin of Materials Sciene 33 (2010) 227-231.

[5] Z. Lu, F. He, P. Xu, Y. Teng, B.J.J.o.W.U.o.T.-M.S.E. Wang, Effects of heat-treatment temperature on Eu 3+ and Li+ Co-doped ZnO photoluminescence by sol-gel process, Journal of Wuhan University of Technology-Mater. Sci. Ed. 23 (2008) 20-23.
[6] O. Lupan, T. Pauporté, B. Viana, P. Aschehoug, M. Ahmadi, B.R. Cuenya, Y. Rudzevich, Y. Lin, L.J.A.S.S. Chow, Eu-doped ZnO nanowire arrays grown by electrodeposition, Applied Surface Science 282 (2013) 782-788.
[7] H. Shahroosvand, M.J.J.o.L. Ghorbani-asl, Solution-based synthetic strategies for Eu doped ZnO nanoparticle with enhanced red photoluminescence, Journal of Luminescence 144 (2013) 223-229.
[8] E.I. Naik, H.B. Naik, R. Viswanath, I.S. Gowda, M.J.S.A.S. Prabhakara, Bright red luminescence emission of macroporous honeycomb-like Eu^{3+} ion-doped ZnO nanoparticles developed by gel-combustion technique, SN Applied Sciences 2 (2020) 863.
[9] A. Phuruangrat, O. Yayapao, T. Thongtem, S. Thongtem, Synthesis and characterization of europium-doped zinc oxide photocatalyst, Journal of Nanomaterials 2014 (2014).
[10] M.A. Malimabe, S.V. Motloung, T.E. Motaung, L.F. Koao, Effects of Eu^{3+} co-doping on the structural and optical properties of Ce^{3+} doped ZnO powder synthesized by chemical bath deposition method, Physica B: Condensed Matter, 579 (2020) 411890.
[11] U. Vinoditha, B. Sarojini, K. Sandeep, B. Narayana, S. Maidur, P. Patil, K.J.A.P.A. Balakrishna, Defects-induced nonlinear saturable absorption mechanism in europium-doped ZnO nanoparticles synthesized by facile hydrothermal method, Applied Physics A 125 (2019) 436.
[12] S. Yu, H. Zhang, C. Lin, M.J.C.A.P. Bian, The enhancement of humidity sensing performance based on Eu-doped ZnO, Current Applied Physics 19 (2019) 82-88.
[13] R.S. Oakes, A.A. Clifford, C.M. Rayner, The use of supercritical fluids in synthetic organic chemistry, Journal of the Chemical Society, Perkin Transactions 1, (2001) 917-941.
[14] C. Aymonier, A. Loppinet-Serani, H. Reverón, Y. Garrabos, F. Cansell, Review of supercritical fluids in inorganic materials science, The Journal of Supercritical Fluids, 38 (2006) 242-251.
[15] T. Adschiri, A. Yoko, Supercritical fluids for nanotechnology, The Journal of Supercritical Fluids, 134 (2018) 167-175.
[16] M. Meddouri, D. Djouadi, A. Chelouche, T. Touam, A. Chergui, Effect of co-solvent on structural and morphological properties of ZnO aerogel prepared by a modified sol-gel process, The European Physical Journal-Applied Physics, 66 (2014).
[17] O. Slimi, D. Djouadi, L. Hammiche, A. Chelouche, T. Touam, Structural and optical properties of Cu doped ZnO aerogels synthesized in supercritical ethanol, Journal of Porous Materials, 25 (2018) 595-601.
[18] F. Mouzaia, D. Djouadi, A. Chelouche, L. Hammiche, Al-Doping Effects on Structural and Morphological Properties of ZnO Aerogels Synthesized in Supercritical Ethanol, in: International Symposium on Materials and Sustainable Development, Springer, 2017, pp. 81-88.
[19] F. Mouzaia, D. Djouadi, A. Chelouche, L. Hammiche, T. Touam, Structural and optical investigations of pure and Al-doped ZnO nano-aerogels: effects of supercritical organic solvent, Applied Physics A, 125 (2019) 1-12.
[20] P. Mohanty, B. Kim, J.J.M.S. Park, E. B, Synthesis of single crystalline europium-doped ZnO nanowires, Materials Science and Engineering: B, 138 (2007) 224-227.

[21] A. Khataee, A. Karimi, M. Zarei, S.W.J.U.s. Joo, Eu-doped ZnO nanoparticles: sonochemical synthesis, characterization, and sonocatalytic application, Ultrasonics Sonochemistry, 67 (2020) 102822.
[22] A. Nouri, A. Beniaiche, B.M. Soucase, H. Guessas, A.J.O. Azizi, Photoluminescence study of Eu^{+3} doped ZnO nanocolumns prepared by electrodeposition method, Optik 139 (2017) 104-110.
[23] C.S. Barrett, T.B. Massalski, Structure of metals. Crystallographic methods, principles and data, (International Series on Materials Science and Technology), Pergamon (1980) 654 pp.
[24] F. Ren, R. Xin, X. Ge, Y.J.A.B. Leng, Characterization and structural analysis of zinc-substituted hydroxyapatites, Acta Biomaterialia 5 (2009) 3141-3149.
[25] B. Anandh, A.S. Ganesh, R. Thangarasu, R. Sakthivel, R. Kannusamy, K.J.O.J.o.C. Tamilselvan, Structural, morphological and optical properties of aluminium doped ZnO thin film by dip-coating method, Oriental Journal of Chemistry, 34 (2018) 1619-1624.
[26] C. Belkhaoui, N. Mzabi, H. Smaoui, P.J.R.i.P. Daniel, Enhancing the structural, optical and electrical properties of ZnO nanopowders through (Al+ Mn) doping, Results in Physics 12 (2019) 1686-1696.
[27] Y.-P. Du, Y.-W. Zhang, L.-D. Sun, C.-H.J.T.J.o.P.C.C. Yan, Efficient energy transfer in monodisperse Eu-doped ZnO nanocrystals synthesized from metal acetylacetonates in high-boiling solvents, J. Phys. Chem. C 112 (2008) 12234-12241.
[28] A. Sayari, L.J.K.P. El Mir, P. Journal, Structural and optical characterization of Ni and Al co-doped ZnO nanopowders synthesized via the sol-gel process, KONA Powder and Particle Journal (2015) 2015003.
[29] P. Li, H.-Y. Zhang, Z.-j. Li, J. Zhang, Effect of surfactants on morphology, structure and photoluminescence properties of Eu-doped ZnO microsphere, Optoelectronics letters, 16 (2020) 293-297.
[30] F. Li, H. Liu, L. Yu, Preparation, photoluminescence and photocatalytic properties of ZnO: Eu^{3+} nanocrystals, Journal of Nanoscience and Nanotechnology, 13 (2013) 5115-5118.
[31] M. Faraz, F.K. Naqvi, M. Shakir, N.J.N.J.o.C. Khare, Synthesis of samarium-doped zinc oxide nanoparticles with improved photocatalytic performance and recyclability under visible light irradiation, New Journal of Chemistry 42 (2018) 2295-2305.
[32] S. Zhao, L. Zhang, W. Li, L.J.P.j. Li, Preparation and fluorescent property of Eu (TTA) 3 phen incorporated in polycarbonate resin, Polymer Journal 38 (2006) 523-526.
[33] F. Berrekhis, Y. Roques, L. Aries, M. Hajjaji, Electrodeposition of casein coatings on zinc alloy, Progress in Organic Coatings 31 (1997) 341-345.
[34] P. Li, H.-y. Zhang, Z.-j. Li, J.J.O.L. Zhang, Effect of surfactants on morphology, structure and photoluminescence properties of Eu-doped ZnO microsphere, Optoelectronics Letters 16 (2020) 293-297.
[35] F. Mouzaia, D. Djouadi, A. Chelouche, L. Hammiche, T. Touam, Particularities of pure and Al-doped ZnO nanostructures aerogels elaborated in supercritical isopropanol, Arab J. Basic and Appl. Sci. 27 (2020) 423-430.
[36] Y. Zong, Z. Li, X. Wang, J. Ma, Y.J.C.I. Men, Synthesis and high photocatalytic activity of Eu-doped ZnO nanoparticles, Ceramics International 40 (2014) 10375-10382.
[37] J. Iqbal, X. Liu, H. Zhu, Z. Wu, Y. Zhang, D. Yu, R.J.A.m. Yu, Raman and highly ultraviolet red-shifted near band-edge properties of LaCe-co-doped ZnO nanoparticles, Acta Materialia 57 (2009) 4790-4796.
[38] M. Khatamian, A. Khandar, B. Divband, M. Haghighi, S. Ebrahimiasl, Heterogeneous photocatalytic degradation of 4-nitrophenol in aqueous suspension by Ln (La^{3+}, Nd^{3+} or

Sm^{3+}) doped ZnO nanoparticles, Journal of Molecular Catalysis A: Chemical 365 (2012) 120-127.
[39] A. Layek, S. Banerjee, B. Manna, A. Chowdhury, Synthesis of rare-earth doped ZnO nanorods and their defect–dopant correlated enhanced visible-orange luminescence, RSC Advances, 6 (2016) 35892-35900.
[40] Y.-P. Du, Y.-W. Zhang, L.-D. Sun, C.-H. Yan, Efficient energy transfer in monodisperse Eu-doped ZnO nanocrystals synthesized from metal acetylacetonates in high-boiling solvents, The Journal of Physical Chemistry C, 112 (2008) 12234-12241.
[41] P. Aneesh, M. Jayaraj, Red luminescence from hydrothermally synthesized Eu-doped ZnO nanoparticles under visible excitation, Bulletin of Materials Science, 33 (2010) 227-231.
[42] S. Gao, H. Zhang, R. Deng, X. Wang, D. Sun, G. Zheng, Engineering white light-emitting Eu-doped ZnO urchins by biopolymer-assisted hydrothermal method, Applied physics letters, 89 (2006) 123125.
[43] O. Lupan, T. Pauporté, B. Viana, P. Aschehoug, M. Ahmadi, B.R. Cuenya, Y. Rudzevich, Y. Lin, L. Chow, Eu-doped ZnO nanowire arrays grown by electrodeposition, Applied Surface Science, 282 (2013) 782-788.
[44] D. Wang, G. Xing, M. Gao, L. Yang, J. Yang, T. Wu, Defects-mediated energy transfer in red-light-emitting Eu-doped ZnO nanowire arrays, The Journal of Physical Chemistry C, 115 (2011) 22729-22735.
[45] M. Wang, C. Huang, Z. Huang, W. Guo, J. Huang, H. He, H. Wang, Y. Cao, Q. Liu, J. Liang, Synthesis and photoluminescence of Eu-doped ZnO microrods prepared by hydrothermal method, Optical Materials, 31 (2009) 1502-1505.
[46] J. Yang, X. Li, J. Lang, L. Yang, M. Wei, M. Gao, X. Liu, H. Zhai, R. Wang, Y. Liu, Synthesis and optical properties of Eu-doped ZnO nanosheets by hydrothermal method, Materials Science in Semiconductor Processing, 14 (2011) 247-252.
[47] A.B. Djurišić, Y.H. Leung, Optical properties of ZnO nanostructures, Small, 2 (2006) 944-961.
[48] A. Djurišić, A.M.C. Ng, X. Chen, ZnO nanostructures for optoelectronics: Material properties and device applications, Progress in quantum electronics, 34 (2010) 191-259

A 42-kHz ULTRASONIC TRANSMITTER BASED ON A TMS320C6713B PROCESSOR

Victor Cojocaru

Ghitu Institute of Electronic Engineering and Nanotechnologies, Technical University of Moldova, Academiei 3/3 str., Chisinau, MD-2028 Republic of Moldova
E-mail: vikcojocaru@gmail.com

(Received, 20 April, 2023)

https://doi.org/10.53081/mjps.2023.22-1.07

Abstract

The paper describes a software design for a 42-kHz ultrasonic transmitter based on the 32-bit timer of a TMS320C6713B processor.

Keywords: ultrasound, 32-bit timer, pulse trains.

Rezumat

În lucrarea dată este descris designul soft al unui transmițător cu ultrasunete în baza timer-ului de 32 de biți al unui procesor TMS320C6713B.

Cuvinte cheie: ultrasunet, timer de 32 de biți, tren de impulsuri.

1. Introduction

Ultrasounds are acoustic waves with frequencies higher than 20 kHz. They are used, particularly, in medicine and technology. One of these technical fields is robotics, where ultrasound is understood as echolocation. Short pulses modulated with a sinusoidal, chirp, or chaotic signal are used for echolocation. The aim of this study is to develop a software for a 42-kHz ultrasound transmitter consisting of pulse trains with a required length.

2. Pulse train implementation methods

To obtain a required length of pulse trains, it is necessary to calculate the pulse duration τ_1 and pause duration τ_2, with the minimum and maximum detection distances D_{min} and D_{max} value, respectively, of a MuRata MA40B8R ultrasound receiver [1, 2], as shown in Figure 1.
With

$$D_{min} = 0.2m \quad (1)$$

and

$$D_{max} = 6m \quad (2)$$

the values of

$$\tau 1 = \frac{2D_{\min}}{V} = \frac{0.4}{350} = 0.001s \quad (3)$$

and

$$\tau 2 = \frac{2D_{\max}}{V} = \frac{12}{350} = 0.034s \quad (4)$$

are obtained.

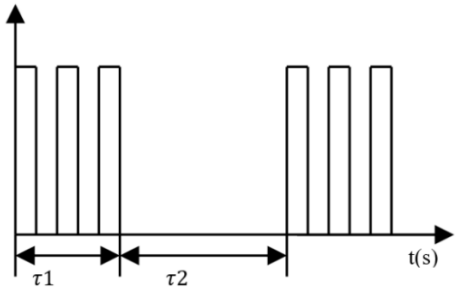

Fig. 1. Examples of pulse trains.

3. Architecture of the 32-bit timer of the TMS320C6713B processor

To obtain pulse trains with a required frequency, it is necessary to use interrupts generated by a 32-bit Timer [4]. The timer operates on the incremental principle in the TMS32C6000 processors. A 32-bit timer can be used for the following issues:

- Counters
- Pulse generation
- CPU interrupts.

The timer has two synchronization modes: from the external clock through a TINT pin and from the internal clock. Through a TOUT pin, it can be used as a clock source, for example, for A/D to start the conversion process. Similarly, signals from a pulse generator are obtained through a TOUT pin. In addition, TINT and TOUT pins can be used as general purposes pins in cases where synchronization or external generation is not required. The timer of a TMS320C6713B processor has three registers [3,4], as shown in Figure 2.

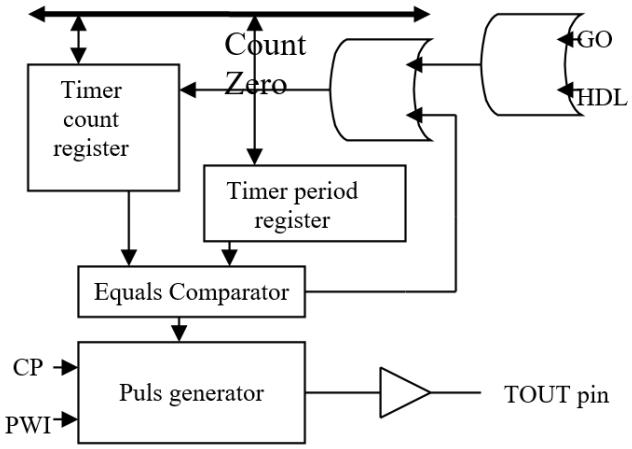

Fig. 2. Structure of a 32-bit timer.

CTL initiates the operating mode of the timer and governs the TOUT pin. BRD contains the number of clock cycles at the input or determines the TOUT signal period. CNT is a 32-bit register that stores the current counter value, while incrementing the values from 0 to *N*. The timer has two operating modes: a pulse mode and a pulse oscillator mode. The second mode should be used to form pulse trains. The initial setting of a timer requires four basic steps, as shown in Figure 3.

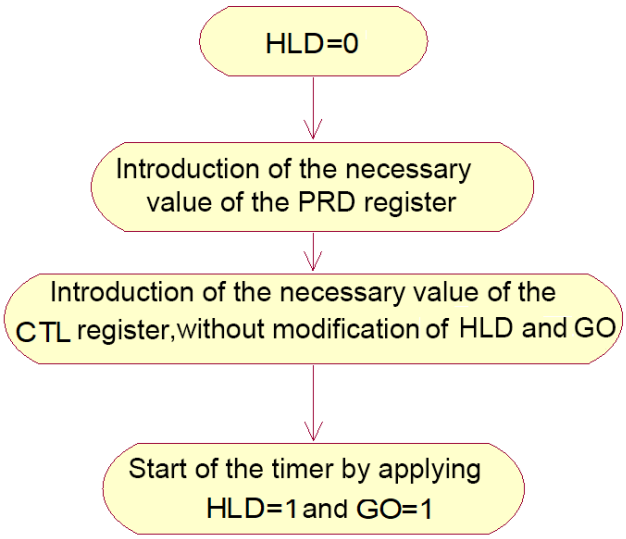

Fig. 3. Initial setting.

4. Structure and organization of the program

To provide the formation of pulse trains, it is primarily necessary to perform required calculations for values of the timer registers, as shown in Fig. 4.

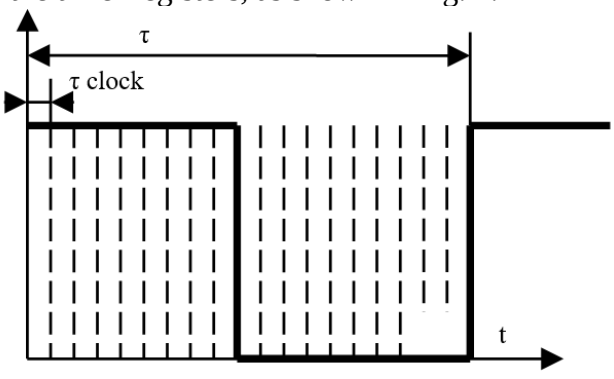

Fig. 4. Formation of pulse trains.

The clock frequency of a TMS320C6713 processor is 225 MHz, while the clock frequency of the timer is 56.25 MHz [3]. The clock pulse duration is calculated using expression (5):

$$\tau_{clock} = \frac{1}{56.25MHz} = 1.8 \times 10^{-8} s\,. \qquad (5)$$

The duration of a 42-kHz clock pulse is calculated using formula (6):

$$\tau = \frac{1}{42kHz} = 2.38 \times 10^{-5} s \quad (6)$$

The calculations for the required value of *N* of the BRD register are performed using formulas (7) and (8):

$$\tau = \tau_{clock} \times N \quad (7)$$

$$N = \frac{\tau}{\tau_{clock}} = 1339 \quad (8)$$

After calculations for the formation of a 42-kHz meander, it is necessary to calculate the number of pulses $N_{imp42kHz}$ required for emission (E) and reception (R), according to formulas (9) and (10), making use of the values of τ_1 and τ_2 calculated according to formulas (3) and (4), respectively:

$$N_{imp\,42\,KHz} E = \frac{\tau_1}{\tau} = 42 \quad (9)$$

$$N_{imp\,42\,KHz} R = \frac{\tau_1}{\tau} = 14279 \quad (10)$$

To obtain pulses at the transmitter, it is necessary to use the ability of the TOUT pin to be used as a general-purpose pin, or a timer pin, depending on the bit value of FUNC and DATOUT of the CTL register (see Table 1).

Table 1. Structure of the CTL register

Number	Name	Value	Value used
31-12	Reserved	0	0
11	TSTAT	0/1	0
10	INVNP	0/1	0
9	CLKSRC	0/1	1
8	CP	0/1	1
7	HDL	0/1	1
6	GO	0/1	1
5	Reserved	0	0
4	PWID	0/1	0
3	DATIN	0/1	0
2	DATOUT	0/1	1 on emission 0 on reception
1	INVOUT	0/1	0
0	FUNC	0/1	1 on emission 0 on reception

In the PRD register, enter the required value for a frequency of 42 kHz.
T_EMISSION=42 is the number of 42-kHz pulses required for emission.
T_TOTAL=14279 is the number of 42-kHz pulses required for emission.

The program code was described in the Code Composer Studio™ development environment. It includes several facilities to facilitate the use of the peripheral. Figure 5 shows the organizational chart of the program, while in Figure 6 the algorithm of the pulse train formation program is presented.

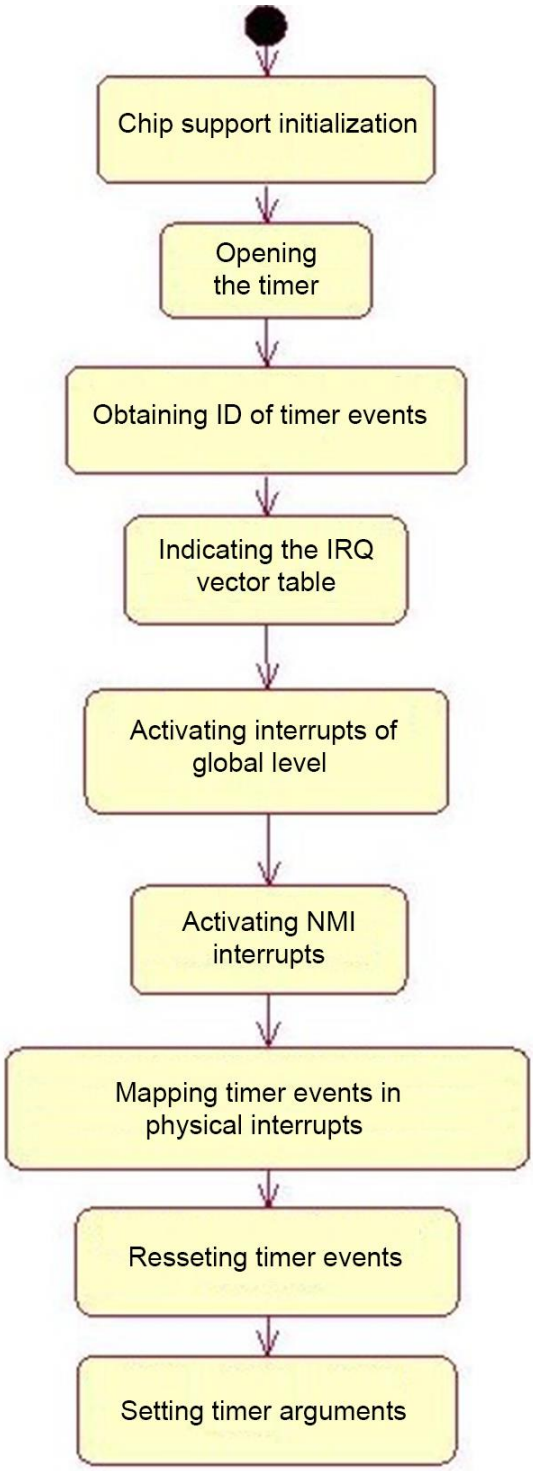

Fig. 5. Organizational chart of functioning of the program.

The Chip Support Library (CSL) provides a C-+ interface for setting and controlling chip-peripherals. It is composed of discrete modules, which are constructed and archived in a library of files. Each module is referred to only one peripheral module. In our case, it is the timer. The timer support is in the csl_timer.h file.

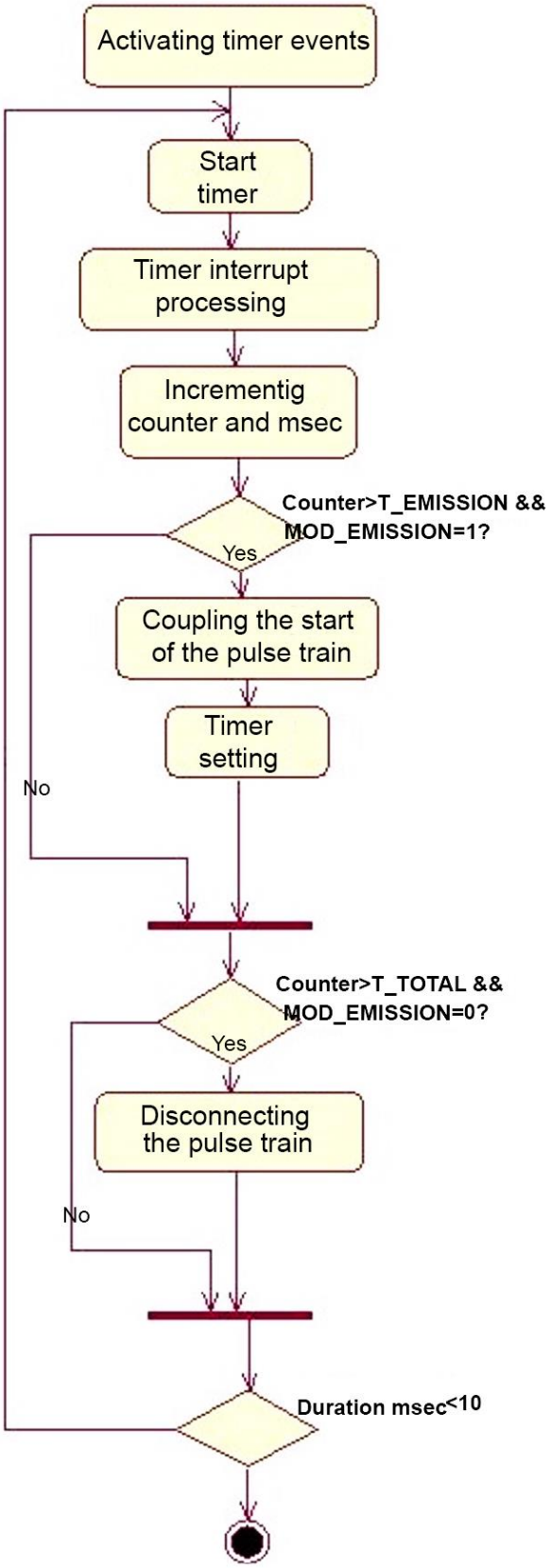

Fig. 5. Algorithm of the pulse train formation program.

5. Conclusions

The use of a TMS320C6713B processor at a clock frequency of 225 MHz makes it possible to design transmitters operating at frequencies higher than 42 kHz. The use of the timer simplifies the description of the code, because the frequency can be changed simply by changing the value of the registers.

References

[1] H.N. Teodorescu Notă de curs "Electronică şi informatică medicala" 2009
[2] http://www.murata.com/products/catalog/pdf/p19e.pdf
[3] http://compel.ru/catalog/dsp/dsp_tms320/tms320c67x/tms320c6713b
[4] http://focus.ti.com/lit/ug/spru582b/spru582b.pdf
[5] http://focus.ti.com/lit/ds/symlink/tms320c6713b.pdf

GENDER DIMENSION IN STEM EDUCATION IN THE REPUBLIC OF MOLDOVA: EFFORTS AND TRENDS

Victoria Lisnic

Legal Political and Sociological Research Institute, Republic of Moldova
E-mail: victorialisnic08@yahoo.com

(Received, 20 March, 2023)

https://doi.org/10.53081/mjps.2023.22-1.08

Abstract

By encouraging girls and women to develop and maintain an interest in STEM subjects, we are preparing the next generation of researchers, engineers, scientists and programmers to meet the growing demand for skilled STEM professionals. Current and future jobs and societal challenges require and will increasingly require a wide range of skills such as teamwork, intercultural competence, empathy, creativity, problem solving and independent non-linear thinking. Accordingly, we must ensure that women and girls are widely represented at all levels as we move forward. It is more important than ever that we eliminate stereotypes and biases and promote women and girls who want to pursue STEM careers.

Keywords: STEM, education, gender, segregation, stereotypes.

Rezumat

Încurajând fetele și femeile să dezvolte și să mențină interesul pentru subiectele STEM, pregătim următoarea generație de cercetători, ingineri, oameni de știință și programatori pentru a răspunde cererii tot mai mari de profesioniști calificați în STEM. Locurile de muncă actuale și viitoare și provocările societale necesită și vor necesita din ce în ce mai mult o gamă largă de abilități, cum ar fi munca în echipă, competența interculturală, empatia, creativitatea, rezolvarea problemelor și gândirea independentă neliniară. În consecință, trebuie să ne asigurăm că femeile și fetele sunt reprezentate pe scară largă la toate nivelurile pe măsură ce avansăm. Este mai important ca oricând să eliminăm stereotipurile și părtinirile și să promovăm femeile și fetele care doresc să urmeze cariere STEM.

Cuvinte cheie: STEM, educație, gen, segregare, stereotipuri.

1. Introduction

The current global trends of the transition from the industrial society to the information society and Industry 4.0 constitute a revolutionary global change comparable to the emergence of the steam engine in the 19th century, electricity in the first half of the 20th century and the Internet in the late 20th century. Global societies are becoming more advanced and technology is more integrated into a daily life than ever before. World moves to an increasingly digital

economy and closing the global gender gap in science, technology, engineering and mathematics (STEM) education is critical to empowering women economically and addressing the shortage of skilled people needed to meet the growing demand for technology jobs. Recent studies show that closing the gender gap in STEM education fields could help reduce labor market bottlenecks, increase women's employment and productivity, and reduce occupational segregation. Ultimately, this would stimulate economic growth both by increasing productivity and increasing labor market activity.

2. STEM Disciplines

The acronym STEM refers to a number of academic disciplines such as science, technology, engineering and mathematics, intended to make a beneficial and significant contribution to the training provided by the education system in these fields. They ensure workforce development by shaping the vision of students according to market demands. STEM education changes society by giving learners a new mindset and skills valued in any profession. They allow learners to be flexible, look for patterns, find connections and evaluate information. STEM education develops critical thinking, increases scientific literacy and empowers the next generation of innovators. It should be noted that there is also the STEAM initiative, proposed by Georgette Yakman, which introduced art among these subjects, considering that there is a link between them that corresponds to the global socioeconomic system [1].

3. STEM Learning

STEM education gives people skills that make them more employable and ready to meet the current labor demand. However, despite good employment opportunities and highly productive jobs in this area, there is currently a low proportion of women studying and graduating in STEM subjects. Although education is one of the most critical areas of women's empowerment, socio-economic barriers and negative stereotypes are still prevalent when it comes to STEM. This gender disparity is alarming, especially as STEM careers are often referred to as the jobs of the future, driving innovation, social wellbeing, inclusive growth and sustainable development. Although girls generally perform better than boys in the Programme for International Student Assessment (PISA) and International Computer and Information Literacy Study (ICILS) international skills tests, they veer away from STEM subjects with age. Actions to promote high quality and inclusive computing education can impact positively on the number of girls pursuing IT-related studies in higher education and, further on, working in the digital sector or digital jobs in other economic sectors. Efforts to address gender stereotypes and gender bias in the digital sector are crucial to improving gender balance in the sector.

4. EU STEM approaches

At the European Union level according to the She Figures 2021, women are still underrepresented as doctoral graduates in STEM fields, including physical sciences (38%), ICT (20.8%), engineering (27%), and mathematics (32.5%) [2]. In order to fix the situation one of the six priorities of the European Commission envisages the digital transformation of Europe by 2030. The Strategy “A Europe fit for digital age” evolves around four cardinal points: Basic digital skills for min 80% of population; Digital transformation of businesses; Digital infrastructures**;** Digitalization of public services (key public services - 100% online).

„Digitization is massively increasing the demand for ICT specialists in the labor market. But that alone is not enough: we will also need to boost basic skills amongst the work force and population at large. Digital literacy has to be a foundation for everyone" [3]. One of the 14 actions of the Digital Education Action Plan 2021-2027, Resetting education and training for the digital age, provides "Encourage women's participation in STEM, in cooperation with the European Institute of Innovation and Technology (EIT); support the EU STEM Coalition to develop new higher education curricula for engineering and information and communications technology based on the STEAM approach to be more attractive for women and increase their participation and career development in STEM subjects and IT" [4]. Another instrument of the European Commission to improve the situation in the field of STEM is the Program dedicated to research and innovation - Horizon Europe. Projects are expected to contribute to increasing cooperation between relevant research and innovation actors from academia, the private sector and national administrations to encourage the participation of women and girls in STEM studies and careers through a STEAM approach. The most recent calls, launched on December 6, 2022, for approaches to gender-responsive STEAM education are: Support to the implementation of an EU Manifesto for STE(A)M education and research and innovation career paths to tackle gender inequalities in ERA; Cultural and creative approaches for gender-responsive STEAM education; Organization of the Women TechEU Scheme [5].

5. STEM education in Moldova

In the case of the Republic of Moldova, the problem of integrating women and girls in STEM sciences is even more accentuated. Although according to National Bureau of Statistic data almost 60% of higher education graduates are women, only 20.5% of them are employed in the STEM field [6]. The perception that the so-called core technological careers are more demanding in terms of availability due to high responsibilities prevails. As long as decision-makers are predominantly male, it will be difficult for women to find a role model in the STEM world. According to the Global data on National Parliaments on January 1, 2023 Moldova is situated on 27th place out of 190 countries with 41 seats occupied by women out of 101 seats in parliament [7]. The participation of women in decision-making in the Parliament reveals a representation of women in a proportion of 38.6% compared to 31.0% at the European level and 26.5% at the global level. However, despite the fact that at the European and Global level the situation from the perspective of the gender dimension in Moldova is quite good, stakeholders in collaboration with policymakers can and must continuously contribute to improving data collection, monitoring, and evaluation of policies aimed at tackling inequalities in STEM fields to better understand which programs are most effective and efficient. The issue of gender disparities in STEM is a complex one and should be addressed accordingly. Considering the underlying causes of gender disparities in the sector and integrating them into policies is vital, as treating the symptoms without addressing the causes would lead to superficial and ineffective measures. To promote and encourage the emancipation of women, the government must be well informed about how the research system of the Republic of Moldova works in practice, the barriers to access and how the challenges can be overcome. One of the major problems in attracting women to STEM is the unattractiveness of the research system of the Republic of Moldova. According to the Eurostat data base "European Neighborhood Policy ranking", the Republic of Moldova records the lowest results regarding the attractiveness of the research system with the lowest level of funding (0.2% GDP) and the lowest number of researchers per capita, - 4 times less researchers than the European average [8].

Table 1. Cross domestic expenditure on research and development for the years 2010 and 2020

	Cross expenditure on R&D (€ million)		R&D expenditure (€ per inhabitant)		R&D intensity (% of GDP)	
	2010	2020	2010	2020	2010	2020
EU	216261.1	310711.1	490.8	694.6	2.0	2.3
Armenia	16.8	*	5.2	*	0.2	*
Azerbaijan	87.3	82.7	9.7	8.2	0.2	0.2
Belarus	288.8	290.7	30.5	30.9	0.7	0.5
Georgia	25.4	*	5.7	*	0.3	*
Moldova	19.3	23.8	5.4	6.7	0.4	0.2
Ukraine	854.1	552.9	18.7	13.2	0.8	0.4

* Lack of data on the Eurostat portal

However, it should to be mentioned that, starting from the increasingly pronounced role of STEM in the national economy and the importance of ensuring equal opportunities and empowering women and girls in this sector, and in order to ensure a social and economic balance in Moldavian society, some measures were taken. An eloquent example of success is the creation in 2017 of the Center of Excellence - Tekwill. Tekwill has been designed as a national public private partnership between the Government of Moldova, USAID, Microsoft, and IBM to answer the needs of the ICT industry to close the gap of the human capital shortage, as well as support the development of the entrepreneurship ecosystem. In a very short time Tekwill has become the home of innovation, where people are connected with ideas, resources, science and industry to enhance IT excellence. Being considered as one of the biggest public private partnerships, the key success of the project is to ensure the proper involvement of all stakeholders into the process. Since its establishment more than 718,232 people have participated in Tekwill activities, of which 44.48% are women. More than 1,597 teams and products were developed through projects [10]. Among the priorities of the Tekwill project is to introduce more women into the workforce in the ICT sector, as well as to reduce income and occupational imbalances. Thus, three years ago, the Tech Women empowerment initiative was born. Tech Women hub brings together a multitude of events for experience exchange, knowledge transfer, mentoring programs, motivational conferences, educational actions and to facilitate access to career opportunities, growth and professional affirmation in the field of technologies. It provides guidance and links to information and resources that can be used to spark girls' interest in STEM and raise awareness of the importance of girls' engagement in these fields of today and tomorrow. Due to a prodigious collaboration between Tekwill, the UN Women over 1000 girls and women have been trained in the IT field. This is one of the successful examples denoting a positive evolution in creating good premises and conditions for improving the situation of attracting women in STEM education. At the same time, it is worth noting the importance of other organizations that promote STEM fields among girls in the Republic of Moldova, such as: Girls Go IT, Tech Ambassadors, Rails Girls, ICT Career Orientation and ATIC.

5. Conclusions

In conclusion, it can be said that in the present, social, cultural, economic, educational and institutional factors sustain the persisting gender segregation across study fields. Stereotyping in education, gender differences in educational and training choices and a lack of female role models are major problems contributing to the low percentage of women graduating in STEM subjects. The growing demand for professionals with skills in science, technology, engineering and mathematics (STEM) and the so-called fourth industrial revolution is expected to create a wide range of new jobs in these fields. However, unless efforts are made to address the mismatch between current skills and what will be needed for the future, this revolution will leave behind a large proportion of girls and women who are underrepresented in these fields.

However, there are solutions that can turn things around. A basic recommendation is to combat stereotypes by simply convincing individuals that they exist and should be avoided. Also, promoting successful models is a good method of encouragement. The power of example boosts motivation, causing women to believe in their capabilities and that they can achieve success that others have found impossible to achieve. Facilitating access to mentors is also essential, ensuring young women's interest in a STEM career is maintained.

References

[1] Yakman, G., STEAM education: An overview of creating a model of integrative education, 2008.
[2] European Commission, Directorate-General for Research and Innovation, *She figures handbook 2021*, Publications Office, 2021, https://data.europa.eu/doi/10.2777/003736
[3] Answers to the European parliament questionnaire to the commissioner-designate, Margrete Vestager, Executive Vice-President-designate for a Europe fit for the Digital Age https://ec.europa.eu/commission/commissioners/sites/default/files/commissioner_ep_hearings/answers-ep-questionnaire-vestager.pdf
[4] Digital Education Action Plan 2021-2027, Resetting education and training for the digital age. https://eur-lex.europa.eu/legal-content/EN/TXT/?uri=CELEX%3A52020DC0624
[5] Funding & tender opportunities**,** Single Electronic Data Interchange Area (SEDIA) https://ec.europa.eu/info/funding-tenders/opportunities/portal/screen/home
[6] Biroul National de Statistica https://statistica.gov.md/ro
[7] Global data on National Parliaments https://data.ipu.org/women-ranking?month=12&year=2022
[8] Portretul statistic al femeilor și bărbaților în Republica Moldova https://statistica.gov.md/ro/portretul-statistic-al-femeilor-si-barbatilor-in-republica-moldova-9617_60333.html
[9] European Neighborhood Policy - East - statistics on science, technology and digital society https://ec.europa.eu/eurostat
[10] Tekwill - Center of Excellence https://tekwill.md/